



UPPSALA
UNIVERSITET

*Digital Comprehensive Summaries of Uppsala Dissertations
from the Faculty of Science and Technology 2010*

Engineering Surfaces of Solid-State Nanopores for Biomolecule Sensing

SHIYU LI



ACTA
UNIVERSITATIS
UPSALIENSIS
UPPSALA
2021

ISSN 1651-6214
ISBN 978-91-513-1129-6
urn:nbn:se:uu:diva-433812

Dissertation presented at Uppsala University to be publicly examined in Siegbahnsalen, Ångströmlaboratoriet, Lägerhyddsvägen 1, Uppsala, Friday, 26 March 2021 at 09:15 for the degree of Doctor of Philosophy. The examination will be conducted in English. Faculty examiner: Professor Michael Mayer (Adolphe Merkle Institute, University of Fribourg).

Abstract

Li, S. 2021. Engineering Surfaces of Solid-State Nanopores for Biomolecule Sensing. *Digital Comprehensive Summaries of Uppsala Dissertations from the Faculty of Science and Technology* 2010. 91 pp. Uppsala: Acta Universitatis Upsaliensis. ISBN 978-91-513-1129-6.

Nanopores have emerged as a special class of single-molecule analytical tool that offers immense potential for sensing and characterizing biomolecules such as nucleic acids and proteins. As an alternative to biological nanopores, solid-state nanopores present remarkable versatility due to their wide-range tunability in pore geometry and dimension as well as their excellent mechanical robustness and stability. However, being intrinsically incompatible with biomolecules, surfaces of inorganic solids need be modified to provide desired functionalities for real-life sensing purposes. In this thesis, we presented an exploration of various surface engineering strategies and an examination of several surface associated phenomena pertaining specifically to solid-state nanopores. Based on the parallel sensing concept using arrayed pores, optical readout is mainly employed throughout the whole study.

For the surface engineering aspect, a list of approaches was explored. A versatile surface patterning strategy for immobilization of biomolecules was developed based on selective poly(vinylphosphonic acid) passivation and electron beam induced deposition technique. This scheme was then implemented on nanopore arrays for nanoparticle localization. In addition, vesicle rupture-based lipid bilayer coating was adapted to truncated-pyramidal nanopores, which was shown to be effective for the minimizing DNA-pore interaction. Further, HfO_2 coating by means of atomic layer deposition was employed to prevent the erosion of Si-based pores and to shrink the pore diameter, which enabled reliable investigations of DNA clogging and DNA polymerase docking.

For the surface associated phenomena, several findings were made. The lipid bilayer formation on truncated pyramidal nanopores via instantaneous rupture of individual vesicles was quantified based on combined ionic current monitoring and optical observation. The probability of pore clogging appeared to linearly increase with the length of DNA strands and applied bias voltage, which could be attributed a higher probability of knotting and/or folding of longer DNA strands and more frequent translocation events at higher voltage. A free-energy based analytical model was proposed to evaluate the DNA-pore interaction and to interpret observed clogging behavior. Finally, docking of DNA polymerase on nanopore arrays was demonstrated using label-free optical method based on Ca^{2+} indicator dyes, which may open the avenue to sequencing-by-synthesis enabled by the docked polymerase.

Keywords: solid-state nanopores, surface engineering, DNA sensing, DNA polymerase, optical detection, lipid bilayer, hafnium oxide, electron beam induced deposition

Shiyu Li, Department of Electrical Engineering, Solid-State Electronics, Box 534, Uppsala University, SE-751 21 Uppsala, Sweden.

© Shiyu Li 2021

ISSN 1651-6214

ISBN 978-91-513-1129-6

urn:nbn:se:uu:diva-433812 (<http://urn.kb.se/resolve?urn=urn:nbn:se:uu:diva-433812>)

“工欲善其事，必先利其器”

— 孔子, 《论语·卫灵公》

“The craftsman who wishes to do his work well
must first sharpen his tools.”

— Confucius, The Analects

List of papers

This thesis is based on the following papers, which are referred to in the text by their Roman numerals.

- I **Li, S.;** Zeng, S.; Chen, L.; Zhang, Z.; Hjort, K.; Zhang, S.-L. (2018) Nanoarrays on Passivated Aluminum Surface for Site-Specific Immobilization of Biomolecules. *ACS Applied Bio Materials*, 1 (1), 125-135.
- II **Li, S.;** Zeng, S.; Zhang, Z.; Hjort, K.; Zhang, S.-L. (2019) Nanoparticle Localization on Solid-State Nanopores via Electrophoretic Force”, *TRANSDUCERS & EUROSENSORS XXXIII*, 2372-2375.
- III **Zeng, S.*; Li, S.*;** Utterström, J.; Wen, C.; Selegård, R.; Zhang, S.-L.; Aili, D.; Zhang, Z. (2020) Mechanism and Kinetics of Lipid Bilayer Formation in Solid-State Nanopores. *Langmuir*, 36, 1446-1453.
- IV **Li, S.;** Zeng, S.; Zhang, Z.; Hjort, K.; Zhang, S.-L. (2020) Visualization of DNA Translocation and Clogging using Photoluminescent-Free Silicon Nanopore Arrays. *IEEE-NANO 2020*, 193-197.
- V **Li, S.;** Zeng, S.; Wen, C.; Barbe, L.; Tenje, M.; Zhang, Z.; Hjort, K.; Zhang, S. -L. (2020) “Dynamics of DNA Clogging in Hafnium Oxide Nanopores”, *The Journal of Physical Chemistry B*, 124(51), 11573-11583.
- VI **Li, S.;** Zeng, S.; Wen, C.; Zhang, Z.; Hjort, K.; Zhang, S. -L. “Label-Free Optical Detection of DNA Polymerase Docking on Solid-State Nanopore Arrays”, *Manuscript*.

*The authors contributed equally to the work.

Reprints were made with permission from the respective publishers.

Author's contributions

- I Planned and performed all the experimental work, took part in discussion and wrote the manuscript including revising the manuscript in accordance to referee comments.
- II Planned and performed most of the experimental work apart from the nanopore device fabrication, took part in discussion and wrote the manuscript.
- III Performed fluorescence microscopy observation of lipid bilayer formation and the fluorescence recovery after photobleaching experiments, took part in discussion and wrote part of the manuscript.
- IV Planned and performed most of the experimental work apart from the nanopore device fabrication and preparation of vesicles, took part in discussion and wrote the manuscript.
- V Planned and performed most of the experimental work, took part in analytical modelling and discussion, and wrote the manuscript in accordance to referee comments.
- VI Planned and performed most of the experimental work apart from the nanopore device fabrication, took part in discussion and wrote the manuscript.

Publications not included in this thesis

- I Wen, C.; **Li, S.**; Zeng, S.; Zhang, Z.; Zhang, S.-L. (2019) Auto-genic Analyte Translocation in Nanopores. *Nano Energy*, 60, 503-509.
- II Zeng, S.; Wen, C.; **Li, S.**; Chen, X.; Chen, S.; Zhang, S.-L.; Zhang, Z.; (2019) “Controlled Size Reduction to Form Solid-State Nanopores via Electron Beam Induced Carbon Deposition. *Nanotechnology*, 30, 455303.
- III Wen, C.; Zeng, S.; **Li, S.**; Zhang, Z.; Zhang, S.-L. (2019) On Rectification of Ionic Current in Nanopores. *Analytical Chemistry*, 91 (22), 14597-14604.
- IV Xu, X.; Makaraviciute, A.; Abdurakhmanov, E.; Wermeling, F.; **Li, S.**; Danielson, U. H.; Nyholm, L.; Zhang, Z. (2020) Estimating Detection Limits of Potentiometric DNA sensors Using Surface Plasmon Resonance Analyses. *ACS Sensors*, 5(1), 217-224.

Contents

1. Introduction: The hole story.....	15
1.1 Emergence of nanopore sensors.....	15
1.2 Biological vs. Solid-state nanopores.....	17
1.3 Surface tailoring for solid-state pores.....	20
1.4 Electrical vs. Optical nanopore sensing.....	23
1.5 Scope of the thesis.....	25
2. Theoretical background: Interface matters.....	27
2.1 Surface charge & Electrical double layer.....	27
2.2 Pore conductance: Bulk & Surface.....	29
2.3 Electrophoresis & Electroosmosis.....	31
2.4 Erosion of SiN _x /Si/SiO ₂ surface.....	33
2.5 Surface-biomolecule interactions.....	34
3. Surface patterning on solid-state nanopore arrays.....	37
3.1 Surface patterning of carbon nanoarrays.....	38
3.1.1 Selective PVPA passivation against nonspecific adsorption.....	38
3.1.2 Preparation and characterization of nanopatterns by EBID.....	39
3.2 Site-specific immobilization of various analytes.....	40
3.2.1 Streptavidin and oligonucleotides.....	41
3.2.2 Biotinylated nanoparticles.....	41
3.2.3 DNA polymerase.....	43
3.3 Deposition of carbon nanoarray on nanopore array.....	44
3.3.1 Fabrication of SiN _x nanopore arrays.....	45
3.3.2 Deposition of carbon domain in the vicinity of nanopore.....	46
3.4 Localization of nanoparticles on nanopore array.....	47
3.4.1 Diffusion-based approach.....	47
3.4.2 Electrophoresis-based approach.....	48
4. Lipid bilayer coated on truncated-pyramidal Si nanopore arrays.....	49
4.1 Fabrication of truncated-pyramidal nanopore arrays.....	49
4.2 Formation of lipid bilayer on TPP arrays.....	50
4.2.1 Electrical monitoring of lipid bilayer formation.....	51
4.2.2 Optical observation of lipid bilayer formation.....	53
4.2.3 Fluorescence recovery after photobleaching.....	54

4.3 Optical detection of DNA translocation on TPPs.....	55
4.3.1 Photoluminescence of SiN _x	55
4.3.2 Fluidic cell and optical setup	56
4.3.3 Optical observation of DNA translocation	57
5. DNA clogging on HfO ₂ nanopore arrays	59
5.1 Coating HfO ₂ on Si nanopore arrays	60
5.2 DNA clogging behavior in nanopore arrays.....	61
5.2.1 Effects of DNA lengths and applied voltages.....	61
5.2.2 Temporary clogging behavior.....	63
5.2.3 Effects of solution pH values.....	65
5.3 Analytical model for accounting clogging behavior	65
5.3.1 Model building.....	66
5.3.2 Model results	67
6. Docking of DNA polymerase on nanopores	69
6.1 Device and detection system	70
6.1.1 Shrinkage of pore diameter by means of ALD	70
6.1.2 Characterization of optical label-free detection method.....	71
6.2 Docking of DNA polymerase.....	72
6.2.1 Electrical detection on single pore.....	72
6.2.2 Optical detection on pore arrays	74
7. Summary and outlook	75
Sammanfattning på Svenska	79
Acknowledgement	81
References.....	83

Abbreviations and Symbols

2D	Two-dimensional
3D	Three-dimensional
ALD	Atomic layer deposition
Al ₂ O ₃	Aluminum oxide
B.C.	Before Chirst
BOX	Buried oxide
BHF	Buffered hydrofluoric acid
CDB	Controlled dielectric breakdown
DNA	Deoxyribonucleic acid
DNAP	DNA polymerase
DRIE	Deep reactive ion etching
dsDNA	Double-stranded deoxyribonucleic acid
EBID	Electron beam induced deposition
EBL	Electron beam lithography
EDL	Electric double layer
EDX	Energy dispersive X-ray spectroscopy
EOF	Electroosmosis flow
FET	Field effect transistor
H ₂ O ₂	Hydroperoxide
H ₂ SO ₄	Sulfuric acid
HfO ₂	Hafnium oxide
KCl	Potassium chloride
KOH	Potassium hydroxide
LPCVD	Low pressure vapor deposition
MspA	<i>Mycobacterium smegmatis</i> porin A
MoS ₂	Molybdenum disulfide
MXene	2D transition metal carbide
ONT	Oxford Nanopore Technologies
PBS	Phosphate buffered saline
PDMS	Polydimethylsiloxane
PEEK	Polyether ether ketone
PEG	Poly(ethylene glycol)
pI	Isoelectric point
PL	Photoluminescence
POPC	1-palmitoyl-2-oleoyl-glycero-3-phosphocholine
PVPA	Poly(vinylphosphonic acid)

PZC	Point of zero charge
RCA	Rolling circle amplification
RIE	Reactive ion etching
SAM	Self-assembled monolayer
SNR	Signal to noise ratio
SEM	Scanning electron microscopy
SMRT	Single-molecule real-time
Si	Silicon
SiN _x	Silicon nitride
SiO ₂	Silicon dioxide
SOI	Silicon on insulator
ssDNA	Single-stranded deoxyribonucleic acid
STM	Scanning tunneling microscopy
TiO ₂	Titanium oxide
TEM	Transmission electron microscopy
TPP	Truncated pyramidal shape
XPS	X-ray photoelectron spectroscopy
α HL	α -hemolysin

C	Ion concentration
C_D	DNA concentration
D_{di}	Diffusion coefficient of DNA
D_L	Diffusion coefficient of lipid
E	Electric field intensity
E_{max}	Maximum electric field intensity
F_{en}	Entropic energy in the analytical model
F_{el}	Electrophoretic energy in the analytical model
F_{ep}	Electrophoretic force
G	Total nanopore conductance
G_b	Bulk conductance
G_s	Surface conductance
h	Membrane thickness
k	Boltzmann constant
l	Distance between each base pair in DNA
M	Number of base pairs can be accommodated in nanopore
N_{strand}	Number of DNA strand in the nanopore
N_{SRP}	Number of size reduced nanopores
N	Number of base pairs
n	Position of DNA molecule
Q	Bare charge carried per base pair
Q_{eff}	Effective charge carried per base pair
R_H	Hydrodynamic radius
R	Radial distance away from nanopore
R^*	Capture radius of nanopore

R_c	Capture rate of DNA molecules
r_{DNA}	Radius of dsDNA molecule
r_L	Large radius of conical nanopore
r_S	Small radius of conical nanopore
S_{min}	Minimum horizontal cross-sectional area of nanopore
V	Applied bias voltage in the analytical model
ΔG	Change of Gibbs free energy in system
ΔH	Change of enthalpy in system
ΔS	Change of entropy in system
ΔV	Voltage drop across the membrane
ε	Permittivity of the solution
ε_{HY}	Hydrophobic energy
ε_Q	Electrostatic energy
ζ	Zeta potential
η	Viscosity of the solution
θ	Conical angle of nanopore
κ	Parameter denoting the local friction of the base pair
λ_D	Debye length
μ	Ion mobility
μ_{ep}	Electrophoretic mobility of DNA
μ_{os}	Electroosmotic mobility
σ	Conductivity of the solution
σ_s	Surface charge density of the nanopore
τ	Mean translocation time
v_{ep}	Electrophoretic velocity
v_{os}	Velocity of electroosmotic flow

1. Introduction: The hole story

How a tiny hole can serve as an exploring tool for the mankind to “observe” the world? The answer may vary greatly through history. In the 5th century B.C., the Chinese philosopher Mozi recorded the formation of an inverted image with a pinhole and presupposed the pinhole phenomenon as a demonstration that light travels in straight lines. Till the 16th century, this image-forming ability of a tiny hole led to the invention of camera obscura and the development of pinhole photography [1]. Into the 20th century, the brilliant technology advances have made it possible for us to witness the celestial beauty through space telescopes with sophisticated pinhole cameras. Towards the other end of observing scale, an idea of using a nanosized hole to probe biomolecules arose a mere few decades ago. This new type of pinhole “camera” is called nanopore sensor. In less than three decades, the nanopore sensor has proven to be a surprisingly powerful tool to interrogate individual biomolecules including nucleic acids and proteins. Applications of this tiny nanopore offer a giant glimpse into the future for advancing biological science and improving human healthcare, one of the most important being reading the sequence of nucleobases of a DNA strand. Today, with having the envisioned future in mind, thousands of researchers, hundreds of laboratories and about a dozen of commercial enterprises worldwide are striving in the nanopore field to explore the full potential of this tiny hole.

1.1 Emergence of nanopore sensors

It might appear a bit cliché to quote Richard Feynman’s landmark lecture *“There’s Plenty of Room at the Bottom”* to introduce nanotechnology at the start. However, after revisiting his famous talk, you would always find it remarkably prescient about how life science will advance when envisaging if we can maneuver and observe entities down to nanoscale, as he stated in 1959: *“What are the most central and fundamental problems of biology today? They are questions like: What is the sequence of bases in the DNA? What happens when you have a mutation? How is the base order in the DNA connected to the order of amino acids in the protein? ...”* “... It is very easy to answer many of these fundamental biological questions; **you just look at the thing!** ...” [2]

Indeed, to truly look into the marvelous biological system at nanoscale, we need experimental techniques that is not just time-averaged and population-based conventional methods, rather is to probe and identify single-molecules directly and resolve their structure and spatial dynamics in real-time. In the mid 1990's, a method of doing so started entering the stage, known as nanopore technology [3]. The principle of this method is exceedingly simple: a nanometer-sized pore that spans across an insulating membrane connects two chambers containing electrolyte solutions, and a constant ion flow through the pore forms when applying an external bias voltage across the membrane. If biomolecules are present in the solution, they will partially impede the ion flow when driven through the pore electrophoretically and/or electroosmotically. Typically, by analyzing ionic current changes, characteristic information of the passing molecules can be extracted. Figure 1.1 depicts a schematic diagram of the working principle of nanopore sensor.

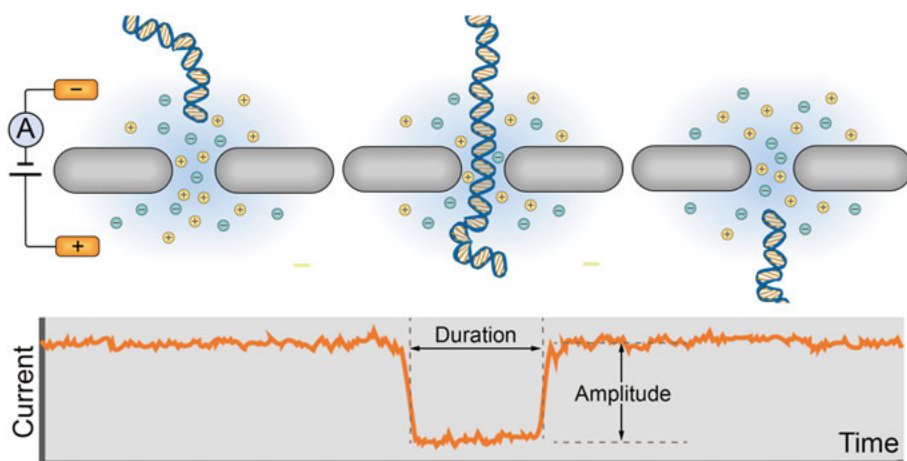


Figure 1.1. A schematic showing the principle of single-molecule nanopore sensing techniques.

This operating principle of nanopore is a reincarnation of the classic Coulter counter, which is a hole-based sensing technique to count and size particles that can be traced back to the 1950's. However, the vast gap between the two techniques is that the hole is not of millimeter or micrometer but of nanoscale dimensions, which provides a sensing capability of target analytes at the single-molecule level. This exciting leap sparks an ambitious goal of using nanopores for DNA sequencing, where a linearized single-strand DNA (ssDNA) threads through the nanopore and individual bases can be directly identified from the changes of ionic current blockades during the translocation. Two significant features of nanopore sequencing are envisioned: (1) amplification of the DNA is not required and (2) the nucleobase sequence of much longer strands can be determined. This promise has fuelled the boom of nanopore

research in academic and industrial interest over the last two decades. In 2012, with the development of enzyme-based methods of ratcheting polynucleotides through the nanopore, the first sequence read of DNA strands using nanopores was published [4]. Two years later, Oxford Nanopore Technologies (ONT) released the first commercial nanopore sequencer MinION, a compact and portable device weighing only about 100 g shown in Figure 1.2.

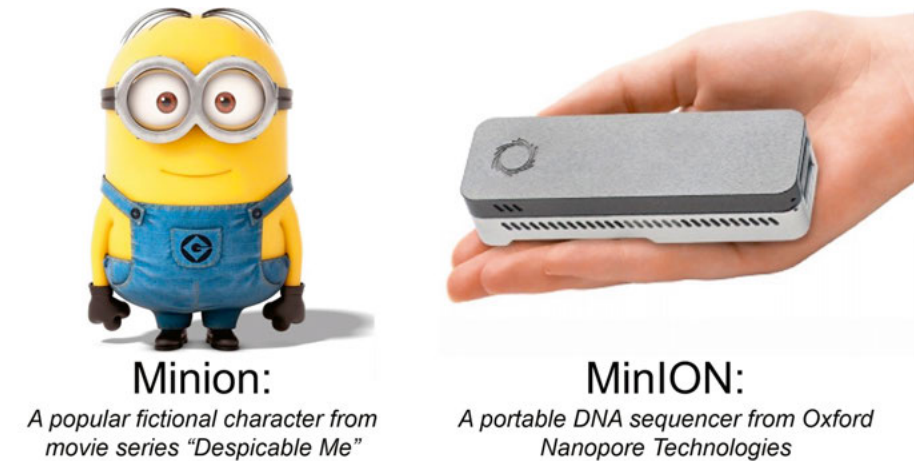


Figure 1.2. A demonstration of the difference between the popular movie character Minion and the first nanopore DNA sequencer MinION from ONT.

From the earliest radical proposal of nanopore sequencing to the ongoing commercial realization of sequencing instruments, it shows the immense potential of nanopore sensor as a single-molecule sensing tool. Today, not only in the context of DNA sequencing, nanopore-based sensing is rapidly developing in expanding applications, such as fundamental biophysical studies[5], clinical diagnostics [6, 7], biological screening [8] and even protein sequencing [9, 10].

1.2 Biological vs. Solid-state nanopores

How to obtain a tiny pore in an insulating membrane then? Thanks to the rapid advances in bio- and nanotechnologies, two major types of nanopores have been developed for biosensing purposes.

The first type consists of biological protein pores that exist in almost every living thing on the planet. They are a vital type of nanoscale machinery that serves a variety of functions in nature, including gating ion flow for chemical energy generation, shaping action potentials for nerve signaling, regulating biomolecular transportation across the cell membrane, and much more. Among a plethora of protein pores, two in particular have been widely used in

the nanopore research: α -hemolysin (α HL) and *Mycobacterium smegmatis* porin A (MspA), with diameters of 1.4 nm and 1.2 nm at the narrowest channel region, respectively, comparable with the width of ssDNA (0.9 ± 0.1 nm). The first DNA translocation experiments were performed using α HL pores [11]. According to the resistive pulse sensing principle, the ionic conductivity is particularly sensitive at the constriction region, so the narrowest aperture part of the nanopore serves as its sensing region. MspA has an aperture length about 0.6 nm [12] and an effective sensing length of about 1.2 nm [4, 13], which is much shorter than α HL as shown in Figure 1.3. With using a DNA polymerase as a molecule motor to slow down the DNA translocation velocity, the first read of DNA sequence by nanopore was accomplished on the MspA pore [4].

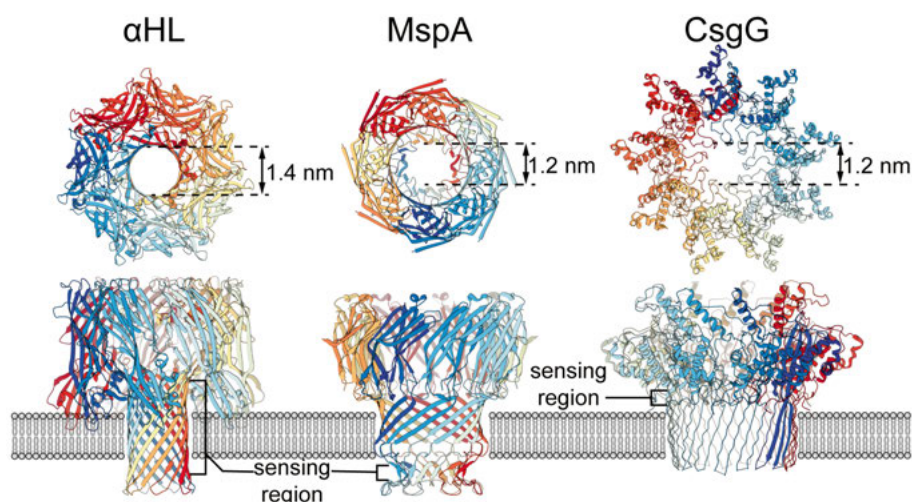


Figure 1.3. Three representative biological pores: α HL (PDB ID: 3M4D), MspA (1UUN) and CsgG (4UV3). Protein structure images are obtained from Protein Data Bank (PDB) (www.rcsb.org) with the sensing region and narrowest pore diameter indicated.

There are numerous desirable properties of biological pores: they have extremely reproducible geometry at the atomic level; they can self-insert into the lipid bilayer membrane that has very low capacitance and excellent noise performance in electrical measurements; they are versatile to be mutated by genetic engineering to tweak their physical and chemical features on specific sites. Currently, the nanopore DNA sequencers from ONT uses a heavily engineered mutant amyloid secretion channel, CsgG [14](shown in Figure 1.3). While biological pores have enabled DNA sequencing, for future sensing of an expanding analytes and manufacturing with a scalable approach, they are ill-suited due to their small diameters preventing the detection of large analytes and the intrinsic fragile nature of lipid bilayer and protein pores. They

can be easily damaged by mechanical stresses, high electrical field, temperature variations and harsh pH and this further limits the integration of biological pores with other nanodevices.

Being aware of the limitations of biological pore, a second type of nanopores was developed by fabricating pores on solid-state membrane materials, usually named solid-state nanopores. Compared to their biological counterparts, solid-state nanopores have a wide-range tunability in pore geometries and dimensions as well as excellent mechanical robustness and stability.

Over the last decade, various materials have been used to fabricate the free-standing membrane, such as Si [15], Al_2O_3 [16], TiO_2 [17], HfO_2 [18], and 2D materials like graphene [19], MoS_2 [20] and transition metal carbides (MXenes) [21], while the most widely used is SiN_x . Meanwhile, a handful of approaches have also been developed to generate pore structures on the existing thin membrane, with each approach having its own advantages and limitations. Figure 1.4 shows the schematic illustrations of some common fabrication techniques that are discussed in the following paragraph.

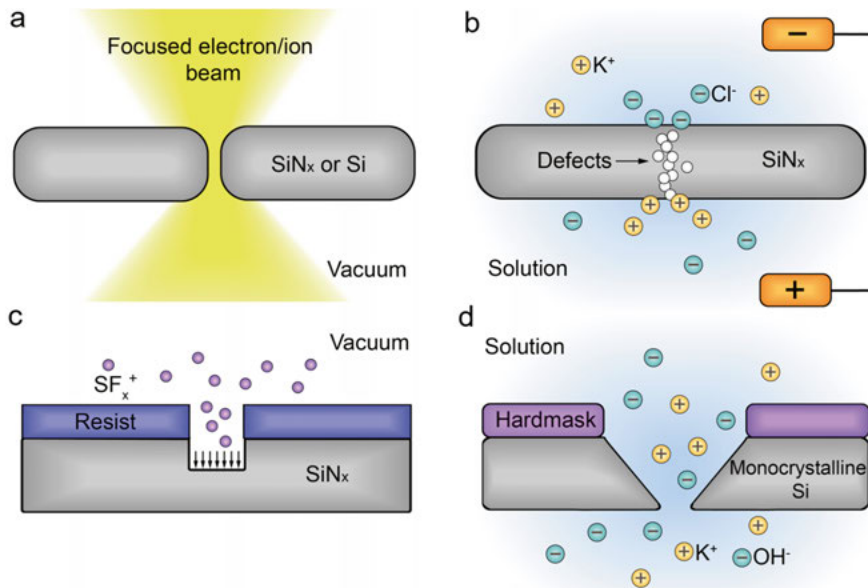


Figure 1.4. Fabrication methods of solid-state nanopores: (a) direct drilling by focused electron/ion beam; (b) controlled dielectric breakdown; (c) lithography combined with reactive ion etching; (d) lithography combined with wet chemical etching.

For instance, direct drilling techniques of using focused ion/electron beam with an ion microscope or a transmission electron microscope (TEM) can achieve reliable sub-10 nm pore size [22-24]. Particularly, the current state-of-the-art TEM-based drilling can fabricate pores down to a single-nanometer level [25], making it the main workhorse of nanopore fabrication. However,

both methods share considerable drawbacks of high cost, low throughput and instrumentation availability. In contrast, controlled dielectric breakdown (CDB) serves as a simple and cost-effective pore making strategy [26-28]. In CDB, by applying high electric field across the insulating membrane in the electrolyte solution, single nanopores as a result of localized breakdown will form at a random position on the membrane [29]. Though CDB is an attractive alternative to beam-based drilling techniques, it suffers from the incapability of forming multipore arrays to realize parallel detection. Another group of nanopore fabrication techniques is based on the lithographic process combined with different etching processes, including dry etching, wet chemical etching and electrochemical etching [30-32]. With using these processes well-established in the semiconductor industry, this group of strategies can easily achieve massive production of nanopore devices with a range of pore sizes and various arrangements. However, it is difficult for this type of methods to fabricate sub-10 nm pores reliably due to the variation along the multistep fabricating process and the spatial resolution of lithography. Therefore, post pore shrinking by deposition or oxidation is usually needed to obtain desirable pore size [33-35]. Figure 1.4 shows the schematic illustrations of the mentioned fabrication techniques.

It appears that an arsenal of fabrication techniques is already available to obtain different types of solid-state nanopores, yet still a series of challenges lies ahead to realize high-selectivity and high-sensitivity biosensing, as the performance that biological pores reached for DNA sequencing.

1.3 Surface tailoring for solid-state pores

One major challenge to be addressed for solid-state nanopores is its surface incompatibility with biomolecules. This mainly concerns two aspects of the solid-state surfaces: one is the tendency of pore surfaces to non-specifically adsorb biomolecules, which may lead to clogging of the pores and affect the sensing efficacy; the other one is the lack of functional groups on pore walls such as carboxylic acid and amines, unlike biological pores, to site-specifically modify pore properties or tether receptor ligands.

The nonspecific interaction between analytes and pore walls is an outcome of hydrophobic interaction, electrostatic attraction, and van der Waals forces [36]. To reduce the strength of all the contributing forces, applying surface coatings is the most effective solution by utterly refashioning surface properties. Organic coatings are commonly employed through various coating strategies, such as physisorption of surfactants [37, 38], layer-by-layer self-assembly of charged polymers [39, 40], chemical modification via salinization [41], self-assembled monolayers (SAM) of thiols on gold [42-44], and coating of the fluid lipid bilayer [45, 46]. The majority of organic coating strategies are

solution-based and self-assembled processes, which enable a continuous coverage of the coating layer on the inner pore surfaces. While applying organic coatings has proven to be effective for reducing nonspecific interaction, long-term stability and success rate of preparing high-quality organic coatings remain challenging for quantitative and reproducible nanopore experiments. Figure 1.4 shows the illustrated representations of common organic coating strategies for solid-state nanopores.

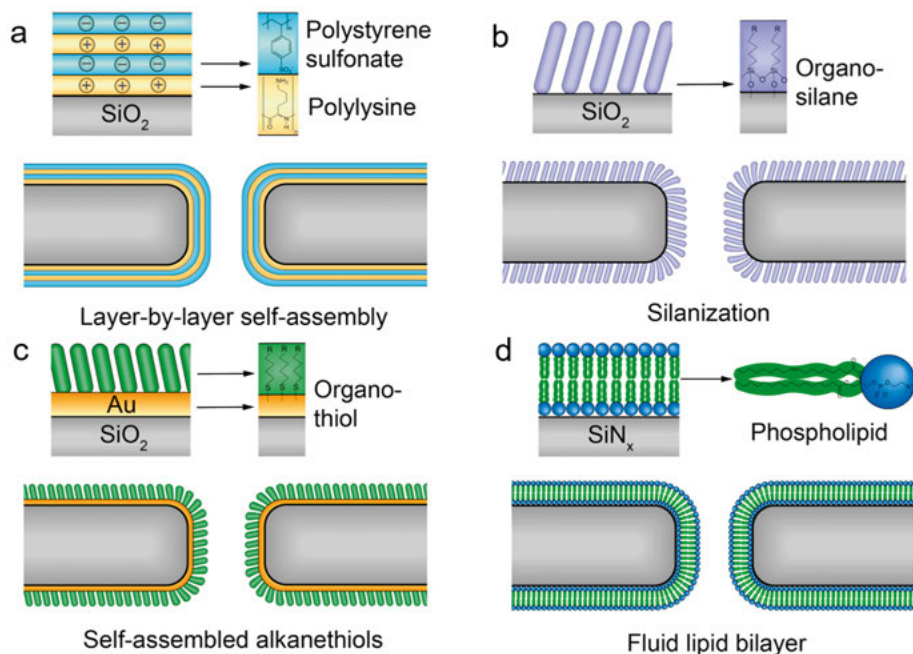


Figure 1.5. Idealized illustration of the common organic coating strategies for solid-state nanopores: (a) coating prepared by layer-by-layer self-assembly of negatively and positively charge polymers; (b) coating prepared by silanization; (c) coating of SAM by alkanethiols on gold; (d). coating with a fluid lipid bilayer.

Alternatively, deposition of inorganic materials by means of atomic layer deposition (ALD) inside the nanopore is a well-suited deposition method because ALD can conformally cover the recessed feature of nanopore [47, 48]. More importantly, it can achieve atomic precision with an excellent control of layer thickness and uniformity [49]. In contrast to organic coating methods, inorganic coating by means of ALD is easy to operate and stable to various conditions. However, it is relatively neutral to minimize nonspecific interactions because mere electrostatic attraction can be altered by employing materials with different surface charge properties.

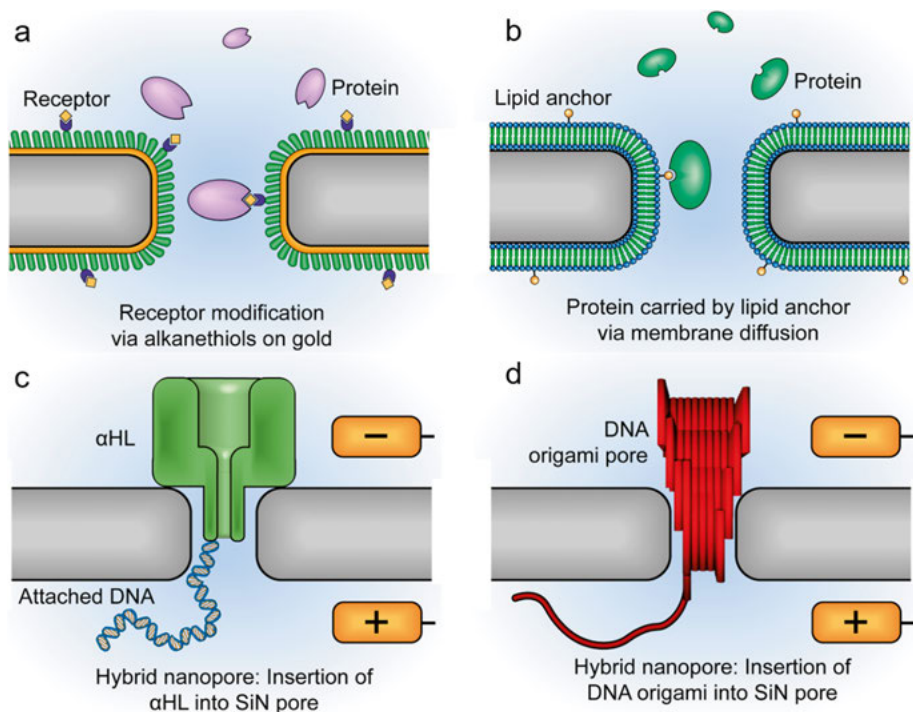


Figure 1.6. Idealized illustrations of receptor modification or insertion of biological pores into solid-state nanopores: (a) a protein molecule captured by a nanopore modified by SAM of alkanethiols on gold; (b) a protein molecule carried through a nanopore via membrane diffusion of a lipid anchor; (c) insertion of a α HL into a solid-state nanopore; (d) insertion of a DNA origami pore into a solid-state nanopore.

For improving sensing selectivity, introducing active ligands on the pore walls to prolong the residing time of target analytes has proven to be a promising route. It is mainly achieved based on surface coating methods with using a mixture of coating reagent that parts of it are anchored with receptors. For instance, metallized SiN_x nanopores modified with nitrilotriacetic-acid receptors via a thiol-terminated SAM allowed observation of reversible binding and unbinding of proteins inside nanopores [44]. Likewise, a biomimetic approach was developed employing lipid bilayer coating with certain lipids with receptors to capture and carry proteins through the pore via lipid membrane diffusion [46]. This method showed the potential of using solid-state pores to estimate the protein shape and dipole moment [45, 50]. In addition, another strategy able to achieve pore functionalization is to dock or attach a biological pore to a solid-state pore. Ideally, this hybrid type of nanopore could combine the advantages of both two types of pores. The first demonstration was realized by electrophoretically inserting a DNA tethered α HL pore into a 3.6 nm SiN_x pore [51]. Other demonstrations of hybrid pores using DNA origami channels

[52] and viral portal proteins [53] were later achieved. Yet, signal fluctuations are often observed in the hybrid pore system, mainly caused by the loosely fixed protein pores resulting in leakage current. Figure 1.6 shows the illustrations of aforementioned functionalization strategies.

1.4 Electrical vs. Optical nanopore sensing

The aforementioned surface dressing strategies for solid-state nanopores keep trying to better mimic their biological analogues. However, from a materials and engineering perspective, solid-state nanopores offer a remarkable versatility of inventing novel architectures and enabling various sensing modalities, which biological pores do not possess. This great versatility renders higher chances for nanopore technology to achieve multiplexed detection, high-throughput analysis, and enhanced sensing selectivity and sensitivity.

In general, the emerging sensing strategies can be classified into two categories: electrical sensing and optical sensing. For electrical sensing, apart from the prevalent ionic current detection based on resistive pulse sensing, integrating nanopores with field-effect transistor (FET) and quantum tunneling junctions have been explored. The sensing principle for FET is based on monitoring the change in source-drain conductance upon binding/attaching of charged analytes on the gate surface [54]. By integrating FET with nanopore, it allows an active transport of the analyte to the transistor to facilitate the detection, and in the meantime the nanopore-based ionic current measurements can be synchronized (as illustrated in Figure 1.7a). In the case of DNA sensing, FET signals are generated from a change in local potential at the gate induced by capacitive coupling during DNA translocation [55, 56]. FET structures incorporated with nanopore using Si nanowires [55], graphene nanoribbons [57, 58], carbon/gold electrodes [59] have been successfully demonstrated to achieve DNA detection. In a similar but different fashion, a quantum-tunneling configuration of two electrodes placed close to each other can be built into nanopore structure to form a tunneling junction (as illustrated in Figure 1.7b). The idea of this approach is to use tunneling current to probe the translocating DNA and differentiate single nucleotides with the advantage of near-atomic resolution of tunneling effect, as initially demonstrated by scanning tunneling microscopy (STM) [60]. Particularly, 2D materials like graphene [61, 62] and MoS₂ [63] have been demonstrated to be the promising candidates as the electrode materials, as their atomic thickness and high conductivity can achieve the ultimate spatial resolution for individual nucleotides and amino acids. Nevertheless, for the sophisticated integration of FET and quantum tunneling, extensive fabricating optimization and surface functionalization are still needed to achieve a high device yield and sensing selectivity.

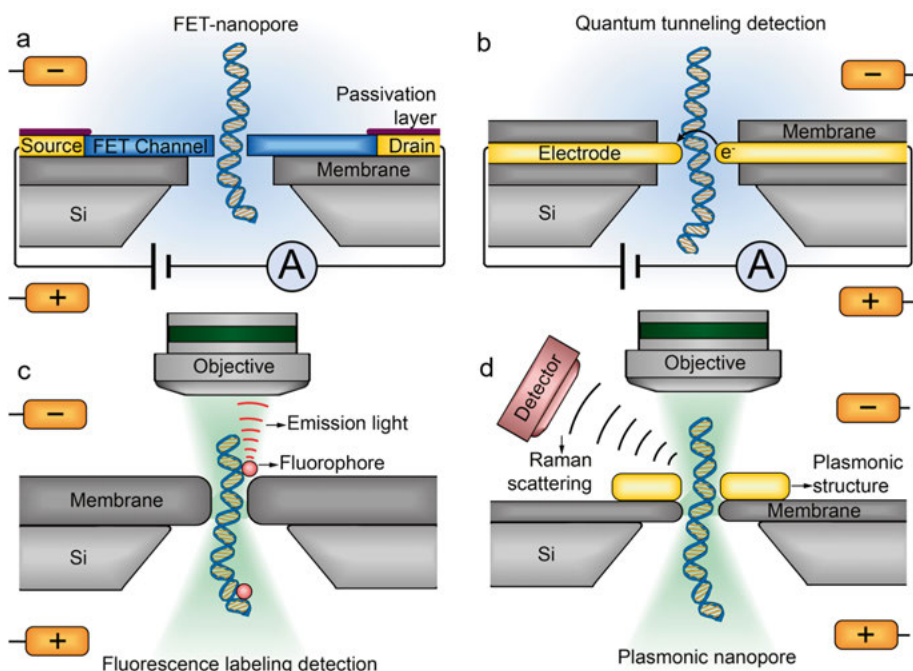


Figure 1.7. Illustrations of different sensing modalities: (a) integration nanopore with FET structure; (b) integration nanopore with tunneling junction; (c) fluorescence detection of labeled analytes; (d) Raman scattering detection with plasmonic nanopores.

Although substantial progress has been made to improve the performance for electrical sensing on solid-state nanopores, to date, two major factors have been stunting employing electrical sensing for real-life applications: noise and throughput. The electrical signal collected from nanopore measurements is often hindered by non-ideal noise spectra, especially at high bandwidth (≥ 100 kHz) for achieving high temporal resolution [64]. At low frequencies (< 100 Hz), flicker ($1/f$) noise associated with many physical phenomena dominates. At high frequencies (> 1 kHz), dielectric noise associated with the capacitance of device materials dominates [65, 66]. The noise behavior of solid-state nanopores is regarded as a key limiting factor of resolving fine molecular features, which single-molecule sensing generally requires. Furthermore, the throughput of electrical sensing, particularly for ion current measurement, is often limited to a single nanopore. It is engineering challenging to construct a massive pore array with each nanopore having individual electrode and reservoirs. If multiple pores share a same pair of electrodes, current signals from individual pores will be convoluted and subtle changes cannot be discriminated [67].

To complement the deficiency of electrical sensing, there has been a drive to develop optical sensing strategies. As a fundamentally independent method

from electrical sensing, optical approach can provide extra information on top of ionic current that relies on photons rather than electrons [68]. The typical optical sensing approach is to detect the fluorescently labelled molecules that are temporally confined in nanopores via fluorescence microscopy (as illustrated in Figure 1.7c). Importantly, optical signals from individual pore can be separately analyzed with retained single-molecule resolution, which allows high detection throughput by using pore arrays in the same membrane. In addition, fluorophores covering a broad spectral range enables versatile strategies to discriminate molecular structure. One of the pioneer work is using two types of fluorophore barcode to achieve optical recognition of different DNA sequence on nanopore arrays [69]. Also, the diffusive and voltage-drive motion of DNA molecules has been observed by tracking the fluorescence emission from dye-labelled DNA [70-73]. On top of labelling analytes and introducing ion dye indicator, building plasmonic structure onto nanopore has been another striving direction for optical sensing [74-76]. Plasmonic nanostructure can produce a localized electromagnetic field, known as plasmon resonance, which can enhance the light intensity and attenuate background noise (as illustrated in Figure 1.7d). Thereafter, plasmonic nanopores are particularly powerful to readout optical signals, including scattering light, Raman scattering and fluorescence. For example, an enhancement of fluorescence by a factor of 10 was achieved for a single dye-labelled DNA using a plasmonic nanowell [77].

Nevertheless, as an emerging field, optical nanopore sensing has several issues to be addressed with continuous efforts, such as photoluminescence of membrane materials, photothermal heating induced bubble generation and thermophoresis, and photoconductive effect caused interference for high-bandwidth optoelectrical sensing.

1.5 Scope of the thesis

As previous sections have alluded, various efforts are needed to push forward the ever-growing field of solid-state nanopore sensing, including surface tailoring to minimize nonspecific interaction and introducing specific binding site, parallel detection with multipore arrays to improve throughput, and complementation with optical readout to gain extra information beyond ionic current. This thesis aims to make contributions toward all aforementioned points, to be more specific, to engineering surfaces of solid-state nanopore arrays for optical-based sensing of biomolecules. Towards this objective, novel and existing surface tailoring strategies have been developed and adopted for solid-state nanopore arrays, and based on that, several dynamic processes associated with pore surfaces have been studied through optical observation. The structure of this thesis, following the introduction chapter, can be summarized as follows:

Chapter 2 introduces the fundamental theories at the intricate interfaces of solid/solution/biomolecule in a nanopore sensing system, which provides the basic information for discussions in the following chapters. Subsequently, the main work of this thesis is divided into four parallel chapters based on the three surface tailoring strategies used and the corresponding studies.

Chapter 3 demonstrates a novel and versatile surface patterning technique for site-specific immobilization of target analytes (Paper I), which has proven to be compatible with nanopore array structures (Paper II).

Chapter 4 focuses on an adaption of lipid bilayer coating on truncated pyramidal shape pores and the corresponding study of its formation mechanism and kinetics (Paper III), as well as the optical observation of its anti-adsorption property for DNA translocation (Paper IV).

Chapter 5 presents the effort for obtaining a photoluminescent-free and durable nanopore by depositing HfO_2 on Si pore arrays, and the investigation of DNA clogging dynamics relied on the device (Paper V).

Chapter 6 shows the attempts of docking DNA polymerase onto solid-state nanopores by utilizing the detection methods of both ionic current measurement and label-free optical observation (Paper VI).

Finally, Chapter 7 summarizes the different attempts of surface engineering strategies, concludes the gained knowledge and briefly outlines the future outlooks.

2. Theoretical background: Interface matters

The aphorism “God made the bulk; surfaces were invented by the devil.” attributed to Wolfgang Pauli, seems to be spot-on when applying in the field of solid-state nanopore sensing. In this intricate interfacial system of solid/solution/biomolecule, knowing the basis of surface physics and chemistry is necessary for the understanding of surface associated phenomena and problems. In this chapter, basics of electrostatic properties at the interfaces and nanopore conductance are first introduced in section 2.1 & 2.2; essential electrokinetic phenomena in the electrolyte solution are focused in section 2.3; surface chemistry of $\text{SiN}_x/\text{Si}/\text{SiO}_2$ erosion in electrolytes is brought up in section 2.4; different biomolecule-surface interactions are briefly summarized in section 2.5. These provide the theoretical background for the later discussions in the characterization of fabricated nanopores and the investigation of surface associated dynamic processes in the following chapters.

2.1 Surface charge & Electrical double layer

When an object is exposed to a fluid, surface charges are often formed at the interface. The object might be a solid surface, a DNA strand, a protein complex, even a gas bubble or another type of liquid droplet. In the nanopore system, the concerned objects bearing surface charges are the solid-state membrane and the biomolecular analytes. For different materials, several proposed mechanisms for developed surface charge are: adsorption of mobile ions, ionization of surface groups (acidic or basic groups), dissolution of ions from crystal lattice. Besides, at the presence of an across membrane electric field, induced charge can generate on the surface of dielectric material due to polarization [78].

To describe the surface charge property of a solid material or a molecule in an aqueous solution, point of zero charge (PZC) or isoelectric point (pI) is generally used, which refers to the pH value at which the net surface charge is zero. For molecules, their pI value can be directly obtained from their acid dissociation constant value pK_a . For example, an amino acid with only one amine and one carboxyl group, the pI can be calculated from the mean of the two pK_a values of this molecule: $\text{pI} = (\text{pK}_{a1} + \text{pK}_{a2})/2$. In the case of DNA, the backbone of DNA is linked by phosphodiester bonds containing phosphate group. Because the phosphate group has a pK_a near 0, DNA molecules are

negatively charged at the physiological pH of 7.4. For the widely used membrane materials, SiN_x and SiO_2 have PZC value around 4 and 2 [79, 80], respectively. When the solution pH is higher than the PZC, SiN_x and SiO_2 surfaces become negatively charged via deprotonation. The net surface charge will form an electrostatic field. To reach equilibrium, this electrostatic field, in combination with thermal motion of the ions, attracts the counter charge ions to the vicinity of the surface, which electrically screens the net surface charge. According to the Gouy-Chapman-Stern theory, a two-layer structure forms, known as the electric double layer (EDL) [81]. The internal layer called the Stern layer is comprised of adsorbed ions, which are immobile relative to the surface. The outer layer called the diffusive layer, where the distribution of ions is governed by local potential and follows the Boltzmann distribution. In turn, the distribution of ions shapes the local potential via the Poisson equation. By solving a linearized Poisson-Boltzmann model proposed by Peter Debye and Erich Hückel, two important characteristic parameters can be extracted, Debye length λ_D and zeta potential ζ [81].

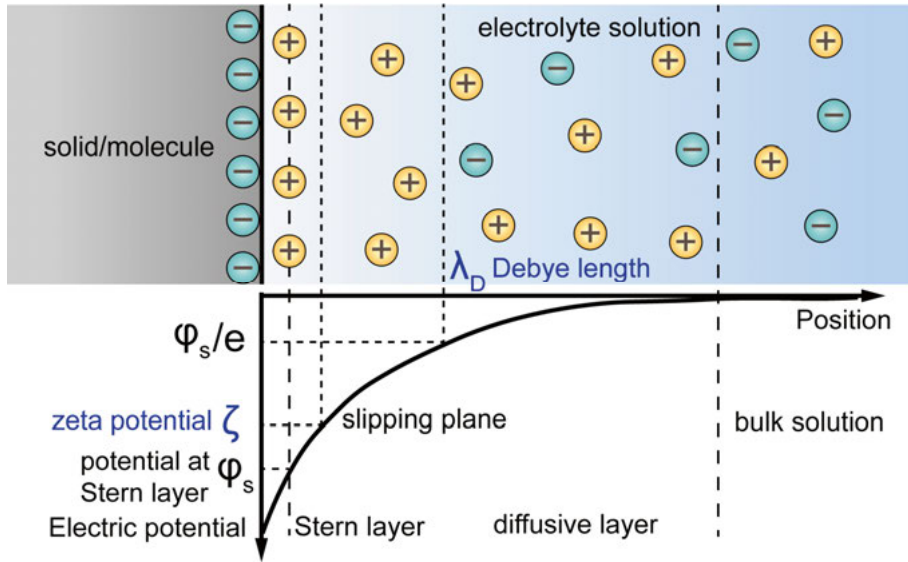


Figure 2.1. A schematic of the electric double layer using the Gouy-Chapman-Stern model. The charge distribution and potential profile at a negatively charged surface are illustrated and important parameters are indicated.

The Debye length λ_D is a decay constant that equals the perpendicular distance from the surface to the point where the electric potential decreases to e^{-1} of the surface potential. It describes the length scale of the screening effect of EDL. In electrolyte solution with monovalent ions, the Debye length is expressed as

$$\lambda_D = \sqrt{\frac{kT\varepsilon}{2N_A e^2 C}} \quad (2.1)$$

where k is the Boltzmann constant, T absolute temperature, ε the permittivity of the solution, N_A Avogadro's number, e the unit charge and C the molar ion concentration. For 1 M and 100 mM KCl solution, λ_D is about 0.3 nm and 1 nm, respectively. Zeta potential ζ is defined as the electric potential at the slipping plane, which is the boundary plane between the Stern layer and diffusive layer. ζ is regarded as the apparent surface potential that is a critical parameter in studies of electrokinetic phenomena, and also a key indicator to evaluate the degree of electrostatic interactions between adjacent charged surfaces in the solution.

2.2 Pore conductance: Bulk & Surface

An understanding of the conductance of a nanopore is the basis for any nanopore study, especially for electrical measurements. In general, at a high salt concentration, *e.g.* 1 M KCl (commonly used for nanopore experiments), the effect of surface charge on pore conductance can be neglected due to a small λ_D of the EDL as previously discussed. In this case, only the bulk ionic conductance of the pore is considered. The bulk conductance is determined by two parts, the pore resistance and the access-region resistance. For a simple and ideal cylindrical pore geometry, with the assumption of a uniform electrical conductivity, the total pore conductance is expressed as [82]

$$G = \sigma \left(\frac{4h}{\pi d_p^2} + \frac{1}{d_p} \right) \quad (2.2)$$

where σ is the solution conductivity, h the membrane thickness and d_p the pore diameter. The first term in the parentheses represents the pore volume resistance and the second term describes the resistance of two access-regions. To treat various pore geometries conveniently, such as hour-glass, conical and truncated-pyramidal shapes, a versatile conductance model based on the concept of effective transport length L_{eff} has been introduced by Wen *et al* [83]. L_{eff} is defined as the distance along the pore axis (perpendicular to membrane) between the two points in each reservoir, where the electric field intensity falls to e^{-1} of the maximum intensity E_{max} in the system (as illustrated in Figure 2.2). According to Gauss's law, the strongest electric field E_{max} exists at the most constraint region for electric field distribution, in this case, at the minimum cross-section area S_{min} in the nanopore. Thus, the total conductance in this model can be described as

$$G = \sigma \frac{S_{min}}{L_{eff}} \quad (2.3)$$

Then, the relationship between L_{eff} and pore geometry can be derived based on Ohm's law and an estimation of the equi-field surface area of the access-region, detailed derivation and expression for different pore geometries can be found in [84]. For example, the L_{eff} of a conical nanopore shape with a conical angle θ can be expressed as

$$L_{eff} = 0.46d_p \left(1 + \frac{1}{\sqrt{1-\sin\theta}} \right), \quad (h > L_{eff}) \quad (2.4a)$$

$$L_{eff} = 0.92d_p + h(1 - \sqrt{1-\sin\theta}), \quad (h < L_{eff}) \quad (2.4b)$$

Since L_{eff} is determined by h and d_p , and S_{min} is determined by d_p , the bulk conductance G can be obtained by substituting L_{eff} into equation 2.3. Or conversely, by measuring conductance G , the nanopore diameter can be calculated, which serves as an alternative way to determine the nanopore size besides using high-resolution electron microscopy.

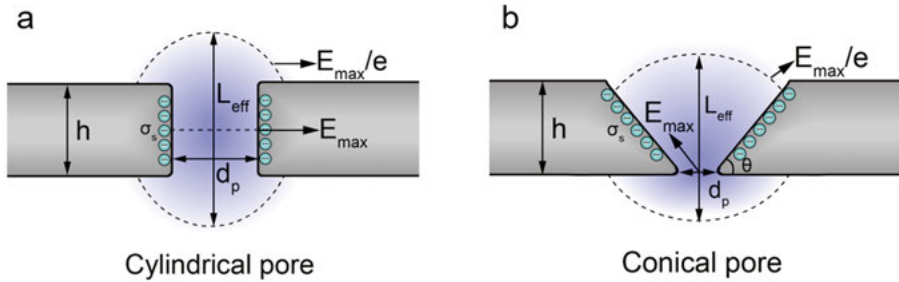


Figure 2.2. A schematic showing the L_{eff} -based conductance model for cylindrical and conical shape pore. Image is not to scale.

If the nanopore diameter is comparable to the EDL thickness, the effect of surface charge on nanopore conductance should be considered. In such a case, the total nanopore conductance G is contributed by two parts: bulk conductance G_b and surface conductance G_s :

$$G = G_b + G_s \quad (2.5)$$

The calculation of bulk conductance has already been discussed above. The surface conductance is determined by the surface charge density σ_s and the corresponding ion mobility μ in the EDL. For a cylindrical shape pore, the expression of G_s is given as

$$G_s = \mu \sigma_s \frac{\pi d_p}{h} \quad (2.6)$$

For a conical pore with an uneven cross-section area, L_{eff} can be used instead of h in the case $h > L_{eff}$. In the case $h < L_{eff}$, same expression as cylindrical pores can be used as an estimation:

$$G_s = \mu \sigma_s \frac{\pi d_p}{L_{eff}}, \quad (h > L_{eff}) \quad (2.7a)$$

$$G_s = \mu\sigma_s \frac{\pi d_p}{h}, \quad (h < L_{eff}) \quad (2.7b)$$

Based on the aforementioned model of bulk and surface conductance model, the nanopore diameter and the surface charge can be extracted by fitting the conductance G obtained at different electrolyte conductivity σ . Later, a real example of extracting surface charge density of nanopore is given in section 5.2.3.

2.3 Electrophoresis & Electroosmosis

Under an electric field, two types of electrokinetic phenomena are of particular interest in the nanopore system. One is electrophoresis, which concerns the motion of charged analytes; the other is electroosmosis, which describes the motion of liquid with respect to the charged surface.

In electrophoresis, the charged objects in the fluid are driven by the electrostatic Coulomb force and will gain a velocity determined by the electrophoretic mobility μ_{ep} and the electric field E :

$$\vec{v}_{ep} = \mu_{ep} \vec{E} \quad (2.8)$$

For large objects, *e.g.* a sphere particle with radius much larger than its Debye length, the surface charge is shielded by the EDL. In this case, the electrophoretic mobility μ_{ep} is given by

$$\mu_{ep} = \frac{\varepsilon \zeta}{\eta} \quad (2.9)$$

where ζ is the zeta potential of the particle, ε and η is the permittivity and the viscosity of the fluid, respectively.

In the case of DNA in a bulk solution, the electrophoretic force posed on DNA is determined by the electric field E and DNA's effective charge Q_{eff} :

$$\vec{F}_{ep} = Q_{eff} \vec{E} \quad (2.10)$$

Q_{eff} is smaller than the DNA's bare charge Q , which is the result of screening of negatively charged phosphate group by tightly associated counter ions, according to the Manning condensation theory. At a monovalent ion concentration of 100 mM, Q_{eff} was found about 25% of Q [85]. In a nanopore system, the DNA molecules freely diffuse when they are far from the pore, because the electric field intensity is negligible there. Close to the pore, there is a non-zero electric field that decays approximately radially away from the mouth of the pore due to the finite access resistance. The voltage in the vicinity of a cylindrical pore can be approximately expressed as

$$V(R) = \frac{d_p^2}{8hR} \Delta V \quad (2.11)$$

where R is the radial distance from the pore mouth and ΔV is the total voltage drop across the system [86]. As a DNA strand approaches the pore, the DNA

motion starts being dominated by the electrophoretic drift at a characteristic length scale, called the capture radius R^* (as illustrated in Figure 2.3). This can be obtained by balancing the diffusive motion against the electrophoretic drift, when setting $V(R^*) = D_{di}/\mu_{ep}$ where D_{di} is the DNA diffusion coefficient [86]. Thus, the capture radius can be written as

$$R^* = \frac{d_p^2 \mu_{ep}}{8hD_{di}} \Delta V \quad (2.12)$$

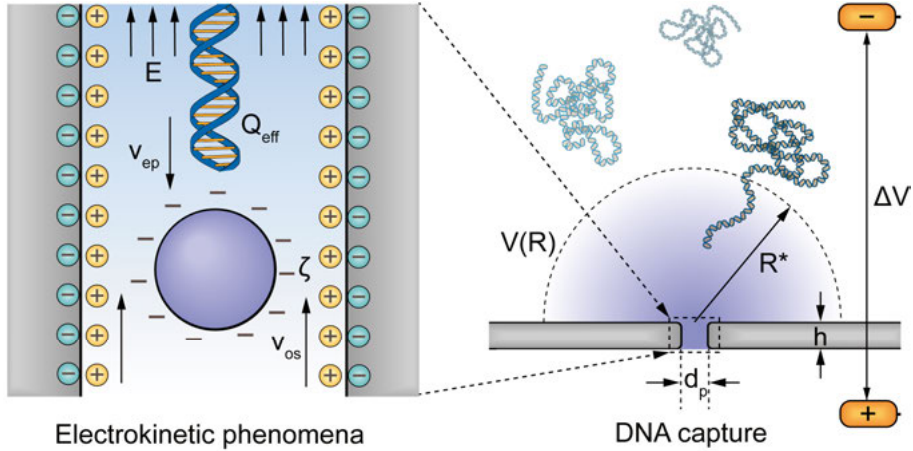


Figure 2.3. Illustrations showing the electrokinetic phenomena inside the nanopore and the capture radius of the nanopore. Image is not to scale.

Assuming that the process inside the capture region is limited by the time required for DNA to arrive at the pore, and not by the final translocation process, a capture rate r_c can be derived by the Smoluchowski theory for absorption by a hemisphere of radius R^* :

$$r_c = \frac{\pi d_p^2 \mu_{ep}}{4h} C_D \Delta V \quad (2.13)$$

where C_D is the DNA concentration. This formalism predicts that, in this diffusion-limited regime, r_c of DNA is proportional to its concentration and the applied voltage, while independent of DNA length, because μ_{ep} is observed to be independent of DNA length above 400 base pairs [87-89]. This barrier-free model has been confirmed to be valid for large solid-state nanopores when capturing double-stranded DNA (dsDNA) molecules, as indicated by the linear dependence of the capture rate on voltage [86, 90]. In contrast, for small pore diameters, such as protein pores, there is a free energy barrier against DNA threading through the pore. This energy barrier can originate from the confinement of DNA end in the coiled configuration, as well as possible unfavorable interactions of the highly charged DNA with the pore. In this case,

the r_c has an exponential dependence on voltage, which has been experimentally observed and theoretically explained [86, 91]. All the experiments performed in this thesis are done in the diffusion-limited regime, and a later discussion of DNA translocation frequency in section 5.2.1 involves this model.

In electroosmosis, the counterions in the diffusive layer of EDL migrate under an electric field tangential to the charged surface. This motion of ions will drag water molecules along with them, which forms a liquid flow, called electroosmotic flow (EOF), see Figure 2.3. In the nanopore system, EOF often exists in the nanopore channel and imposes an additional force on the translocating analytes. Depending on the net charge of the molecule and the charge polarity of pore walls, EOF can either plays as a countering or an accelerating role to the electrophoretic force. Similar to electrophoresis, the velocity of EOF can be written as

$$\vec{v}_{os} = \mu_{os} \vec{E} \quad (2.14)$$

where μ_{os} is electroosmotic mobility. If the Debye length on the pore wall surface is much smaller than the pore diameter, μ_{os} in the nanopore can be expressed as

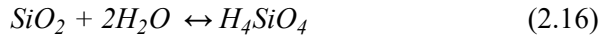
$$\mu_{os} = -\frac{\epsilon\zeta}{\eta} \quad (2.15)$$

For moderately charged and neutral analytes, such as certain proteins or nanoparticles, EOF is the dominating driving force for the translocation through the nanopore.

2.4 Erosion of SiN_x/Si/SiO₂ surface

As discussed in section 2.2, the nanopore conductance is determined by the pore size and its geometry, and especially sensitive to the pore diameter. Therefore, the stability of nanopore diameter is critical for quantitative and reproducible nanopore experiments. SiN_x is the most widely used membrane material for fabricating nanopores and considered chemically and mechanically robust, *e.g.*, SiN_x pores can be aggressively cleaned by a hot Piranha solution (a mixture of H₂SO₄ and H₂O₂) or an O₂ plasma treatment before measurements. However, it has been noticed that the diameter of SiN_x nanopore gradually enlarges in the electrolyte solution, indicating a slow erosion of SiN_x. It has been found that, for TEM-drilled SiN_x pores, there is a thinned ring around the pore where N is depleted and Si/SiO₂ is rich [92]. For SiN_x pores fabricated by the lithographic process with reactive ion etching (RIE), SiO₂ is also found at the pore walls with a less extended Si-rich region [92]. Thereafter, the slow degradation of Si and dissolution of SiO₂ in water are believed to be one of the reasons for SiN_x pore expansion [92, 93]. This phenomenon has been studied in great detail previously, *e.g.* in the context of seawater minerals [94] and biocompatibility of Si/SiO₂ nanoparticles [95]. It

is because that the Si/SiO₂ material surface is hydrolytically unstable and dissolves overtime into water-soluble silicic acid, and the following equilibrium is established:



In the nanopore experiments, a variety of factors can affect the etch rate of this erosion process, including salt concentration, temperature, pH value, and applied voltage [92, 96-98]. Under certain conditions, for example, high applied voltage or high salt concentration under continuous operation, the etch rate can be sufficiently fast to result in a noticeable pore expansion and uncertainty in quantitative experiments. Additionally, this erosion reaction has been used to thin down SiN_x membrane and fabricate pores under laser illumination [99-101], in which the authors argued that the etching of SiN_x is accelerated for Si-rich membrane as a result of accelerated dissolution of SiO₂ in higher pH and elevated temperature [99, 102]. In Chapter 5 and Chapter 6, coating of HfO₂ on Si nanopores is employed to prevent pore expansion in repeated measurements.

2.5 Surface-biomolecule interactions

Surface-biomolecule interactions have always been one of the central topics in the biosensing field [103-105]. In nanopore sensing, the interactions become even more prominent due to the nanoscale confinement of the biomolecule and is inseparable for any nanoscale interface problem. As briefly mentioned in Chapter 1, untreated solid-state surface can non-specifically adsorb various biomolecules, which is troublesome for potential nanopore sensing of complex biological fluids, such as serum, urine or cerebrospinal fluid. Therefore, understanding the interactions between biomolecules and surfaces is crucial to engineer surfaces with desired properties for nanopore applications.

In particular, as an increasingly common analyte, proteins are prone to interact with solid surfaces. As proteins are composed of amino acids with side groups having either positive or negative charge, or being polar or apolar, it makes proteins both amphiphilic and amphoteric [106]. The latter is often related to the net charge that protein carries at physiological pH. Hence, protein-surface interactions are a result of a wide range of physicochemical interactions, which are driven by interfacial energy differences, including increasing entropy, Coulomb forces and hydrogen bond [106, 107].

To evaluate if proteins will be adsorbed onto the surface, the change of Gibbs free energy ΔG provides the criteria [106], which is defined as

$$\Delta G = \Delta H - T\Delta S \quad (2.17)$$

where ΔH is the change in enthalpy, T absolute temperature and ΔS the change in entropy. If $\Delta G < 0$, protein adsorption occurs. If $\Delta G > 0$, surface repulses protein. First, electrostatic interaction is one of the factors that can influence

both protein and DNA, because DNA often carries negative net charge in the solution. When their sign of net charge is opposite to that on the surface, the Coulomb attraction force will lead to a decrease of ΔH of the system, which prompts the adsorption, and *vice versa* [108]. Second, if the hydrophobic regions of proteins contact with the hydrophobic surface, it will result in an increase of entropy of the water phase [109]. Since ΔS rises and thus ΔG drops, this hydrophobic interaction drives protein adsorption. On the contrary, hydrophilic surfaces promote the adsorption of a thin water layer on the substrate, which keeps the system of low interfacial energy. This water layer provides a repulsive barrier to hydrophobic moieties, known as hydration force, and therefore hinders protein adsorption [110]. Furthermore, another factor rises when surfaces are covered by hydrophilic polymers of certain chain length. Adsorption of biomolecules on such surfaces requires conformation change of polymers from a state of high degree of freedom of mobility to that of a reduced degree, which leads to a decrease in entropy and thus a raising of ΔG [111]. In reality, to control surface-biomolecule interactions, solid surfaces can be modified by different chemical functional groups, considering the aforementioned factors (as illustrated in Figure 2.4.).

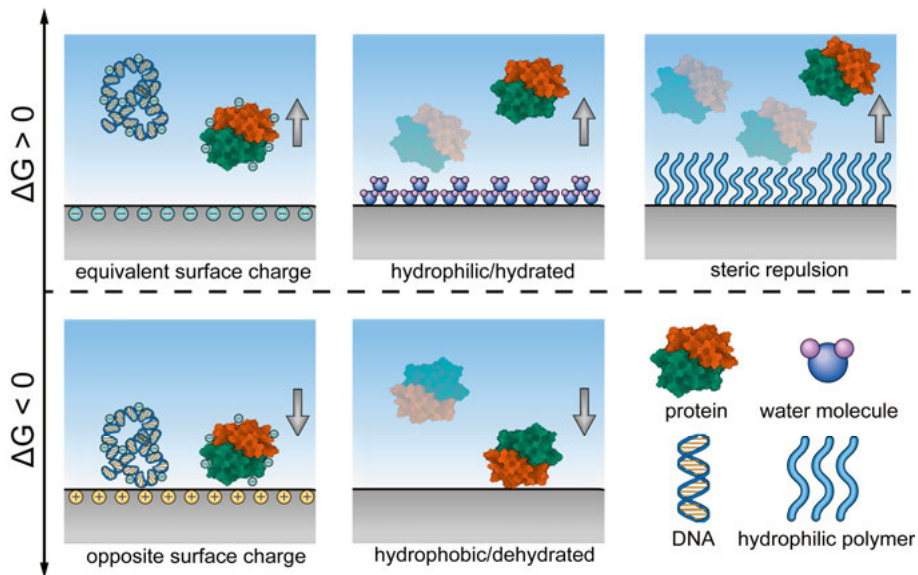


Figure 2.4. Surface-protein/DNA properties and their resulting Gibbs free energy, hindering or facilitating adsorption, respectively. For $\Delta G < 0$, protein adsorption is promoted, for $\Delta G > 0$, protein adsorption is hindered.

In this thesis, surface passivation by negatively charged polymers presented in Chapter 2 is effective to prevent DNA and protein adsorption through electrostatic repulsion and hydration forces. In addition, lipid bilayer coating

demonstrated in Chapter 3 is a well-known non-fouling surface, against non-specific adhesion via steric repulsion and also hydration forces.

3. Surface patterning on solid-state nanopore arrays

Aiming at minimizing nonspecific adsorption of biomolecules and localizing target binding sites in the vicinity of nanopores, one of the main efforts in this thesis has been put on developing a novel surface patterning strategy that is compatible with nanopore arrays. To date, to introduce specific binding sites near or inside the nanopore, most of the reported strategies have done that through stochastic distribution of the receptors on the organic coating covering the membrane. This approach is limited by the poor spatial controllability of the receptor between different coating batches and the high consumption of analytes bound to ligands outside of the sensing region. One feasible solution is to build a local chemical contrast in the nanopore region, which allows the ligand molecules selectively locate at the desirable positions. For nanopore arrays, this solution resembles well-established surface patterning techniques [112]. However, common surface patterning techniques are ill-suited to apply on solid-state nanopore arrays. Because, for already fabricated nanopores, the free-standing membrane is normally too fragile to experience further patterning process, while for integration patterning process along with nanopore fabrication, it may require complicated fabrication process and be practically difficult. Thus, our approach is to use a direct-write resist-less nanopatterning technique, electron beam induced deposition (EBID), to generate a chemical contrast near the prefabricated nanopores. In EBID, a substrate spot exposed to a focused electron beam can result in the localized deposition of materials from a dissociated vapor precursor [113]. By combining EBID with surface passivation of poly(vinylphosphonic acid) (PVPA), we can build carbon nanodomains aligned with nanopores, which serve as binding sites for target analytes. In addition, the PVPA passivation layer prevents nonspecific adsorption of biomolecules and also acts as the precursor for EBID process.

In this chapter, this versatile surface patterning technique is first demonstrated on planar Al surface (section 3.1) and shown the capability for immobilization of biomolecules (section 3.2), and then it is adapted on nanopore array structures (section 3.3) for localizing nanoparticles in the vicinity of nanopores (section 3.4).

3.1 Surface patterning of carbon nanoarrays

The idea of our surface patterning strategy is inspired by the demonstration of PVPA passivation against adsorption of biomolecules in single-molecule real-time (SMRT) sequencing [114], and surface biofunctionalization with EBID technique on a poly(ethylene glycol) (PEG)-coated glass substrate [115]. Since PVPA can selectively passivate Al or Al_2O_3 surface, which the latter could be easily deposited on nanopore surface by means of ALD, it motivates us to use this passivation for the later adaption on solid-state nanopores. With the EBID technique, carbon-containing nanostructures can be directly written on the surface, as PVPA layer serves as precursors. Thus, first, we demonstrate the PVPA passivation on planar Al surface to prevent non-specific adsorption and the capability of biofunctionalization of EBID fabricated carbon nanodomains. Then, for a further demonstration of this method, we place DNA polymerase with a streptavidin tag onto the carbon nanodomain with the assistance of an intermediate immobilization of biotinylated nanoparticles. We verify the well-defined localization and perseverance of enzyme activity by performing rolling circle amplification (RCA) and detecting the synthesized DNA products by fluorescence microscopy. The complete process flow from carbon nanoarray generation on passivated Al surface to immobilization of target biomolecules is schematically presented in Figure 3.1.

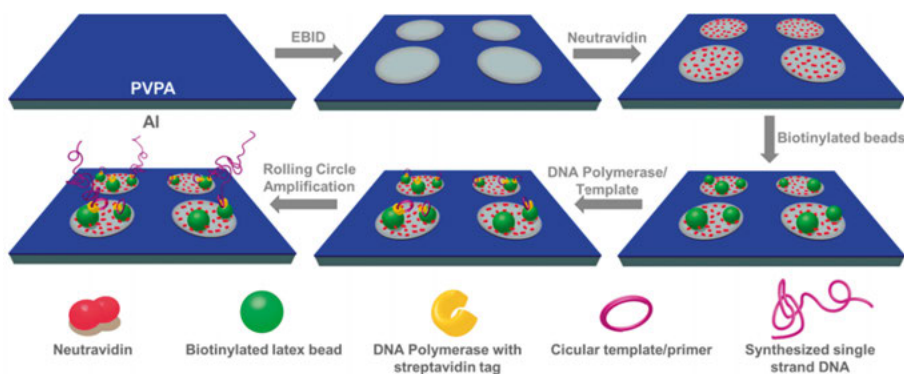


Figure 3.1. Schematic illustration of localization of target DNA polymerase and RCA on PVPA-passivated Al surface via EBID nanopatterning. Adapted with permission from Paper I. Copyright (2018) American Chemical Society.

3.1.1 Selective PVPA passivation against nonspecific adsorption

The molecular structure of PVPA is shown in Figure 3.2a, with each molecule containing about 200 phosphonic acid groups. A thermal deposition process was carried out to treat the patterned mixed material surface with aqueous PVPA solution. With a thin layer of native Al_2O_3 on the Al surface, the phosphonic acid groups can specifically react with the hydroxyl groups to form Al-

O-P bonds [116]. The selective deposition of PVPA on Al was confirmed using XPS (Figure 3.2b). The typical P 2p peak at 135 eV observed in PVPA-treated Al surface indicates the successful passivation of Al by PVPA [117].

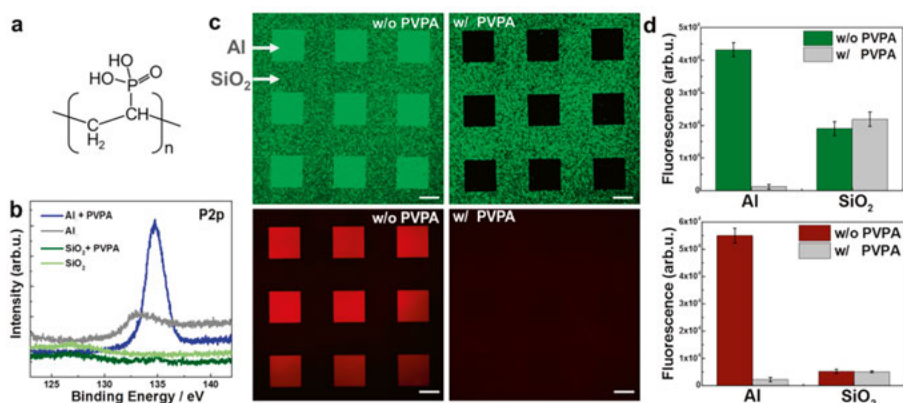


Figure 3.2. Selective passivation of Al against nonspecific adsorption of protein and DNA by PVPA modification. (a) Molecular structure of PVPA. (b) XPS spectra of P 2p on PVPA-treated and untreated Al surfaces. (c) Fluorescence micrographs of neutravidin (green) and oligonucleotide (red) adsorption on Al micropatterns on top of SiO₂, with (w/) and without (w/o) PVPA treatment. (Scale bars, 20 μm.) (d) Quantitative results of the fluorescence intensity on the two material surfaces with or without PVPA treatment. Adapted with permission from Paper I. Copyright (2018) American Chemical Society.

The PVPA-mediated anti-adsorption property was investigated by incubating the micropatterned surface with neutravidin and oligonucleotide as two test biomolecules. The presence of neutravidin was visualized with the assistance of biotinylated fluorescent nanoparticles and the oligonucleotide was directly labeled with Texas Red dye. As shown in Figure 3.2c, Without PVPA treatment, both neutravidin and oligonucleotide could adsorb to the Al surface with high density. On the PVPA-treated surfaces, the adsorption of neutravidin and oligonucleotide on Al surface was substantially suppressed and an excellent contrast of neutravidin adsorption over the surrounding SiO₂ surface was observed. Qualitative intensity analysis of the fluorescence micrographs verified that the PVPA-passivated Al surface was effectively repellent to neutravidin and oligonucleotide (Figure 3.2d).

3.1.2 Preparation and characterization of nanopatterns by EBID

To conduct EBID for generating carbon domains, a commercial EBL system was employed with the benefit of high reproducibility in defining designed patterns. Under electron beam irradiation, the volatile carbon residue in the

EBL chamber and the PVPA layer in the exposed area can be decomposed. As a result, the formation of carbon-containing nanodomains on the PVPA-passivated surface will mirror the geometrical arrangement of the e-beam exposure. Carbon square domain arrays were generated on the PVPA-passivated Al surface (Figure 3.3a).

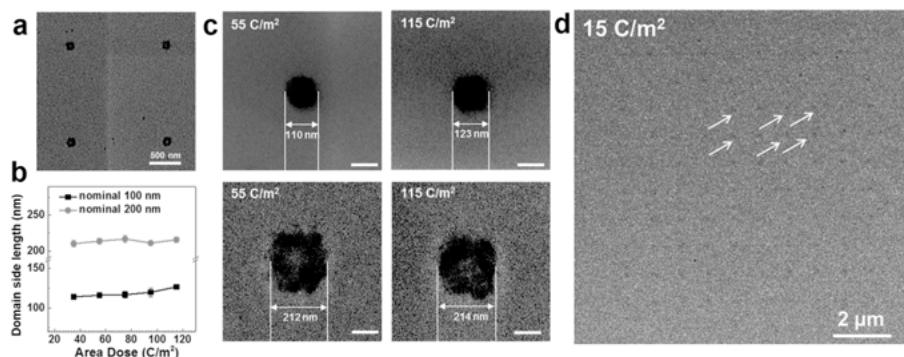


Figure 3.3. Morphological characterization of carbon nanodomains via EBID on PVPA passivated Al surface. (a) The SEM image of the nominal 100 nm nanodomain array with a lateral interval of 1.5 μm . (b) Influence of electron dose on the real size of the nanodomain. (c) SEM images of nanodomains fabricated with different doses and sizes. Scale bar: 100 nm. (d) SEM image of the 200 nm carbon nanoarray fabricated with an electron dose of 15 C/m^2 .

The main technical parameter that govern the EBID process is the electron dose in our fabrication process, which determines the dwell time of the electron beam. As shown in the statistical results (Figure 3.3b) and SEM images (Figure 3.3c), the electron dose only had a minor influence on the written feature size. The nanodomain profile was difficult to recognize below 20 C/m^2 electron dose under SEM, which implied that the amount of carbon material at such conditions was too low to produce distinguishable secondary electron contrast (Figure 3.3d).

3.2 Site-specific immobilization of various analytes

To assess the feasibility of selective biofunctionalization of the EBID fabricated carbon nanoarrays, we first use fluorescent labelled streptavidin and oligonucleotide to demonstrate. Then, immobilization of biotinylated fluorescent nanoparticles is further demonstrated, which provides a versatile approach for immobilization strategies. And finally, considering the importance of DNA polymerase in the application for DNA sequencing, we show the capability of positioning DNA polymerase with streptavidin tag on the carbon domains with retained activity of synthesizing DNA via RCA.

3.2.1 Streptavidin and oligonucleotides

First, streptavidin and oligonucleotides were tested as examples for biomolecules. As shown Figure 3.3a, Cy3-streptavidin can be selectively physisorbed to the carbon nanoarrays with a significantly higher contrast over the non-patterned passivating PVPA regions. For oligonucleotides, direct adsorption and indirect bio-affinity approaches were both examined by incubating biotinylated Texas Red labeled oligonucleotides with plain carbon nanoarrays and neutravidin-decorated nanoarrays. As a result, the labeled DNA molecules were unable to directly adsorb on the plain nanoarrays (Figure 3.3a, right). Via biotin-avidin interaction, a distinct localization of the biotinylated DNA was observed on neutravidin-decorated nanoarrays (Figure 3.3a, middle). The statistical results confirm that outstanding localization selectivity was achieved for direct adsorption of streptavidin and neutravidin mediated binding of biotinylated DNA, on the 100 nm and 200 nm nanoarrays (Figure 3.3b). The mechanism underlying the excellent selective localization of streptavidin is due to the strong nonspecific adsorption on carbon nanodomains and the anti-adsorption property of the PVPA layer, further discussion can be found in Paper I.

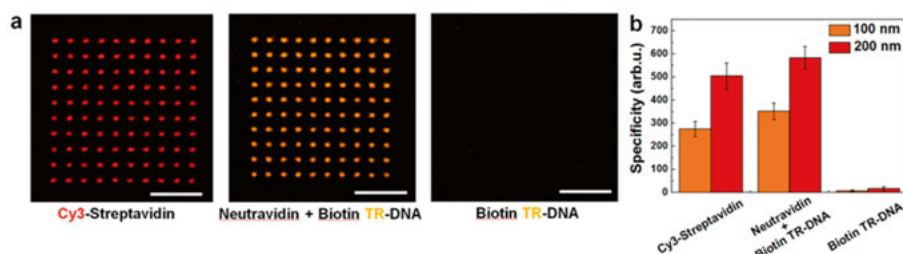


Figure 3.3. Biofunctionalization of carbon nanoarrays with streptavidin and oligonucleotide. (a) Fluorescence images of 100 nm carbon nanoarrays immobilized with fluorescently-labeled protein and DNA: Cy3-streptavidin-decorated nanoarrays (left); neutravidin-decorated nanoarrays immobilized with biotinylated Texas Red labeled oligonucleotide (middle); carbon nanoarrays directly incubated with biotinylated Texas Red labeled oligonucleotide (right). (Scale bar: 5 μ m) (b) Statistical results of the immobilization specificity of biomolecules on different size nanoarrays. Adapted with permission from Paper I. Copyright (2018) American Chemical Society.

3.2.2 Biotinylated nanoparticles

To exploit the latent capacity of the presented nanopatterning approach, fluorescent biotinylated nanoparticles of 40 nm in diameter were tested to incubate with neutravidin-decorated nanoarrays fabricated with various electron doses. As shown in Figure 3.4a and b, the biotinylated particles were selectively localized on the nanodomains and the particle occupation rate was influenced

by the electron dose. The statistical results (Figure 3.4c) show that the occupancy of biotin particles increased with the increase of electron dose. With a similar target area, a higher density of binding sites led a higher probability of nanoparticle immobilization. The dependence of the occupancy of biotinylated particles on electron dose is due to the difference of local neutravidin density, which could be adjusted by the electron dose of the EBID process [115].

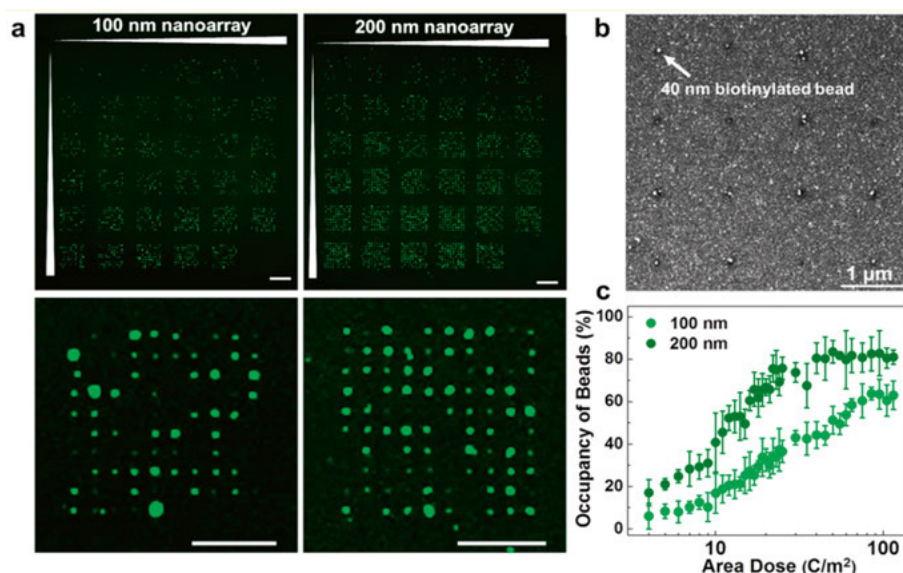


Figure 3.4. Positioning of biotinylated nanoparticles onto neutravidin-decorated nanoarrays. (a) Fluorescence images of localization of 40 nm biotinylated nanoparticles on different size neutravidin-decorated nanoarrays with various doses (upper) and magnified portion of the arrays (lower) at an electron dose of 115 C/m². (Scale bar: 5 μm) (b) SEM image of particle loaded nanoarrays with observed localization of single and double particles. (c) Statistics of particle occupancy rate with the electron dose. Reproduced with permission from Paper I. Copyright (2018) American Chemical Society.

The diffusion-based immobilization of nanoparticles should follow the Poisson-distribution throughout the nanoarrays [114]. To estimate the number of particles on differently sized nanoarrays, the fluorescence intensity distribution was analyzed from the images of particle loaded nanoarrays by employing the Poisson statistics to calculate the percentage of each number group, as shown in Figure 3.5. By setting an optimal fluorescence threshold, the nanodomains occupied with particles were selected as the target region to give the histogram analysis of mean fluorescence brightness. For the 100 nm nanoarrays, a narrow peak of around the 500 (arbitrary unit) fluorescence level was observed, which could be ascribed to the single particle occupied

nanodomains. Hence, the Poisson statistics was employed to establish the relationship between fluorescence intensity and occupancy number. As shown in Figure 3.5, the calculated occupancy rate follows the profile of fluorescence intensity distribution for both size nanoarrays, indicating the expected Poisson-distributed particle loading.

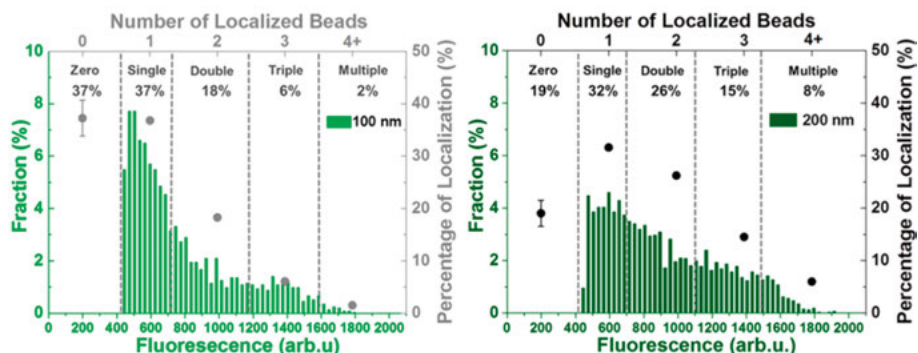


Figure 3.5. Histogram analysis of fluorescence intensity on biotinylated particle localized nanoarrays of different sizes and different rates of particle occupancy calculated with the Poisson statistics, except that the zero-particle occupancy rate is obtained from experimental results. Reproduced with permission from Paper I. Copyright (2018) American Chemical Society.

3.2.3 DNA polymerase

As an essential enzyme to synthesize DNA, DNA polymerase has been extensively employed for DNA cloning, sequencing, labeling and other applications [4, 118]. To further demonstrate the compatibility and extensibility of the presented patterning approach, DNA polymerase with a streptavidin tag was positioned on the biotinylated particle loaded nanoarrays and in situ RCA was subsequently performed to detect the activity and localization of the immobilized polymerase. Before loading onto the biotinylated nanoarrays, the streptavidin tagged DNA polymerase was first bound to a circular DNA template/primer. After multiple washing steps to eliminate nonspecifically adsorbed polymerase/template complex, subsequent in situ RCA on the patterned surface was carried out to synthesize ssDNA containing repetitive sequences complementary to the circular template. Using complementary Texas Red-labeled oligonucleotides as a probe, the amplified DNA strands were detected by fluorescence microscopy (shown in Figure 3.6a). For the nanoarrays of both sizes, an obviously organized localization of fluorescent biotinylated particles and synthesized DNA were observed. This result indicates the successful immobilization of the DNA polymerase and the preservation of the enzyme activity. The strong colocalization of two fluorescent signals of superimposed false-color images indicates that the active DNA polymerase was localized to the nanoarray via the specific avidin-biotin binding.

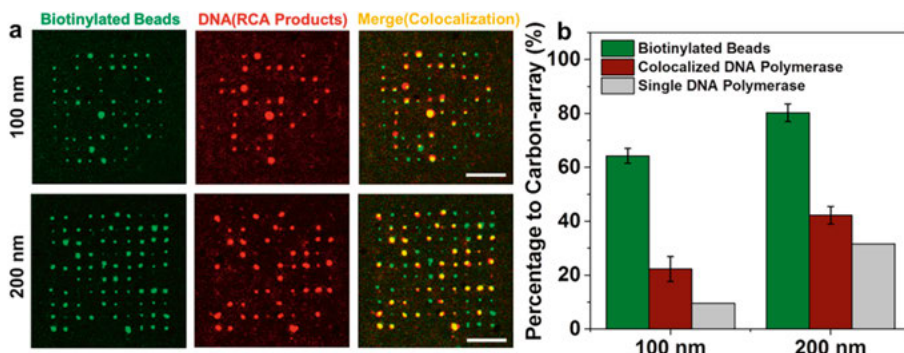


Figure 3.6. Colocalization of biotinylated particles and single-stranded DNA synthesized by immobilized DNA polymerase. (a) Fluorescence micrographs of immobilized biotinylated fluorescent particles (green), DNA strand synthesized by RCA (red) and the merged images to show the colocalization. (Scale bar: 5 μ m) (b) Statistical results of loading percentage of biotinylated particles, colocalized DNA polymerase and single DNA polymerase on two different nanoarrays. Adapted with permission from Paper I. Copyright (2018) American Chemical Society.

The level of colocalization was quantitatively analyzed by a further statistical analysis of the biotinylated particles and localization of RCA product (Figure 3.6b). Similar to the previous assumption, the loading rate of single polymerase can also be estimated by using the Poisson statistics once the missing fraction of colocalization is known. Localization of approximately 10% and 30% single polymerase was achieved, respectively, for the 100 nm and 200 nm nanoarrays. In conclusion, the combination of PVPA passivation with EBID nanopatterning allowed us to specifically position the target enzyme onto organized nanoscale domains with retained activity.

3.3 Deposition of carbon nanoarray on nanopore array

Functional nanoparticles are at the forefront of numerous sensing applications in large part due to their ease of functionalization with receptor ligands and incorporation with optical sensing methods [119-121]. For nanopore sensors, use of nanoscale particles of unique optical, magnetic, electronic or chemical properties can enable applications otherwise unconceivable [122-124]. To explore the potential of the developed patterning technique, we transfer this adaptable method to nanopore arrays for nanoparticle localization, as presented in Paper II. In the following sub-sections, we demonstrate the capability of precise localization of streptavidin coated nanoparticles in the close vicinity of the nanopores defined by the pore-specific carbon domains. Furthermore, we study the nanoparticle loading efficiency by comparing diffusion-

driven loading with electrophoresis-driven loading, as schematically shown in Figure 3.7.

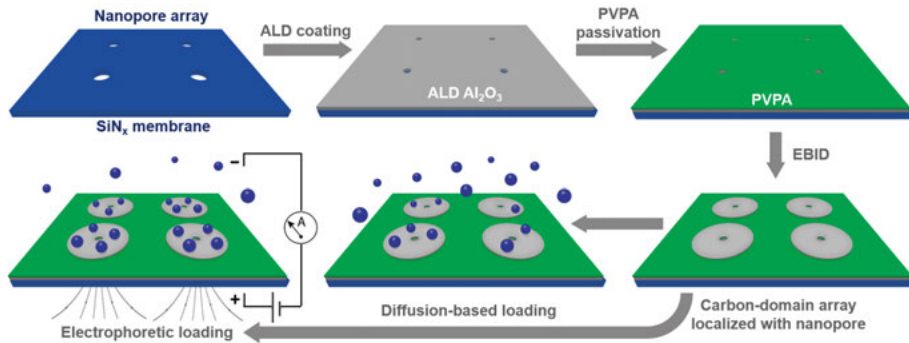


Figure 3.7. Schematic of EBID assisted precise localization of nanoparticles on solid-state nanopore arrays by diffusion- or electrophoresis-driven loading. Reproduced from Paper II. Copyright (2019) IEEE.

3.3.1 Fabrication of SiN_x nanopore arrays

To manufacture nanopore arrays, we employ nanopore fabrication method based on electron beam lithography (EBL) and RIE. The process steps of SiN_x nanopore array fabrication are schematically illustrated in Figure 3.8. The fabrication started from a 300 μm double side polished silicon wafer. After standard wafer cleaning, the wafer was thermally oxidized to grow a 50-nm thick SiO₂ layer. This is followed by the growth of a 25-nm thick low stress SiN_x by the means of low-pressure chemical vapor deposition (LPCVD). Subsequently, etched alignment marks were first fabricated to ensure an accurate realignment of carbon nanodomains to the nanopores. Nanopore arrays were patterned on the front side with EBL and then transferred into the device layer SiN_x by means of RIE. Next, a 150 μm window was opened from the rear side of the wafer by photolithography. Deep reactive ion etching (DRIE) and KOH etching were subsequently carried out to open large cavities in the thick Si carrier layer reaching the SiO₂ on the front side. This oxide was then stripped off in buffered hydrofluoric acid (BHF), completing the generation of nanopore arrays in the free-standing SiN_x membrane on the front side of the wafer.

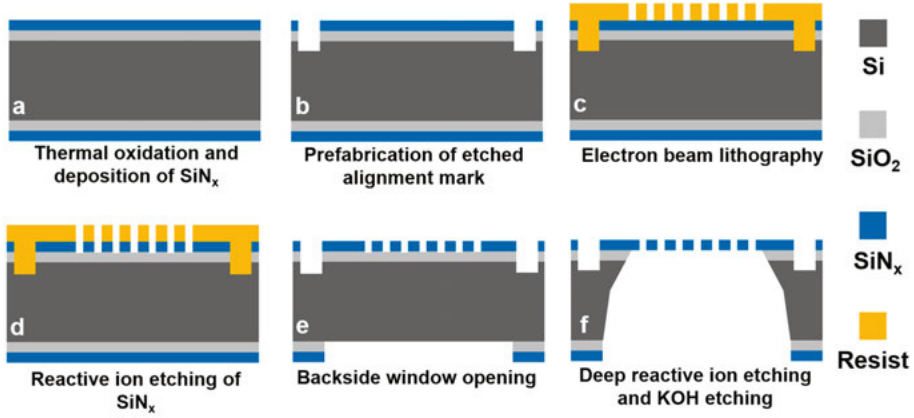


Figure 3.8: Process for fabrication of a nanopore array in SiN_x membrane: (a) Thermal oxidation followed by SiN_x deposition by means of LPCVD; (b) Definition of etched alignment marks; (c) EBL patterning of the nanopore array; (d) RIE of SiN_x ; (e) Rear side window opening; (f) DRIE and KOH etching and final oxide removal from the rear side. Reproduced from Paper II. Copyright (2019) IEEE.

3.3.2 Deposition of carbon domain in the vicinity of nanopore

To deposit carbon domains in the vicinity of nanopores, the nanopore array was first coated with a 10 nm thick Al_2O_3 by means of ALD and passivated with PVPA subsequently. For the following EBID process, it is worth mentioning that the carbon domains were written on the designated surface area in virtue of the alignment with prefabricated etched marks in the EBL system. Since nanopores were fabricated by using the same alignment mark, carbon domains can be generated with an accurate spatial organization with respect to nanopores. This capacity of precise alignment cannot be easily achieved using other nanopatterning techniques such as nanoimprint lithography and nanocontact printing.

In Figure 3.9a, the SEM image shows a SiN_x nanopore array with pores of 80 nm in diameter. Upon a 10 nm thick Al_2O_3 coating, the pore size shrank to approximate 60 nm in diameter (Figure 3.8b). Since the carbonized area is difficult to be recognized in SEM, the patterned nanopores were incubated with streptavidin coated nanoparticles to verify the existence of carbon domains. As shown in Figure 3.9b, nanoparticles are selectively localized in the vicinity of the nanopores through the adsorption on the carbon surface. In a particular case (Figure 3.9c), a large amount of carbon is deposited in the inner orifice of the nanopore. This result demonstrates the compatibility of the developed surface patterning strategy with fabricated nanopore array structures.

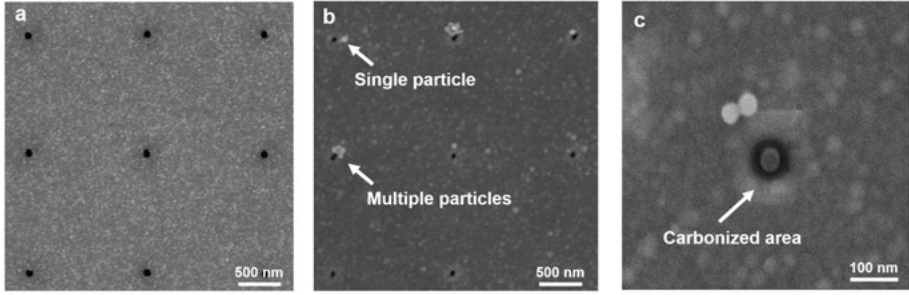


Figure 3.9: (a) SEM image of a nanopore array with nanopores of 80 nm in diameter; (b) SEM image of nanoparticles localized in the vicinity of the nanopores; (c) SEM image of the carbonized area around a nanopore with nanoparticles immobilized nearby.

3.4 Localization of nanoparticles on nanopore array

With the natural feature of nanopores allowing for electrophoresis of charged nanoparticles, they can be loaded onto carbon domains either by simple diffusion or by electrophoretic forces. We compare the two approaches in the following sub-sections.

3.4.1 Diffusion-based approach

In diffusive-loading, we incubated the patterned nanopore surface with streptavidin particles of various concentrations for 30 minutes. As shown in Figure 3.10a, the loading yield drastically decreases with decreasing nanoparticle concentration. In Figure 3.10b, the statistical result verifies that the loading fraction drops from 65% to 3% when the particle concentration is decreased three orders of magnitude. This result reflects that the diffusive loading efficiency is highly dependent on the particle concentration based on the diffusion kinetics, which could be a major hurdle for applications where only low nanoparticle concentrations are available.

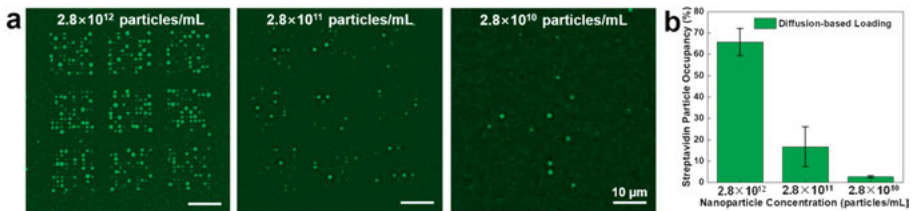


Figure 3.10: (a) Fluorescence micrographs of nanoparticles immobilized by diffusion at different concentrations; (b) Variation of particle occupancy with particle concentration. Reproduced from Paper II. Copyright (2019) IEEE.

3.4.2 Electrophoresis-based approach

To enhance the nanoparticle capture efficiency by the carbon nanodomains, electrophoretic force was utilized to drive the charged nanoparticles onto the carbon nanoarrays around the nanopores. The nanoparticles coated with streptavidin are negatively charged, and can be electrophoretically driven to the pore orifice. With a concentration of 2.8×10^9 particles/mL and at an applied voltage of 200 mV for 5 minutes, a nanoparticle occupancy over 90% on the nanopore array is observed in Figure 3.11a. To achieve similar localization occupancies, the required nanoparticle concentration is three orders of magnitude higher for the diffusion-driven loading than for the electrophoresis-driven one. The SEM images in Figure 3.11b confirm the nanoparticle localization on the carbon nanodomains. Furthermore, the ionic current change along the loading process can be monitored. For a smaller array of 5-by-5 pores, the ionic current change for individual pores can be recognized, as evident from the stepwise blockage of the ionic current trace (Figure 3.11c). Since the average diameter of nanoparticles of 40 nm is smaller than the pore diameter of 60 nm, translocation events can occur as indicated by the spikes in the current trace. While the pore surface is highly carbonized, continuous current drop is observed as a result of pore clogging by the nanoparticles.

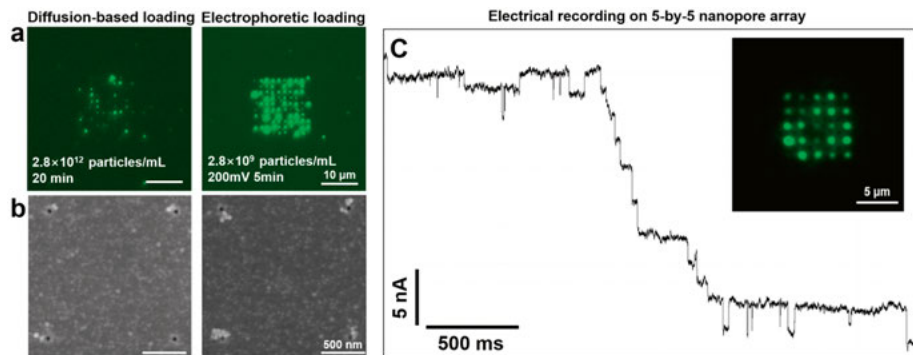


Figure 3.11: (a) Fluorescence images of nanoparticles immobilized on nanopores by diffusion (left) versus electrophoresis (right); (b) SEM images of nanoparticles immobilized in the vicinity of the nanopores by diffusion (left) versus electrophoresis (right). (c) Ionic current trace during the electrophoretic loading of fluorescent nanoparticles on a 5-by-5 nanopore array. Inset shows the fluorescence image of the eventual nanopore array localized with nanoparticles. (a) and (b) are adapted from Paper II. Copyright (2019) IEEE.

4. Lipid bilayer coated on truncated-pyramidal Si nanopore arrays

In the previous chapter, the concept of using EBID fabricated hydrophobic carbon domains to capture various nanoscale entities is demonstrated for potential nanopore sensing applications. While for conventional nanopore sensing modalities, a hydrophilic pore surface is often desirable to allow for an unperturbed translocation. To provide functionalities of both anti-adsorption and active binding sites on pore surface, coating with lipid bilayer has proven to be a powerful strategy. Pioneered by Mayer's research group, this strategy has been used to identify geometric profiles and dipole moments of proteins with nanopores [45, 46]. However, with the emergence of various types of solid-state nanopores, the feasibility of lipid bilayer coating on various pore geometries and materials need to be verified. Hence, we adapt this coating method on truncated pyramidal Si nanopore (TPP) arrays and study the corresponding mechanism of lipid bilayer formation via electrical monitoring and optical observations. Furthermore, to validate the efficacy of the coated lipid bilayer against DNA adsorption, we developed an optical characterization platform to study the DNA translocation events with the advantage of parallel detection using pore arrays.

In this chapter, the fabrication of TPP arrays is first described in section 4.1. Then, the mechanism of lipid bilayer formation on TPP arrays is discussed in section 4.2. At last, the optical observation of DNA translocation through lipid coated pores is presented in section 4.3.

4.1 Fabrication of truncated-pyramidal nanopore arrays

One of the motivations for us to develop fabrication process of Si-based TPP pores, instead of SiN_x pores, is to take advantage of the anisotropic etching of crystalline Si to define smaller pore size beyond the limitation of lithography. An additional reason is that Si shows negligible photoluminescence (PL), which constitutes an ideal substrate for optical detection and will be discussed later in 4.3.1. Details of the TPP fabrication are schematically shown in Figure 4.1. The process started on a 4-inch double side polished silicon on insulator (SOI) wafer with a 55 nm thick Si device layer on 145 nm thick buried oxide (BOX) layer. A 30 nm low stress SiN_x was deposited on both sides of the

wafer via LPCVD. This was followed by nanopore arrays patterned on the deposited SiN_x using EBL and RIE. The substrate was opened with large cavities by DRIE and KOH etching to stop on the BOX with the Si device layer protected. In the next step, patterned nanopores in SiN_x were transferred to the Si device layer with a second KOH etching. After removal of BOX, TPPs in a free-standing Si membrane were formed. Finally, thoroughly cleaned TPP chip were incubated in solutions with small unilamellar vesicles (SUVs) composed of 1-palmitoyl-2-oleoyl-glycero-3-phosphocholine (POPC) to coat the lipid bilayer.

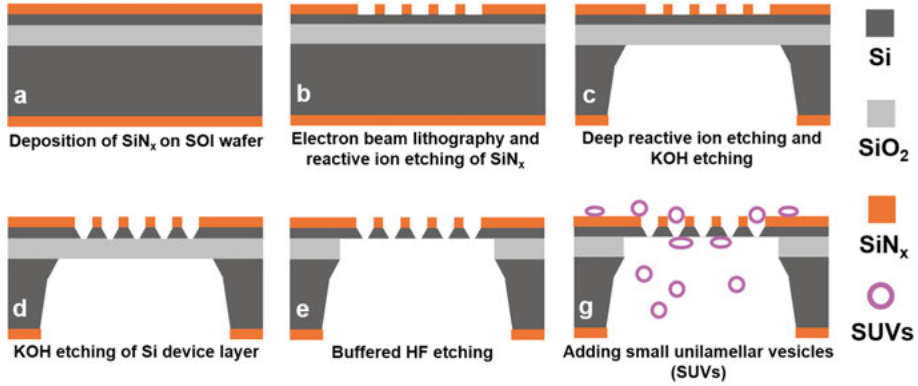


Figure 4.1. Process flow for fabrication of a Si TPP nanopore array and formation of lipid bilayer coating using small unilamellar vesicles (SUVs). Reproduced from Paper IV. Copyright (2020) IEEE.

In Figure 4.2a, SEM images show a 5-by-5 TPP array with a pore spacing of $1\ \mu\text{m}$, where inset (i) depicts a higher magnification image of one of the pores. The truncated pyramidal shape of the TPPs can be clearly seen in inset (ii). Unless otherwise specified, the TPP array used in this work is 5-by-5 with the same TPP size (length of the bottom square base) around $60\ \text{nm}$.

4.2 Formation of lipid bilayer on TPP arrays

Lipid bilayer formation on the TPP arrays was first monitored in real-time by the ionic current change through the TPP arrays. The mechanism of the lipid bilayer formation was investigated by a statistical analysis of the current drops caused by the adsorption and rupture of vesicles. Then, the optical observation verified the proposed mechanism via visualization of the formation process using fluorescent labelled SUVs. The detailed experimental description can be found in Paper III.

4.2.1 Electrical monitoring of lipid bilayer formation

For electrical monitoring, after adding the vesicle solution to the two reservoirs sandwiching the TPP chip, a bias was applied via the Ag/AgCl electrodes connected with a flow cell. The electrolyte on the larger TPP base side was set at the given potential values while the opposite electrolyte on the small base side was kept at ground. A typical example of monitored ionic current trace by adding vesicles with a hydrodynamic radius (R_H) of 92 nm at 50 mV is presented in Figure 4.2b. As can be clearly seen, the ionic current through the nanopores started to decrease step by step when the voltage was applied. Initially, the decrease in the ionic current was rapid and then became slower and finally tended to level off. The inset in Figure 4.2b shows a close-up view of the current trace between 9 s and 16 s. The current drops were all found to be discrete steps instead of a continuous decay, indicating that the process giving rise to the current drops is instantaneous.

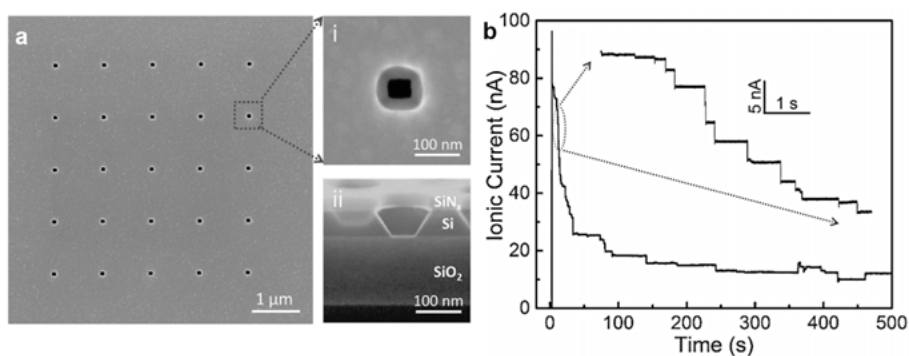


Figure 4.2. SEM images of a TPP nanopore array and the measured ionic current through the TPP array at 50 mV after adding vesicles ($R_H = 92$ nm). (a) SEM image of a 5×5 TPP nanopore array with the pore spacing of 1 μ m. Inset (i) shows a close-up image of the marked pore position. Inset (ii) shows a cross sectional SEM image of TPP without a large cavity underneath and with the BOX layer intact for easy sample preparation. (b) Vesicles ($R_H = 92$ nm) dispersed in PBS were added to the two reservoirs sandwiching the TPP chip. After connecting with the two Ag/AgCl electrodes, 50 mV was applied and the ionic current started to decrease step by step. The inset shows a close-up view of the steps of current drop between 9 and 16 s. Adapted with permission from Paper III. Copyright (2020) American Chemical Society.

Three different scenarios that can cause the current drop are envisioned: lipid bilayer formation inside the TPPs that covers the inner TPP side walls; formation of a lipid bilayer that spans the TPPs; and adsorption of an intact vesicle in the TPP. Whereas the former leads to a reduction in pore diameter and thus the ionic current, the two latter scenarios would lead to blockage of the TPP. Assuming that the lipid bilayer is formed inside the TPP completely and

uniformly, the ionic current per pore is calculated to drop by 0.27 nA at 20 mV, 0.71 nA at 50 mV and 1.30 nA at 100 mV. Taking this as unity at respective bias, the number of size reduced pores (N_{SRP}) can be calculated as dividing current drops by unity. N_{SRP} is used to characterize to what extent the interior of TPPs are covered by the lipid bilayer and non-integers can appear. If a TPP is blocked, the resulting N_{SRP} should be much more than 1. To further determine the dominant cause of the current drops, careful statistical analysis of the current steps was performed for the measurements with different applied biases, vesicle sizes and concentrations. As illustrated in Figure 4.4a, at different conditions, current drop events appear intensely within the first 50 s after the bias was applied. In addition, N_{SRP} exhibited a similar distribution, although the frequency was slightly different for different conditions (Figure 4.4b). Nevertheless, for all conditions, N_{SRP} all appeared most frequently at around 0.5, indicating that lipid bilayer formed from the vesicle rupture only partially covered the interior of a TPP.

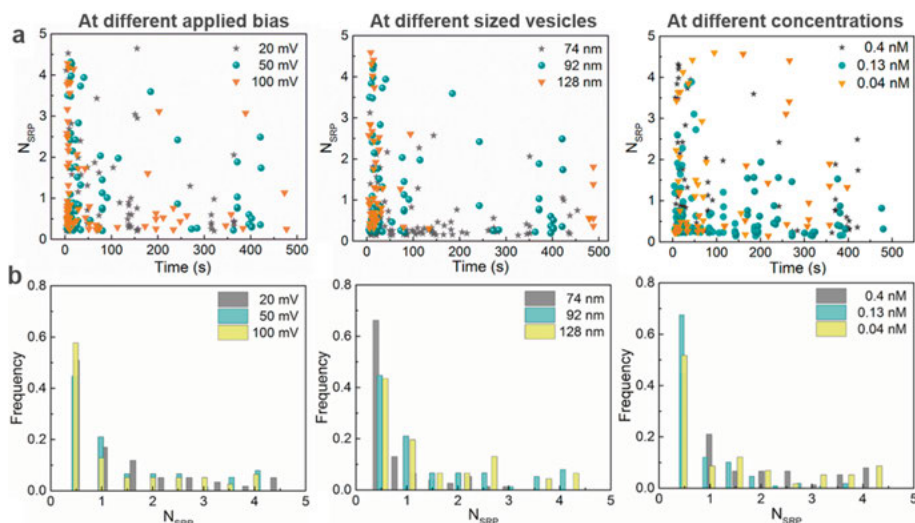


Figure 4.3. Statistical analysis of current steps of the recorded ionic current trace of 5-by-5 nanopore arrays at various conditions. (a) N_{SRP} versus time at different applied bias, sized vesicles and concentrations. (b) Relative frequency of N_{SRP} at different applied biases, vesicles of different sizes and concentrations. Reproduced with permission from Paper III. Copyright (2020) American Chemical Society.

From the findings described above, the process of lipid bilayer formation in the TPP arrays can be inferred as follows: vesicles diffuse to the TPPs, adsorb in the opening of the TPPs and rupture instantaneously to form the bilayer. In the presence of TPPs, the truncated pyramidal shape of a TPP creates a larger vesicle-solid contact area than that of vesicle on a planar support (Figure 4.4a and b). Increased contact area further deforms the vesicle, which leads to an

even higher surface tension. When the surface tension reaches a critical value, vesicles rupture to lipid bilayer. This could be a plausible explanation of the instant rupture of the vesicles in the TPPs. This process is thus different from vesicle rupture on a planar support, which is a typical cooperative process that the rupture only happens when a critical surface coverage of adsorbed vesicles is reached [125, 126]. In addition, the edges of the lipid bilayer formed in the TPPs are energetically unfavorable [127, 128] and can catalyze the rupture of vesicles adsorbed in its immediate vicinity [129], which will result in the formation of a lipid patch. More detailed discussion can be referred in Paper III.

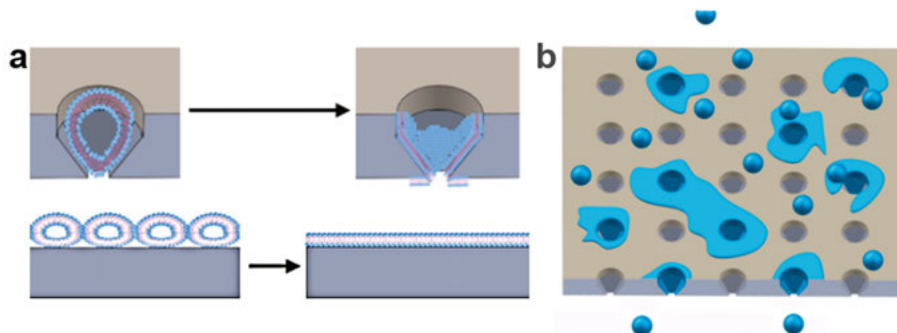


Figure 4.4. Schematic representation of the lipid bilayer formation over nanopore arrays. (a) Upper part: vesicles rupture spontaneously upon adsorption in the TPP cavity. Lower part: lipid bilayer formed at high vesicular coverage on a planar support. (b) Schematic representation of the lipid bilayer formation over TPP array. Reproduced with permission from Paper III. Copyright (2020) American Chemical Society.

4.2.2 Optical observation of lipid bilayer formation

The proposed process is confirmed by imaging the adsorption of vesicles with 1 mol% lipids labeled with Rhodamine-PE. As can be seen in Figure 4.5a, after adding vesicles for a short time (around 1 min for adding vesicles, setting up the microscope, finding the free-standing membrane and starting to record), the lipid bilayer is preferentially formed across the TPP area and the rest of the surface is still covered with intact vesicles or small non-continuous lipid patches. The lipid patch then started to grow from the TPP area as time elapsed. Figure 4.5b shows a close-up view of TPP area after rinsing the chip for 10 min by stopping the lipid bilayer formation in Figure 4.5a at around 2 minutes. It is worth noting that no bias voltage was applied during the optical inspection. These findings indicate that the lipid bilayer formation can be accelerated by predesigned nanocavities on a planar surface. The formation of a complete lipid bilayer on the whole substrate is clearly visible (Figure 4.5c) after over 30 min exposure of the substrate to the solution of vesicles.

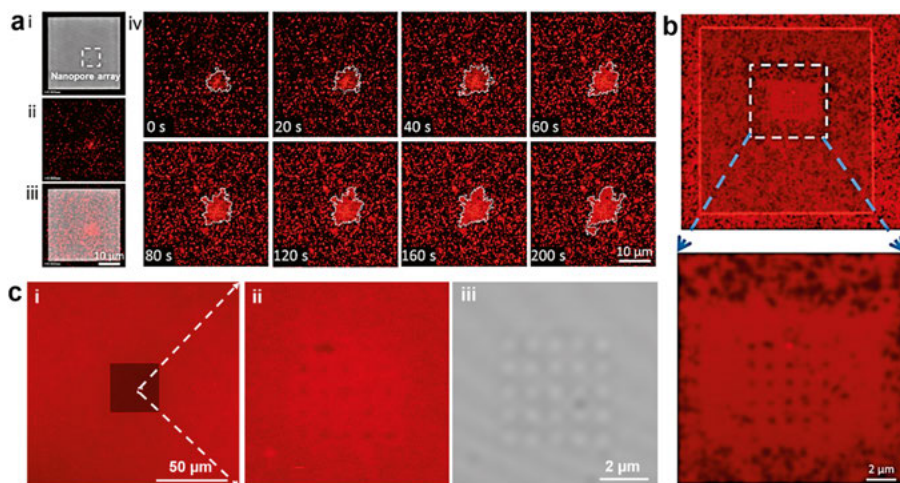


Figure 4.5. Fluorescence micrographs of lipid bilayers formed on TPP chip. (a) Induced vesicle rupture in the nanopore array structure: (i) Bright field (BF) image of a 5-by-5 TPP array; (ii) Fluorescence micrograph of Rhodamine labelled liposome adsorbed and ruptured on TPP area; (iii) Overlay image of (i) and (ii); (iv) A set of fluorescence micrographs in a time series under zero voltage bias, the white dashed contour lines mark the formed lipid bilayer near the TPP area. (b) Lipid bilayer is preferentially formed over the TPP area instead of the planar surface. The inset shows a close-up view of the TPP area. (c): (i) Lipid bilayer is completely formed over whole surface of the TPP chip. (ii) A close-up view of the TPP area. (iii) BF image of the TPP area. Reproduced with permission from Paper III. Copyright (2020) American Chemical Society.

4.2.3 Fluorescence recovery after photobleaching

To confirm the fluidity of the supported lipid bilayer, experiments of fluorescence recovery after photobleaching (FRAP) were performed on the lipid bilayer at a location outside, but near the TPP area. A set of consecutive fluorescence images of the FRAP measurement is shown in Figure 4.6a. By analyzing these images and normalizing the fluorescence intensity to the maximum intensity before photobleaching, the lateral diffusion coefficient of the POPC can be determined by the following equation:

$$D_L = 0.224 \times \frac{r^2}{t_{1/2}} \quad (4.1)$$

where r is the radius of the bleached spot and $t_{1/2}$ is the half time of the fluorescence recovery [130, 131]. The obtained values of $t_{1/2}$ and D_L from an exponential curve fit of the data are 22.9 s and $0.550 \mu\text{m}^2\text{s}^{-1}$, respectively. The obtained value is close to the reported value ($0.71 \mu\text{m}^2\text{s}^{-1}$) of POPC on a Si_3N_4 surface [132].

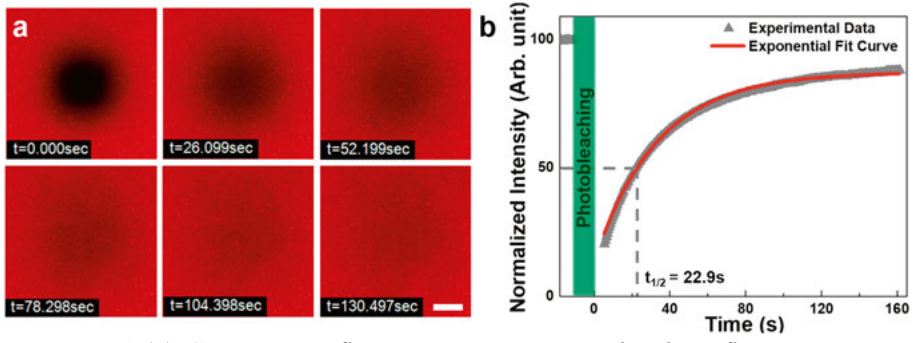


Figure 4.6:(a) Consecutive fluorescence micrographs show fluorescence recovery after photobleaching experiment. The scale bar is $5\mu\text{m}$. (b) Plot of the normalized intensity versus time from FRAP experiments performed on a TPP chip. Grey points correspond to experimental data. Red line corresponds to fitted curve using the diffusion model.

4.3 Optical detection of DNA translocation on TPPs

With the successful demonstration of lipid bilayer coating on TPP arrays, it motivates us to employ this tailored device for optical sensing of DNA translocation and to validate its promised function of minimizing biomolecule-pore interaction, which is concluded in Paper IV.

4.3.1 Photoluminescence of SiN_x

For fluorescence-based optical sensing, photoluminescence (PL) of the membrane is detrimental because it degrades the signal to noise ratio (SNR) and impedes the recognition of single DNA translocation, particularly for short-length DNA with relatively weak fluorescence. Even though SiN_x nanopores are widely used to perform electrical sensing of DNA molecules, a SiN_x layer produces significant PL under illumination in the blue-green spectrum range, thereby limits its applicability in optical sensing [17, 133]. In our device, a SiN_x layer serves as a hardmask for the anisotropic Si etching. To evaluate the PL emission of the as-fabricated SiN_x/Si membrane and to compare it to SiN_x and Si membrane, the PL spectrum of the following three different membranes was recorded under excitation at 532 nm: a 30 nm thick SiN_x membrane, a 55 nm Si membrane, and a double layer membrane of the 30 nm thick SiN_x layer on the 55 nm thick Si layer. As shown in Figure 4.7a, both membranes with the SiN_x layer present have a relatively intense and broad PL from 550 nm to 900 nm, while the Si membrane reveals negligible PL in this range. One of the reasons for the reduction of PL intensity of the double layer membrane in comparison with the bare SiN_x membrane can be a result of optical interference. A similar trend can be seen from the more quantitative measurements

by using confocal microscopy in Figure 4.7b. Under laser illumination at both 488 nm and 532 nm, the Si membrane shows negligible PL. Specifically, the PL intensity of the Si membrane shows at least a 20-fold decrease as compared with those of the other two membranes. Hence, the removal of the SiN_x mask layer in the fabrication process is a prerequisite to render a PL-free membrane. By a further fabrication step of RIE to remove SiN_x , only TPP arrays on pure Si membrane were used for the following optical observation experiments.

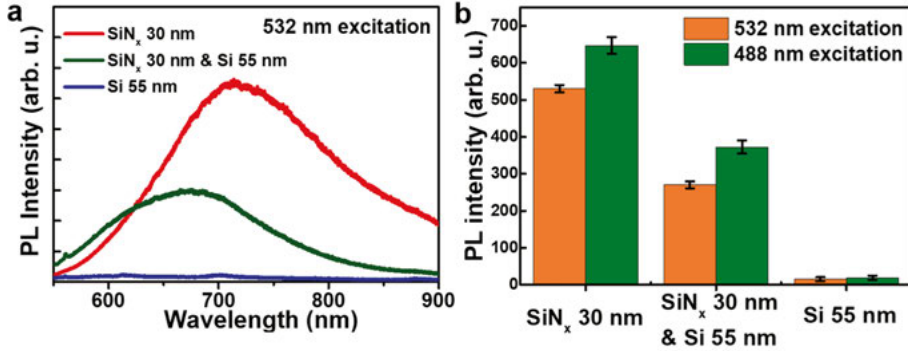


Figure 4.7. PL measurement of a 30 nm thick SiN_x membrane, a 55 nm thick Si membrane, and a double layer membrane of the 30 nm thick SiN_x on the 55 nm thick Si: (a) PL spectra under 532 nm laser excitation; (b) Confocal measurement data of PL emitted from the same size area of the different membranes under 488 and 532 nm laser excitations. The detection wavelength range is 550–800 nm, and the data are normalized to the excitation laser intensities. Reproduced from Paper IV. Copyright (2020) IEEE.

4.3.2 Fluidic cell and optical setup

For optical observation, a custom polyether ether ketone (PEEK) fluidic cell chamber was made, which allowed the mounted nanopore chips to be illuminated and fluorescence signals in the nanopore region to be collected, as shown in Figure 4.8. A pair of pseudo reference Ag/AgCl electrodes were mounted in the electrolyte filled chambers to apply the external bias voltage. Instead of clamping the nanopore chip by pressing O-rings on both sides, the chip was sealed to the upper chamber component by adhesion using a double-sided tape and a polydimethylsiloxane (PDMS) gasket. The bottom of the cell chamber was sealed using a 0.17 mm thick cover glass thereby allowing for a short working distance in optical observation. The optical observation was conducted using a confocal laser scanning microscope with a hybrid GaAsP detector. For all measurements, the fluorescence data were acquired using a 63 \times glycerol objective (NA= 1.3) under a 532 nm laser excitation.

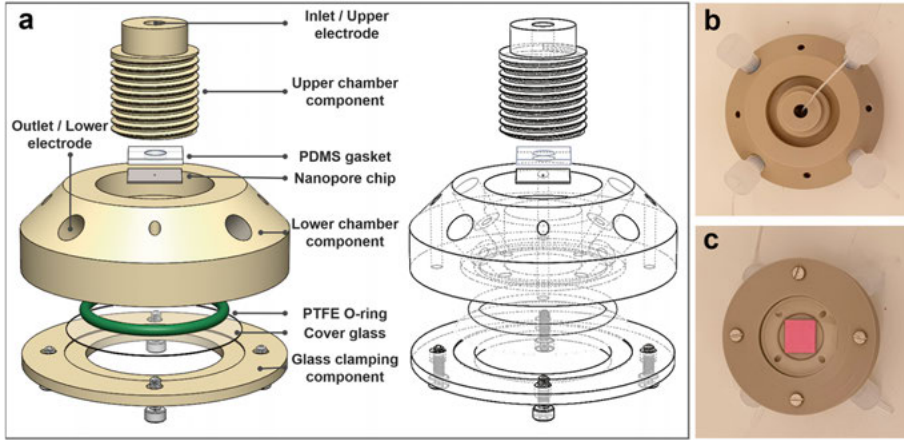


Figure 4.8: (a) Schematic fluidic cell design for the optical observation; (b) and (c): Optical images from the top and bottom view, respectively, of the assembled fluidic cell to host a $1 \times 1 \text{ cm}^2$ nanopore chip installed.

4.3.3 Optical observation of DNA translocation

To evaluate the efficacy of lipid bilayer coating, we recorded the DNA motion and clogging events in a TPP array by means of confocal fluorescence microscopy. With the fluorescent labeled lipids visualized, a homogeneous lipid bilayer coating can be observed on the TPP array surface (Figure 4.9a and b). λ -DNA labeled with TOTO-1 was used to conduct the translocation experiment under 200 mV applied bias for 10 minutes. As shown in Figure 4.9c, multiple pores are obviously clogged by λ -DNA after the translocation experiment. The clogged pores show various fluorescent intensities, which implies that multiple λ -DNA strands can clog in a 30 nm TPP. As observed in Figure 4.9d, the fraction of clogged pores is significantly reduced, which indicates the excellent non-fouling property of the lipid bilayer to DNA molecules. The clogged pores with the lipid bilayer may result from the defects in the lipid bilayer on the pore sidewalls. In Figure 4.9e, the statistical result verifies that the percentage of clogged pores drops from 36% to 7% after coating with the lipid bilayer. Nevertheless, these observations indicate that the irreversible pore clogging by DNA poses a serious concern in nanopore sensing applications. Figure 4.8f shows a representative confocal fluorescence micrograph that captures the translocation of a single λ -DNA molecule in the *cis* chamber and a pore clogged with λ -DNA. The image was obtained from an x-z scan (along one row of the TPP array) through the membrane. A much higher capture rate would be required in future studies and the direct visualization of DNA translocation from the cross-sectional view could be further used for the investigation of the DNA dynamic motion close to the pore.

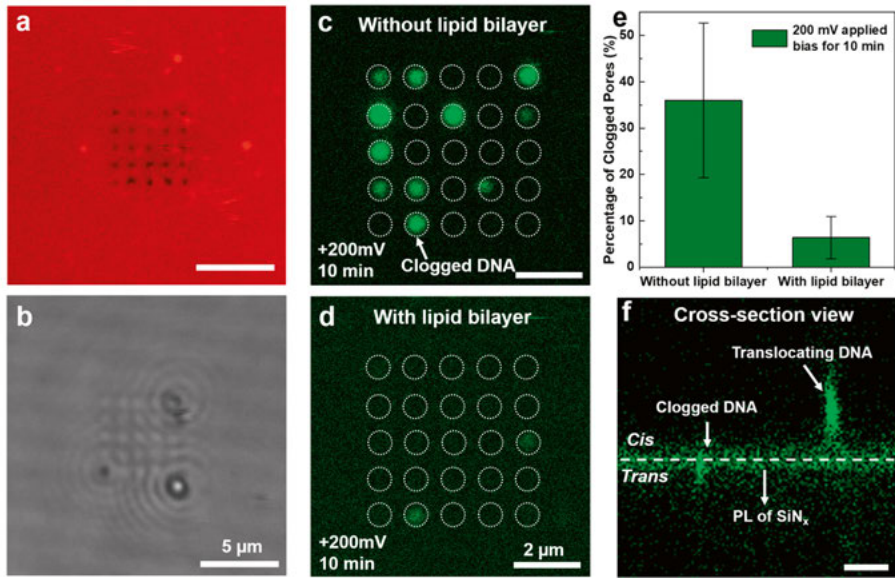


Figure 4.9. Visualization of DNA translocation and clogging in a 30 nm TPP array with and without lipid bilayer coating: (a) A fluorescence micrograph of the lipid bilayer coated TPP array area; (b) Corresponding bright field image of (a); (c) and (d): Fluorescence images of the TPP array clogged with fluorescent labeled 48.5 kb λ -DNA after a 10 min translocation at 200 mV bias, without or with lipid bilayer, respectively; (e) Statistical results of the percentage of clogged pores with λ -DNA after applying a 200 mV bias for 10 minutes; (f) A confocal cross-sectional view of the fluorescent labeled λ -DNA translocation versus clogged in the TPP array, scale bar: 2 μm . Reproduced from Paper IV. Copyright (2020) IEEE.

5. DNA clogging on HfO_2 nanopore arrays

While the previous two chapters have presented that organic coatings are effective to reduce nonspecific adsorption, to date, for nanopore-based DNA sensing, the most common pretreatment is an aggressive cleaning using Piranha solution, mainly due to ease of implementation and rendered hydrophilic surfaces [134]. But under the continuous passage of considerable amounts of DNA molecules during the measurement, the tendency to interact with pore walls can still lead to occasional DNA clogging in the pore. Without further surface coating but only Piranha treatment, DNA clogging in various size nanopores has been reported [71, 135]. However, a detailed understanding of the clogging mechanism of DNA molecules and the governing experimental factors is still lacking. This motivated us to systematically investigate the DNA clogging behavior based on the developed optical sensing platform (as schematically shown in Figure 5.1). The corresponding experimental design should be based upon a nanopore device that enables a reliable and quantitative recognition of DNA clogging events. Therefore, a HfO_2 coating is employed to prevent the pore expansion during the repetitive usage of the Si-based TPP arrays.

In this chapter, the characterization of HfO_2 coated Si nanopore arrays is first presented in section 5.1. In section 5.2, the investigation of DNA clogging behavior in sub-20 nm nanopores by direct optical observation is discussed. Finally, in section 5.3, an analytical model is developed in order to assist our understanding of the experimental results.

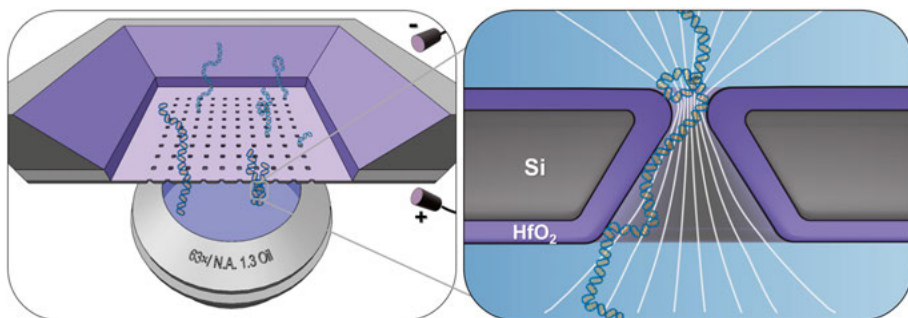


Figure 5.1. Schematic setup for optical observation of DNA clogging events during the translocation through an HfO_2 coated Si nanopore array.

5.1 Coating HfO_2 on Si nanopore arrays

The Si TPP arrays were fabricated by aforementioned process and an additional 5 nm thick HfO_2 layer was coated by means of ALD. As seen in Figure 5.2a, SEM images show a well-defined 10-by-10 HfO_2 coated nanopore array and a single pore. In a typical nanopore array, the fitted diameter of the bottom opening measures 15 nm with a standard deviation of 3 nm (Figure 5.2b). Corresponding cross-sectional SEM images in Figure 5.2c demonstrate the evolution of nanopore shape at different steps along the fabrication process: (i) the initial Si pore in the truncated-pyramidal geometry resulting from the anisotropic etching of Si crystal in KOH solutions; (ii) a slightly concaved interior of the Si pore caused by the RIE for removal of the PL-generating SiN_x mask layer; and (iii) the conformal 5 nm thick HfO_2 coating of the nanopore resulting in a homogeneously shrunk pore with a rounded pore edge

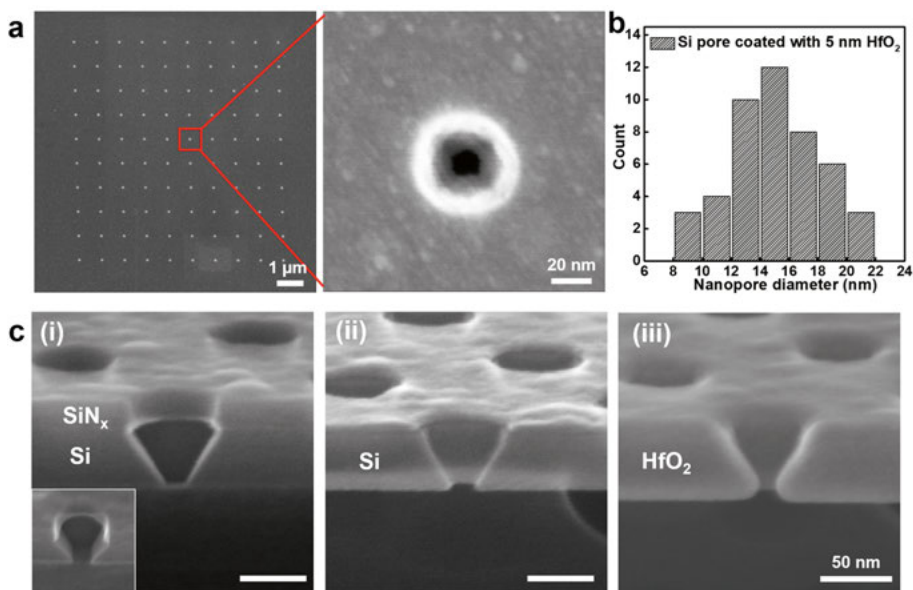


Figure 5.2. Characterization of HfO_2 coated Si nanopore arrays. (a) (Left) SEM image of the 10-by-10 nanopore array; (Right) Top-view SEM image of a single pore. (b) Histogram of the diameter of the small openings of the HfO_2 coated Si nanopore array. The diameter was acquired by fitting the small opening profile to an ellipse and averaging the major and minor axes of the fitted ellipse. (c) Cross-sectional SEM images of the nanopore structure: (i) as-formed and before the removal of the SiN_x hardmask. The inset is obtained with a 45° tilted viewing angle; (ii) after the removal of the SiN_x layer by means of RIE. (iii) after ALD of a 5 nm thick conformal HfO_2 layer. Reproduced from Paper V with an open access permission.

The geometry and elemental composition of the HfO_2 nanopores were further corroborated using TEM and energy dispersive X-ray spectroscopy (EDX) analysis, see Figure 5.3. The quantitative EDX mapping images in Figure 5.3 show the 2D spatial composition of the three involved elements. The Si signature (red) is strong from the surrounding membrane and starts decreasing from the top edge of the pore. Conversely, the EDX maps of Hf (purple) and O (green) display a gradual increase in atomic percentage along the radius of the pore towards the center. Hence, the HfO_2 layer is shown to conformally cover the TPP Si pore and the results EDX are consistent with the SEM data.

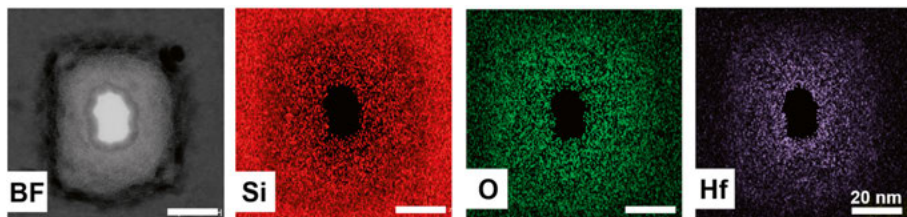


Figure 5.3. TEM image of the HfO_2/Si nanopore and EDX mapping images of the detected elements of silicon (red), oxygen (green), and hafnium (purple). Reproduced from Paper V with an open access permission.

5.2 DNA clogging behavior in nanopore arrays

To take advantage of the array form of pores, we investigated the DNA clogging phenomenon by using confocal fluorescence microscopy, especially focusing on its dependence on DNA length, applied voltage, and surface charge. Detailed experimental description can be found in Paper V.

5.2.1 Effects of DNA lengths and applied voltages

A series of fluorescence micrographs are depicted in Figure 5.4a to visualize how the 10 kbp dsDNA molecules clog in a 10-by-10 nanopore array at a 600 mV transmembrane voltage. With passing the DNA molecules through the nanopore array, some of the nanopores became clogged as the displayed fluorescent signals remain constant in Figure 5.4a. Noticeably, some pores can become declogged and an example is marked by the two dashed white ovals, obviously a temporary clogging case. The clogged pores can also show varying fluorescence intensity as a result of single pores being accreted by multiple DNA molecules. Three time-integrated fluorescence images are shown in Figure 5.4b, each representing the accumulated signals from 1034 frames obtained in a 300 s recording.

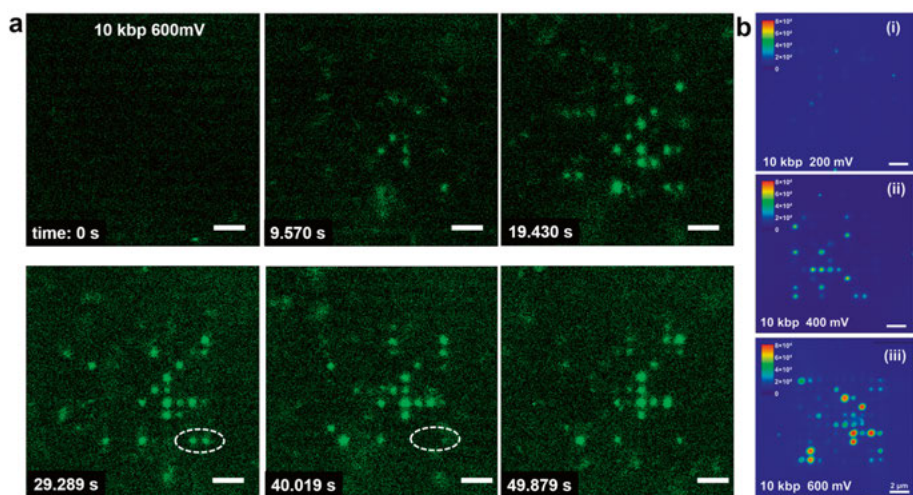


Figure 5.4. Behavior of DNA clogging in HfO_2 coated nanopore arrays. (a) Fluorescence frames of 10 kbp dsDNA clogged nanopore array biased at 600 mV. Images are extracted from a real-time recording for 300 s at 3.45 fps frame rate. The white dashed ovals mark two pores that are released from clogging by comparing with the respective state in the previous frames. Scale bar: 2 μm . (b) Images showing the integrated fluorescent signals from 1034 frames (taken in 300 s) for the 10 kbp dsDNA molecules at the pore positions at 200 mV (i), 400 mV (ii), and 600 mV (iii). Reproduced from Paper V with an open access permission.

The difference in clogging extent of the 10 kbp DNA is observed under different bias voltages. The degree of clogging is further analyzed by extracting the mean intensity in the nanopore region from the time-integrated images. This mean integrated intensity is found in Figure 5.5a to be significantly higher at 600 mV than that at 200 mV or 400 mV, indicating a stronger tendency of DNA molecules residing in the nanopores at higher bias voltage. The number of clogged pores is found in Figure 5.5b to grow with time and the growth appears to be faster at higher bias voltage. The clogging level is evaluated every 3 s by comparing with the previous frames. To further assess the effect of bias voltage and DNA length on pore clogging, a quantitative analysis of the clogging probability is performed. The percentage of clogging is evaluated at the end of 300 s recordings. Results of four independent experiments are taken into the statistical analysis for each data group. A steady increase in clogging percentage with DNA length is evident in Figure 5.5c. The bias dependence of clogging is found weaker for the 1 kbp dsDNA than for the longer counterparts. In the used bias range, the clogging percentage is below 10% for the 1 kbp dsDNA, whereas it reaches 30%, 40%, and 56% for the 5 kbp, 10 kbp, and 20 kbp dsDNA, respectively.

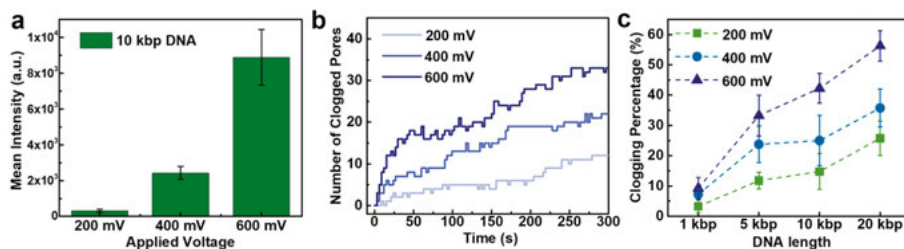


Figure 5.5. Statistical results of DNA clogging behavior: (a) Mean intensity of the integrated fluorescence signals at different bias voltages in the region of pore positions obtained from (Figure 5.4b). (b) Plots of the number of clogged pores by the 10 kbp dsDNA molecules versus time at different bias voltages. The clogging state is evaluated every 3 s. (c) Statistical results of the clogging percentage for 1 kbp, 5 kbp, 10 kbp, and 20 kbp dsDNA measured at 200 mV, 400 mV, and 600 mV. The clogging percentage is extracted from the last frames at the end of the 300 s recording. Reproduced from Paper V with an open access permission.

With our nanopores with an average diameter of 15 nm, lengthy DNA strands can enter with complex molecular configurations, *e.g.* coils, multiple folding or knots [136], in addition to the simple and ideal linear shape. Such specific configurations have been well-characterized using similarly-sized pores in previous studies [136-138]. The knotting probability of linear dsDNA molecules is experimentally shown to rise with the DNA length, *e.g.* a 13.2% knotting probability is found for 20.7 kbp DNA molecules probed with 20 nm SiN_x nanopores [136]. Hence, the observed dependence of clogging probability on DNA length is likely induced by the translocating DNA molecules assuming the aforementioned complex configurations. This hypothesis can be rationalized by considering that the tendency of folded or knotted DNA molecules sticking to the pore surface is higher due to an increased area of interaction and a shortened distance between each DNA segment and pore walls. As for the voltage dependence of clogging probability, it can be attributed to the difference in translocation frequency. As previously discussed in section 2.3, the translocation of dsDNA molecules in large pores follows a linear dependence of translocation frequency on voltage and is dominated by a barrier-free capture process. Hence, it is reasonable to ascribe the observed increasing clogging probability with voltage to an increased translocation frequency.

5.2.2 Temporary clogging behavior

To investigate temporary clogging events, the x-t scan mode provided by the confocal microscope was employed to acquire fine time-resolved images with a temporal resolution of 0.56 ms. The representative x-t scan image of 10 kbp dsDNA translocating the pores at 400 mV displayed in Figure 5.6a (right). It clearly shows a temporary clogging event as well as a persistent clogging of

the pore in the middle of the column. Probable DNA translocation events could also be captured by benefiting from the sub-millisecond scan resolution, as noted in Figure 5.6a. To further characterize the temporary clogging behavior, x-t scan measurements for 5 kbp and 10 kbp dsDNA at different bias voltages were performed. Histograms of the lifetime for over 30 temporary clogging events are plotted in Figure 5.6b wherein the characteristic clogging time scales and the errors are extracted by curve fitting with an exponential function. As can be seen, the majority of the events have a lifetime below 2000 ms. Notably, with the increase of the applied voltage from 200 mV to 600 mV, the characteristic clogging time for 5 kbp and 10 kbp dsDNA decreases. The near-neutral or positively charged HfO₂ surface at pH 7, as the isoelectric point of HfO₂ is 7~8 [139], is expected to induce an EOF force that reinforces the electrophoretic force exerting on the clogging DNA molecules. Therefore, the observed temporary clogging events with our HfO₂ pores are most likely ended with DNA translocating to the *trans* chamber under the combined action of EOF and electrophoresis.

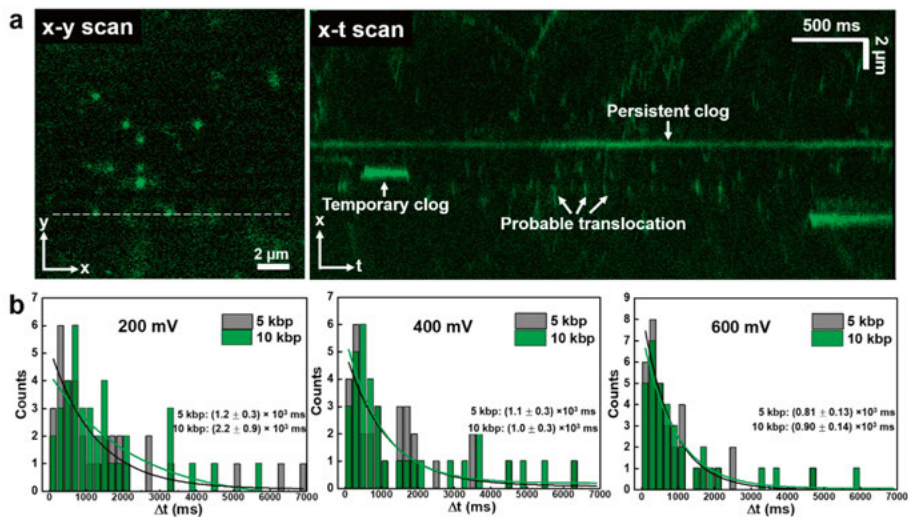


Figure 5.6. Time-resolved study of temporary clogging of DNA HfO₂ nanopore arrays by confocal x-t scans. (a) Fluorescence images of pore clogging acquired by an x-y scan (left) and an x-t scan (right). The white dashed line in the x-y scan marks a row of nanopores that is scanned in the x-t scan mode. In the x-t scan image, the horizontal dimension represents the temporal evolution, where the length of the clogging fluorescent signal denotes the lifetime. (b) Histograms of the temporary clogging lifetime of 5 kbp and 10 kbp dsDNA at 200 mV, 400 mV, and 600 mV. Curve fitting of the histograms with an exponential function is marked as solid lines, with the fitting parameters given in the figures. Adapted from Paper V with an open access permission.

5.2.3 Effects of solution pH values

To investigate the effects of solution pH values, the surface charge density of the pore walls was first characterized by measuring the conductance of single nanopore in electrolytes of different conductivity and then fitting the conductance vs. conductivity data based on a well-established procedure [83, 140]. The extracted surface charge density is $+8.2 \text{ mC/m}^2$, $+3.9 \text{ mC/m}^2$, and -6.2 mC/m^2 at pH of 5, 7, and 9, respectively, see Figure 5.7a. The degree of clogging at different pH was evaluated based on a quantitative analysis of the pore clogging percentage after a 300 s optical observation at 200 mV. The average clogging percentage displayed in Figure 5.7b for 5 kbp and 10 kbp dsDNA at pH 5, significantly higher than those at pH 7 and pH 9. Since the more protonated surface at pH 5 results in higher positive surface charge density, the negatively charged DNA molecules are exposed to a stronger electrostatic attraction force than that at pH 7. A further factor to consider is how the EOF and electrophoretic forces can collaboratively play in the DNA-pore interactions. It has been reported that EOF with an opposing direction to electrophoretic force can slow down the translocation speed of DNA molecules [141]. In this regard, the chance for DNA molecules to interact with pore walls will increase. These findings suggest that the DNA clogging probability can be modulated by altering the electrolyte pH, whereas it is affected by two distinct manners: (i) the strength of electrostatic attraction influenced by the surface charge density and (ii) the direction of EOF dragging force determined by the surface charge polarity.

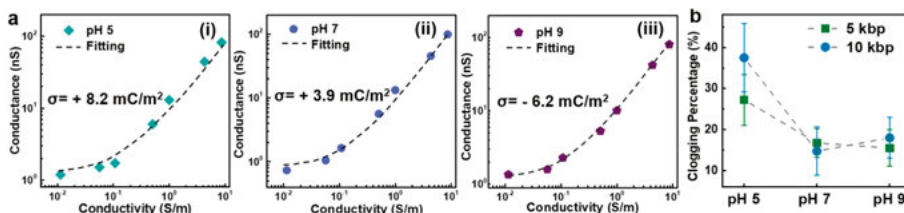


Figure 5.7. Effects of electrolyte pH on the nanopore surface charge and clogging probability: (a) Conductance vs. conductivity relationship for single HfO_2 coated nanopore at (i) $\text{pH}=5$, (ii) $\text{pH}=7$, and (iii) $\text{pH}=9$. Fitting curves are marked as dashed lines. (b) Clogging percentage of 5 kbp and 10 kbp dsDNA in nanopore arrays at different pH, at 200 mV for 300 s. Reproduced from Paper V with an open access permission.

5.3 Analytical model for accounting clogging behavior

By referring to the previous theoretical studies [142, 143], an analytical model is developed to account for the observed DNA clogging phenomenon, based

on examining the energy landscape and the mean translocation time during the DNA translocation process.

5.3.1 Model building

In the model, a DNA molecule threads through a positively charged conical pore in three basic steps: (i) the front segments of a translocating DNA strand enter the pore from its small opening, (ii) the DNA segments transfer to the trans side and the pore is filled with the DNA, and (iii) the tail segments of the DNA strand exit from the pore. Since a translocating DNA may assume complex configurations with folding or knotting, the model simplifies the translocating DNA strand as a bundle of different number of DNA strands (illustrated in Figure 5.8).

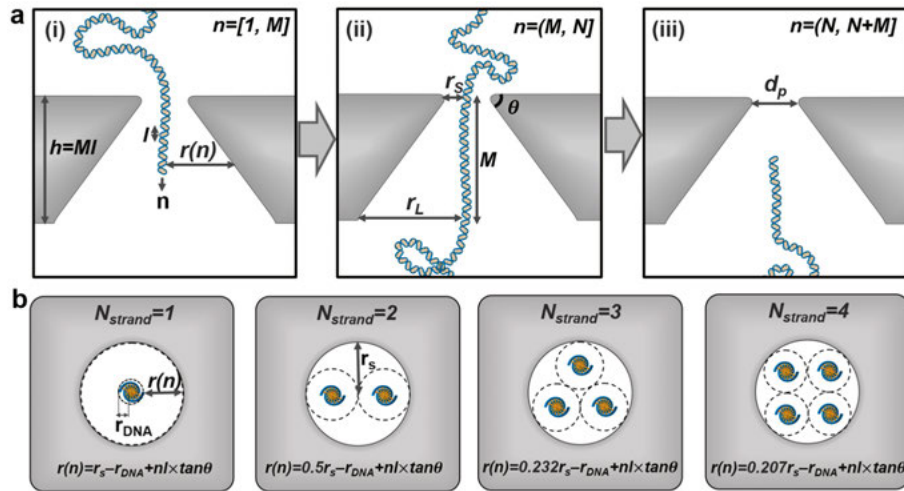


Figure 5.8. Schematics of DNA translocation process with single-file or bundles through a conical nanopore: (a) Three stages of the DNA translocation with single-file configuration: (i) DNA entering the pore; (ii) DNA translocating the pore; and (iii) DNA exiting from the pore, where d_p is the diameter of the small opening of the pore, r_s and r_L are the radius of the small and large opening of the pore, respectively, n is the position of the DNA molecule, N is the number of base pairs in the DNA strand, M is the number of base pairs that can be accommodated by the pore with a single-file configuration, l is the average distance between two base pairs, θ is the conical angle of the pore, and $r(n)$ is the closest horizontal distance between the n th base pair surface and the pore surface. (b) The top views present the hypothesized distribution of multiple DNA strands located in the conical nanopore, where N_{strand} is the number of DNA strands located in the pore and the mathematical expressions for calculating $r(n)$ are denoted in different N_{strand} cases.

By referring to the established models, the energy of the electric field driven DNA translocation process is assumed to consist of four energy components: (i) conformational entropic energy of DNA (F_{en}), (ii) electric potential energy of DNA gained from the external electric field (F_{el}), (iii) electrostatic energy (ε_Q), and (iv) hydrophobic interaction energy (ε_{hy}) between DNA and pore walls (details of mathematical derivation described in the supporting information of Paper V). Therefore, the total energy (F_t) of the translocating DNA is given by:

$$F_t = F_{en} + F_{el} + \varepsilon_Q + \varepsilon_{hy} \quad (5.1)$$

The DNA translocation time is examined in our model to evaluate the level of DNA-pore interactions as an important indicator for the occurrence of DNA clogging. Based on the derived energy landscapes, the mean translocation time (τ) can be calculated with reflecting boundary conditions from the following equation [142],

$$\tau = -\frac{1}{\kappa} \int_0^{N+M} dn \int_0^n dn' \exp \left[\frac{F_t(n)}{kT} - \frac{F_t(n')}{kT} \right] \quad (5.2)$$

where κ is a parameter denoting the local friction of the base pair and definition of other symbols is described in the caption of Figure 5.8.

5.3.2 Model results

Typical F_t landscapes are compared in Figure 5.9a for a single DNA molecule of length 5 kbp ($N = 5000$) translocating in a conical pore. At $V = 0$ mV, the entropic energy dominates with a barrier height of $4.5kT$. Hence, translocation is an unfavorable process due to loss in conformational entropy. At $V = 100$ mV, the electric potential energy dominates with an energy lowering along the translocation trajectory. For four types of translocation configurations with N_{strand} to denote the number of bundled DNA strands, the calculated τ with different sets of parameters as a function of d_p , V , and σ are plotted in Figure 5.9b, c, d, respectively.

In Figure 5.9b, it is apparent that τ increases drastically at different threshold values of d_p for different N_{strand} ; smaller d_p allows for translocation of bundles with smaller N_{strand} , while bundles of a too large N_{strand} can immediately clog as indicated by the sharp rises of the curves. The DNA-pore interactions are stronger for larger N_{strand} due to a combination of a larger number of interacting base pairs with a shorter average distance between DNA strands and pore walls.

In Figure 5.9c, significant increase of τ occurs below 100 mV for $N_{strand} > 1$, which is again caused by the strong DNA-pore interaction. Hence, DNA molecules are more prone to clogging the pore at lower voltages for individual translocation events, which is consistent with the observed voltage dependent

lifetime of temporary clogging. On the other hand, this effect can be overwhelmed by the higher translocation frequency at higher voltage, see Figure 5.5c.

How τ would vary with σ is illustrated in Figure 5.9d. The electrostatic interaction between DNA and pore walls is obviously insignificant for the translocation of unfolded ($N_{strand} = 1$) and double-folded DNA ($N_{strand} = 2$), but becomes governing for that of thicker bundles of DNA strands, as evident from the rapid increase of τ beyond a certain σ value. In short, a stronger electrostatic interaction at higher surface charge density will lead to a higher probability of clogging for multi-folded or knotted DNA molecules, supporting the preceding experimental observations. In brief, this model, despite its simplicity, appears to provide a good account of our experimental data regarding the clogging dependence on DNA length, concentration and solution pH.

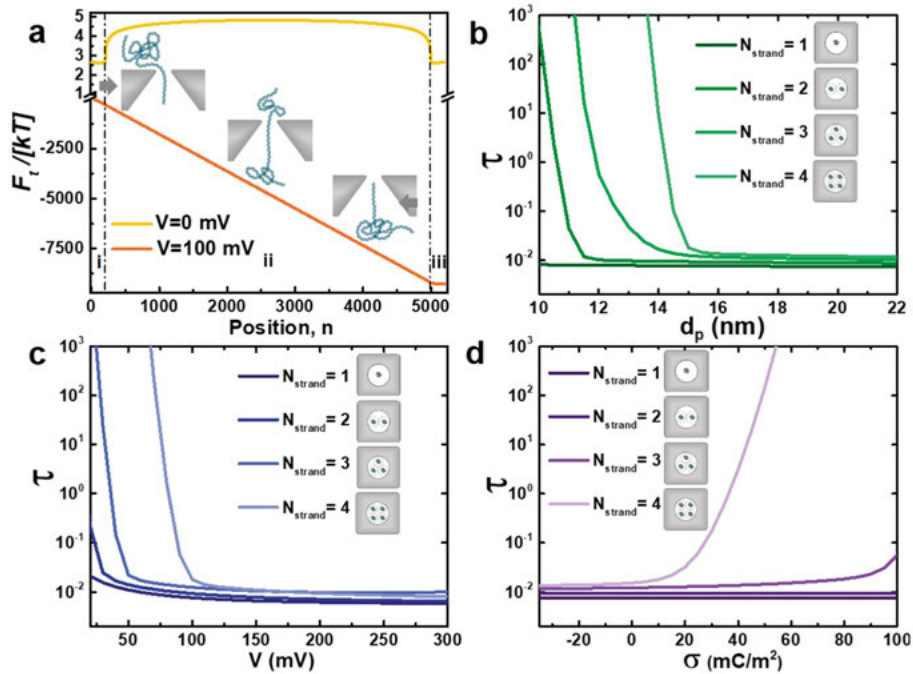


Figure 5.9. Evolution of total energy during translocation and dependence of translocation time on a few representative parameters. (a) Energy landscape of DNA translocation at $V = 0$ mV and at $V = 100$ mV, $M = 200$, $N = 5000$, $d_p = 15$ nm, $\theta = 54.7^\circ$, $\sigma = +10$ mC/m². Different regimes are denoted: (i) DNA entering the pore; (ii) DNA translocating across the pore; and (iii) DNA exiting from the pore. (b) τ as a function of d_p , $V = 50$ mV and $\sigma = +10$ mC/m². (c) τ as a function of V , $d_p = 15$ nm and $\sigma = +10$ mC/m². (d) τ as a function of σ , $V = 50$ mV and $d_p = 15$ nm. Adapted from Paper V with an open access permission.

6. Docking of DNA polymerase on nanopores

One significant factor hampering the nanopore-based biosensing is the fast translocation of analyte through the pore, which limits the extraction of detailed molecular information of the analyte. The realization of DNA sequencing based on biological nanopores relies on a critical step of docking a motor enzyme, DNA polymerase (DNAP) or helicase, on the pore to drastically increase the residence time of nucleobases in the sensing region. However, studies utilizing this sensing scheme in solid-state nanopores are few in number. One of the concerns is that the docked enzyme may suffer denaturation due to the undesirable docking orientation in a confined space or strong interactions between the enzyme and the pore surfaces. Hence, such attempts on solid-state nanopores should be pursued in a high-throughput manner, which would allow for a thorough examination of both active and inactive enzyme docking. This line of thoughts has motivated us to use our developed optical observation platform and nanopore array device to explore the docking behavior of DNAP, as illustrated in Figure 6.1.

In this chapter, characterization of TPP devices with a shrunk pore size and label-free optical detection method using Ca^{2+} indicator dye is first described in section 6.1. Then, both electrical and optical detections of phi29 DNAP docking on TPPs are discussed in section 6.2.

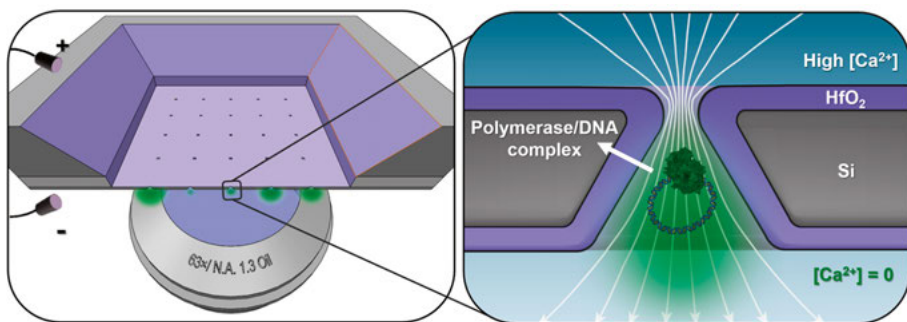


Figure 6.1. Schematic of the optical read-out setup for label-free detection of polymerase-DNA complexes docking on an HfO_2 coated nanopore array.

6.1 Device and detection system

6.1.1 Shrinkage of pore diameter by means of ALD

Due to the limitation of our fabrication process, the initial pore diameter that could be reliably obtained in TPP arrays (≥ 20 nm) was too large to dock the DNAP. Hence, shrinking the pore diameter was necessary. ALD coating of HfO_2 was again employed by considering its excellent chemical stability and PL-free property shown in the preceding chapter and Paper V. In the ALD process, an optimized gas flow of the precursor is prerequisite to obtain a homogeneous conformal coating layer. However, we found that the chip configuration in the reaction chamber and the dimension of nanopore opening size could influence the flow of gas phase and result in non-ideal coating. As illustrated in Figure 6.2a, with a laying-chip configuration of the nanopore chip, the rear-side cavity could create an isolated chamber from the bulk gas phase, which would lead to agglomeration of the precursor at the pore opening due to the perturbed gas flow there. The TEM images in Figure 6.2a indeed show that the laying-chip configuration result in a total pore blockage after coating of a 5 nm thick HfO_2 on a TPP of an initial diameter above 20 nm. As shown in Figure 6.2b, with a standing-chip configuration, the precursor gas could reach both sides of the free-standing membrane evenly. TEM images show that an ideal conformal coating is achieved with the standing-chip configuration.

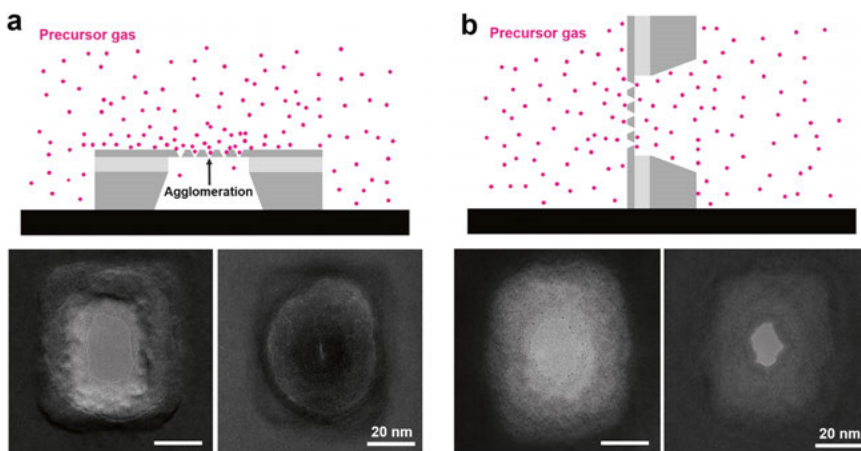


Figure 6.2. Illustrations and TEM images of shrinking nanopore by means of ALD with two types of chip configuration in the reaction chamber: (a) Illustration (top) of a laying-chip configuration with the rear-side cavity creating an isolated chamber from the bulk gas phase. TEM images of the pore before (left) and after (right) coating a 5 nm HfO_2 show a total pore blockage due to precursor agglomeration. (b) Illustration (top) of a standing-chip configuration allowing the precursor to reach the free-standing membrane evenly from both sides. TEM images of the pore before (left) and after (right) coating of a 5 nm HfO_2 show a conformal shrinkage of the pore opening.

Given that the phi29 DNAP molecule is about 5-8 nm in diameter (shown later in Figure 6.5a), a sub-5 nm TPP is necessary to totally prevent the translocation of DNAP. However, we found that the HfO_2 coating tended to bridge together and close the pore at such small pore size (see Figure 6.3a), which could also arise from an unstable precursor gas flow in the tiny nanopore channel during ALD process. Therefore, as a compromise, the pore shrinkage by means of ALD was set to an average size of 8 nm for the docking experiments. SEM images of a shrunk TPP and a TPP array are, respectively, shown in Figure 6.3b and c. The slight nonuniformity of the pore size across the TPP array was also expected to cause DNAP docking.

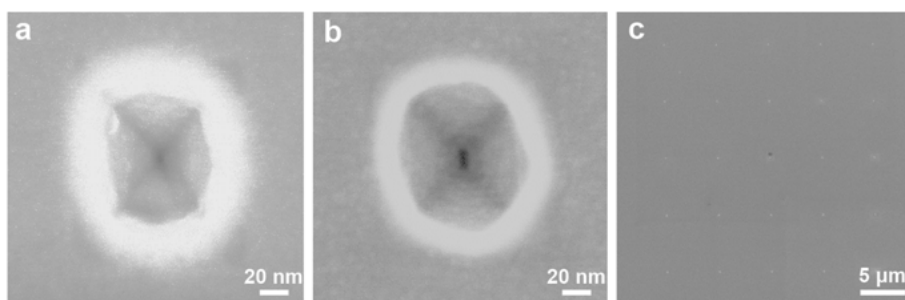


Figure 6.3. (a) A blocked TPP pore after coating of HfO_2 to shrink the pore size. (b) SEM image of a single TPP with the short opening length of 8 nm. (c) SEM image of a 5-by-5 HfO_2 coated TPP array with a pore spacing of 6 μm .

6.1.2 Characterization of optical label-free detection method

To optically detect the docking events of DNAP on the TPP arrays, common fluorescent labeling strategies may suffer from limitations such as weak signals with few labeled fluorophores and the tendency of photobleaching upon long exposure to laser excitation. It is also practically difficult to label DNAP. Thus, a label-free optical detection method was employed to probe the docking of DNAP on the TPP arrays. This method, as illustrated in Figure 6.4a, uses Fluo-4 as a fluorescent reporter molecule for the Ca^{2+} concentration in the vicinity of the nanopore. The flow of Ca^{2+} ions can be inferred by measuring the fluorescence signals on site of a nanopore. To confirm that the fluorescence intensity generated in the nanopore region was a positive function of the magnitude of Ca^{2+} flux through the pore, the fluorescence intensity was measured using confocal imaging with 20 μM Fluo-4 as a function of both Ca^{2+} concentration and applied bias voltage. As shown in Figure 4b and c, the fluorescent intensity is voltage-tunable and rises above the background level at an onset voltage of -50 mV and higher intensity values are measured at higher bulk CaCl_2 concentration at the same voltage.

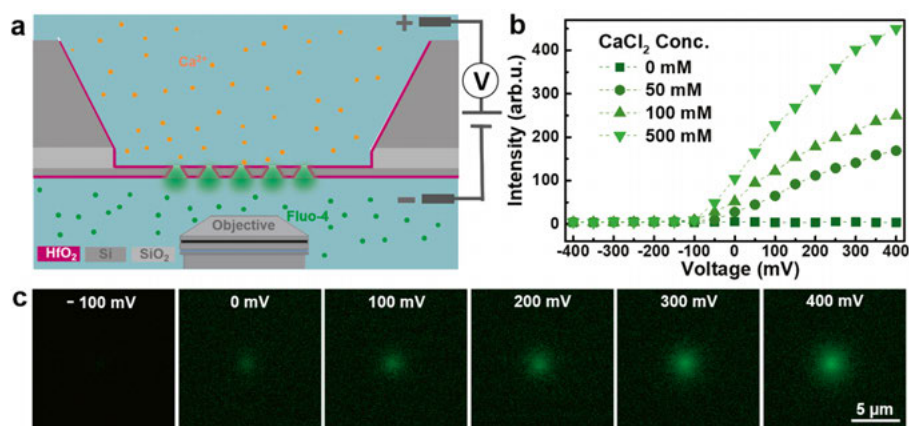


Figure 6.4. (a) Schematic of the label-free optical detection principle with Fluo-4 in the cis chamber and CaCl_2 in the trans chamber. (b) Fluorescence intensity as a function of applied bias voltage at different bulk CaCl_2 concentration. (c) Micrographs showing the fluorescence signals from one TPP pore at different bias voltages with a bulk CaCl_2 concentration of 100 mM.

6.2 Docking of DNA polymerase

To investigate the behavior of DNAP docking onto TPPs with a comparable size, both electrical measurement and optical detection were carried out. The phi29 DNAP was pre-bound to a circular ssDNA template hybridized with a primer. Detailed experimental description can be found in Paper VI.

6.2.1 Electrical detection on single pore

The negatively charged DNAP-template complex could be electrophoretically driven to the TPP. At a +200-mV bias voltage, clear translocation events and long-duration docking events of the DNAP-template complex could be identified by monitoring how the ionic current traces varied with time, and typical examples of such traces are shown in Figure 6.5b. Since the pore size of the used TPP arrays was not sufficiently small to totally prevent the translocation of the DNAP-template complex, the majority of detected events were likely related to translocations. A few docking events with sustained current blockades were also apparent, as shown in Figure 6.5c. This observation was further confirmed by analyzing the distribution of the event amplitude and duration in Figure 6.5d. A large population of the detected events had a duration time in the range of 1 to 100 ms, while a smaller population was beyond 100 ms with a few events lasting for seconds.

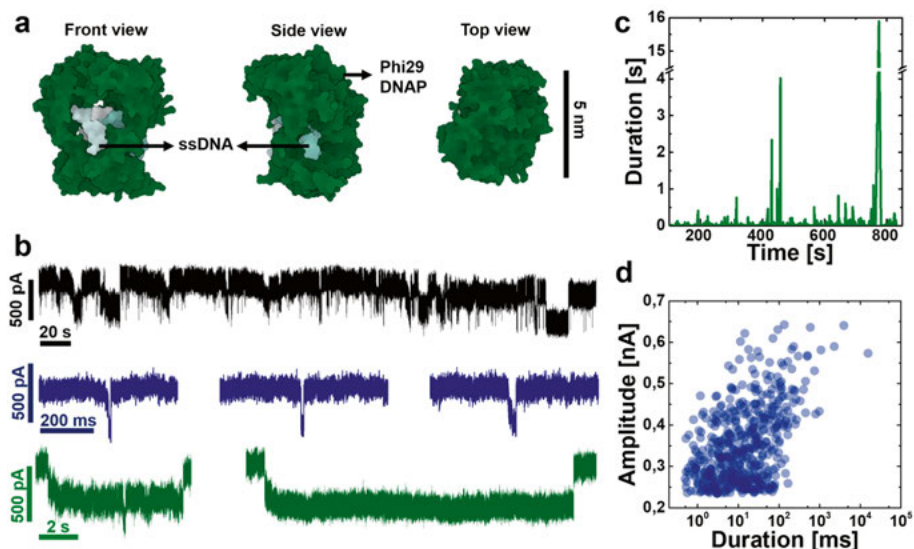


Figure 6.5. Electrical monitoring of DNAP docking on a single TPP: (a) Molecular surface structure of phi29 DNAP bound with an ssDNA molecule from different viewing angles. Images are obtained from Protein Data Bank (PDB), the PDB ID of this complex structure is 2PY5. (b) Typical ionic current traces of the phi29 DNAP bound with a circular DNA template at 200 mV passing/docking an 8-10 nm single TPP: a continuous ionic current trace (black); example traces of translocation events (blue) and docking events (green). (c) Amplitude and duration of detected events collected from the DNAP docking measurement at 200 mV. (d) Event duration vs time analyzed from the current trace shown in (b).

Protein translocation in solid-state nanopores is often characterized by a speed exceeding the electrical measurement bandwidth [144-146]. Notably, the mean protein translocation time is reported to be about 1 μ s for proteins with a range of molecular weights [147]. In this study, the prolonged translocation events with a dwell time beyond 1 ms is likely due to the electrostatic attraction between the negatively charged DNA template and the positively charged HfO₂ pore sidewalls, which has been discussed in Chapter 5 and Paper V. The events with a distinctive extraordinarily-long dwell time beyond 1 s and a high blockade amplitude were regarded successful in docking of the DNAP onto the TPP. Such docking events were unstable because the electrophoretic force in collaboration with the electroosmotic force might force the complex to pass through the pore once its orientation relative to the pore would favor such a movement. The dynamics of this movement have been investigated on docking streptavidin-DNA complex on a 4 nm SiN_x pore [148].

6.2.2 Optical detection on pore arrays

Optical detection of docking DNAP-template complex was carried out on a 5-by-5 TPP array. As shown in Figure 6.6a, with 20 μM Fluo-4 in *cis* and 50 mM CaCl_2 in *trans* at 200 mV, most of the TPPs in the array produced fluorescent signals at $t=0$ s, indicating the presence of a Ca^{2+} ion flux. The variance of intensity was likely due to the nonuniformity of the pore size with the TPP array. Two pores closed by ALD coating showed no signal, which are marked with a white dashed circle. With a continuous recording for 30 s, obvious docking events can be identified at two pore positions marked with red and blue dashed circles by comparing with the respective state in the previous frames (Figure 6.6a). The profile of fluorescent intensity vs time at the two positions was extracted and shown in Figure 6.6b. The decreased fluorescence intensity lasting over seconds for pore 1# is a clear evidence of a DNAP-template docking onto the TPP pore. In the case of pore 2#, it was also observed that the DNAP-template complex could pass through the pore after roughly 10 s of docking, which is consistent with the electrical measurement of docking events on single TPP. Notably, the 50 mM of CaCl_2 used in the detection here is compatible with the phi29 DNAP for DNA synthesis [149], which is desirable for maintaining the activity of the DNAP.

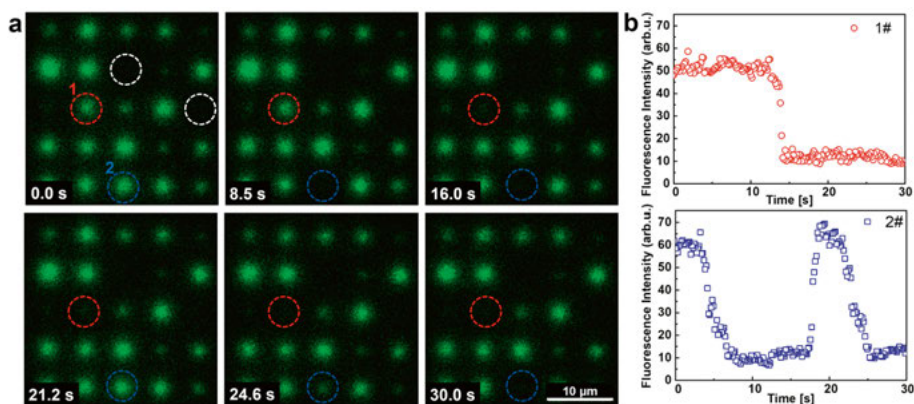


Figure 6.6. (a) A set of fluorescence frames of docking DNAP-template complex onto a 5-by-5 TPP with 20 μM Fluo-4 in *cis* chamber and 50 mM CaCl_2 in *trans* chamber at 200 mV. The white dashed circles mark pores without fluorescence signal. The red and blue dashed circles mark two pores showing docking signals. (b) Fluorescence modulations associated with docking DNAP-template complex at 200 mV for the two marked pores in (a).

7. Summary and outlook

Revisiting Confucius' quote in the preface, to engineer surfaces of solid-state nanopores for biomolecule sensing resembles to sharpen craftsman's tool for excelling his work. The work presented in this thesis is both an exploration of various surface tailoring strategies and an examination of several surface associated phenomena on solid-state nanopores. Based on the parallel sensing concept using arrayed pores, optical readout is mainly employed throughout the whole study.

For the exploration of various surface engineering approaches, the main achievements are:

- Development of a flexible and general surface patterning strategy for specific immobilization of target biomolecules based on selective PVPA passivation and EBID technique, which was further demonstrated on SiN_x nanopore arrays for nanoparticle localization.
- Adaption of the vesicle rupture-based lipid bilayer coating method onto truncated-pyramidal shape Si nanopore arrays, and validation of the efficacy of lipid bilayer to minimize DNA-pore interaction via parallel optical observation.
- Engineering of the membrane materials to be PL-free based on the developed nanopore fabrication process, which provides an ideal substrate for fluorescence-based optical detection.
- Employment of HfO_2 coating by means of ALD for both preventing the expansion of Si-based pore and reducing the pore diameter below 20 nm in a well-controlled manner, which enabled reliable quantitative measurements of DNA clogging events as well as our first attempts in studying DNAP docking.

For the examination of different surface associated phenomena, the main findings are:

- Identification of the lipid bilayer formation on truncated pyramidal shape nanopores via instantaneous rupture of individual vesicles adsorbed inside the nanopores by ionic current monitoring and optical observation.
- Confirmation of that the probability of pore clogging increases with the length of DNA strands and applied bias voltage. The dependence on DNA

length can be accounted for by invoking an increased probability of knotting and folding with longer DNA strands, while that on bias is attributed to more frequent translocation events at higher voltage.

- Investigation of that the surface charge on pore walls has a prominent effect on the probability of DNA clogging through electrostatic attraction or induced EOF as a reinforcing or countering factor.
- Establishment of a free-energy based analytical model employing translocation time to evaluate DNA-pore interaction, which can well explain the observed clogging behavior caused by complex translocation configurations and strong electrostatic interactions.
- Demonstration of DNA polymerase-template complex docked onto HfO₂ coated truncated pyramidal shape nanopores with the detection method of both ionic current measurement and label-free optical observation using Ca²⁺ indicator dye.

Despite of the fact that the field of solid-state nanopore sensing has been advancing at an astonishing and accelerating pace over the past years, the gap between the presented work in this thesis and the promised sensing applications is still significant. As our research group was a newcomer in this field when my study started, the focus of my research has also shifted greatly from aiming at DNA sequencing in the beginning to the engineering of pore surfaces for tackling different surface-associated issues during the past years. However, standing at what we have achieved, the outlook of the future work can be focused on several promising directions:

- The concept of using EBID technique to generate binding domains on nanopore structure is only demonstrated by carbon deposition, which is not ideal for tailoring the local surface properties. There are a handful of choices of metal/metal oxide materials that can be deposited by means of EBID with dedicated equipment and precursors. In addition, with focused EBID, even 3D nanostructure can be obtained with nanometer resolution. In principle, it can be employed for most types of solid-state nanopores and enable the manipulation of nanopore structure and surface chemistry for improving sensing abilities, and even feasible for building plasmonic nanostructures.
- The adaption of lipid bilayer coating on truncated pyramidal shape nanopores can be expanded to different types of lipids with incorporated receptors or fluorophores for novel sensing approaches. For instance, it has been reported phospholipids have different preference to the membrane curvature, which is related to the lipid's molecular shape. Therefore, lipids with different spontaneous curvature can be employed for TPPs, where the small opening has a sharper angle than the large opening, and it allows specific lipids to locate relatively immobile at the small opening of the nanopore.

- Based on the developed PL-free nanopore arrays, a much higher temporal resolution can be achieved for studying the translocating dynamics of biomolecules with advanced optical setup of highspeed readout. And the robust HfO₂ coating is especially reliable for quantitative studies when requiring the consistency of nanopore structure. In addition, electrical measurements can be synchronized with optical observation to provide extra information.
- The docking of DNA polymerase onto TPP arrays can be further explored by examining its activity. Such efforts should be based on an accurate control of pore dimension across the array, as well as a stable control of the docking events, where a surface modification to permanently bind the docked polymerase may be needed. This type of docking scheme can be extended to other enzymes and their reaction kinetics could be probe at a single-molecule level by ionic current measurement.

Sammanfattning på Svenska

Nanoporor har kommit att bli en speciell typ av analytiskt verktyg för enstaka molekyler som har en enorm potential för detektering och karakterisering av biomolekyler som nukleinsyror och proteiner. Normalt innefattar nanopormätningen applicering av en extern spänning för att elektroforetiskt och/eller elektroosmotiskt driva biomolekyler genom nanoporer i ett isolerande membran. Genom att analysera jonströmförändringar erhålls karakteristisk information för de passerande biomolekylerna. Som ett alternativ till biologiska nanoporer erbjuder fasta nanoporer en anmärkningsvärd mångsidighet för biosensortillämpningar på grund av deras möjligheter att stämma av porgeometrier och dimensioner såväl som deras mekaniska robusthet och stabilitet. På grund av deras inneboende oförenlighet med biomolekyler måste dock fasta nanoporers ytor bearbetas för att användas i verkliga biosensortillämpningar. I denna avhandling är det presenterade arbetet både en studie av olika yttekniska strategier och en undersökning av flera ytassocierade fenomen på fasta nanoporer. Baserat på det parallella avkänningskonceptet med nyttjandet av grupperade porer, används huvudsakligen optisk avläsning under hela studien.

Beträffande studierna av olika yttekniska tillvägagångssätt är de viktigaste resultaten:

- Utveckling av en flexibel och allmän ytmönstringsstrategi för specifik immobilisering av målbio-molekyler baserad på selektiv PVPA-passivering och EBID-teknik, vilket ytterligare demonstrerades på grupperade SiN_x nanoporer för nanopartikellokalisering.
- Tillämpning av den vesikelbrottsbaserade lipid-dubbelskiktsbeläggningssmetoden på uppsättningar av Si-nanoporor med trunkerad-pyramidform och validering av effekten av lipid-dubbelskikt för att minimera DNA-porinteraktionen via parallell optisk observation.
- Konstruktion av membranmaterialen för att vara PL-fria baserat på den utvecklade nanoporframställningsprocessen, vilket ger ett idealt substrat för fluorescensbaserad optisk detektion.
- Nyttjande av HfO₂-beläggning med hjälp av ALD för att både förhindra expansion av Si-baserad por och att reducera por diametern under 20 nm på ett välkontrollerat sätt, vilket möjliggjorde tillförlitliga kvantitativa mätningar av blockeringshändelser av DNA.

Beträffande studierna av olika ytassocierade fenomen är de viktigaste resultaten:

- Identifiering av bildandet av lipid-dubbelskikt på nanoporer med trunkerad-pyramidform via ögonblicklig bristning av enskilda vesiklar adsorberade inuti nanoporerna genom mätning av jonström och optisk observation.
- Bekräftelse på att sannolikheten för porblockering ökar med längden på DNA-strängar och applicerad spänning. Beroendet av DNA-längd kan tas hänsyn till genom att åberopa en ökad sannolikhet för trassel och vikning för längre DNA-strängar, medan det vid förspänning tillskrivs mer frekventa translokationshändelser vid högre spänning.
- Undersökning av att ytladdningen på porväggar har en framträdande effekt på sannolikheten för DNA-blockering genom elektrostatisk attraktion eller inducerad EOF som en förstärkande eller motverkande faktor.
- Upprättande av en analytisk modell baserad på den fria energin som använder translokationstid för att utvärdera DNA-porinteraktion, vilken på ett bra sätt kan förklara det observerade blockeringsbeteendet orsakat av komplexa translokationskonfigurationer och starka elektrostatiska interaktioner.
- Demonstration av komplex av DNA-polymeras-mall dockad till HfO_2 -belagda nanoporer med trunkerad-pyramidform med detektionsmetoden baserad både på jonströmmätning och etikettfri optisk observation med Ca^{2+} -indikatorfärg

Acknowledgement

PhD study is a journey to dance with difficulties, challenging yet rewarding. Over the past four years, I have found myself both in great passion to explore further and deep frustration of wandering around. Still, it has been an incredible and invaluable experience for me in many ways. And all this would not happen without a number of great people whom I would like to express my sincerest gratitude here.

First, thank you, Prof. Shi-Li Zhang, for offering me an opportunity to join this interesting project led by you. Your sharp scientific thinking, meticulous working style, strict standard for excellence, and relentless passion for research are the things that I deeply admire. Your guidance leaves me enough freedom to explore my own research interest, and at the same time pushes me improving on the right track.

And thank you, Prof. Klas Hjort, for all the inspiring discussions, valuable advices, and heartening encouragement along the way. I always felt more hopeful and positive after discussing with you in our Monday meetings. And not limit to scientific topics, it has always been a pleasure talking with you, especially with your wise humor. I am truly glad to have you as one of my supervisors.

This thesis would never be achieved without all the good collaborations. I would like to thank Prof. Zhen Zhang for your generous support for me working closely with your group and all your honest advices. Thank you, Prof. Maria Tenje, for welcoming me to attend EMBLA group meetings and allowing me to freely use your lab facilities. I would also like to thank Dr. Lei Chen for the assistance with RCA technique and Prof. Daniel Aili for the help with SUV synthesis.

Special thanks go to Shuangshuang Zeng for all your dedication in nanopore fabrication and the tremendous help in so many ways, as well as Chenyu Wen for building the electrical measurement setup and the assistance with the theoretical work. I really enjoyed working with you two in the same project and all the fun time we spent together as friends.

I would also like to thank Dr. Apurba Dev for screening my thesis and the valuable comments you gave for improvement. Thank Dr. Tomas Nyberg for translating the Sammanfattning på Svenska.

My sincere gratitude also goes to the MSL staff for maintaining an organized and efficient lab, the BioVis platform for supporting in fluorescence microscopy, the Uppsala Genome Center for providing the DNA polymerase,

and the entire administration staff for all the kind help. I would also like to thank Jonatan Bagge for the IT support.

Deep thanks to all the friendly colleagues in the former and current division for building a harmonious working environment. To mention few: Xingxing Xu, thank you for your genuine kindness and warmth both at work and daily life. Besides, thank you for being such a caring neighbor of mine! Lars Riekehr, thank you for the help in TEM measurements and all the nice talks. Asta Makaravičiūtė, thank you for every positive comment and organizing the group seminars. And also, thank all the members of the Friday Beer, Uwe Zimmermann, Adam Hultqvist, Lukas Jablonka, Michelle Marie Villamayor, Sven Englund and many more, for all the cheerful and relaxed time.

Many thanks to the people in the EMBLA group for giving me a wider perspective through the weekly meetings and the pleasant company in the cleanroom. In particular, thank Laurent Barbe, Federico Cantoni and Zhenhua Liu for the generous help in the lab. Thanks, Hannah Pohlit and Ana Maria Porras Hernández, for organizing the cell lab party with me.

The NNIF badminton club is also acknowledged here for welcoming me to the weekly practices with a lot of fun games, which helps me energize my mind.

I also want to thank the friends I have met in Uppsala from my homeland: Kai Song, Feiyan Liang, Huan Wang, Jie Zhao, Yingtao Yu, Xi Chen, Qitao Hu, Xueying Kong, Jiaqi Lu, Yanyan Dong, Lei Tian, Rui Sun, Ruijun Pan, Ye Zou, Chi Zhang and many more, for all the dinners, games, laughs, talks and trips we had together, which make this journey more enjoyable and memorable.

Heartfelt and warmest thanks to Yongli Qi, Bing Zhang, Jiabin Luan and Geng Hua for being good friends in distance and inspiring me with your own stories worldwide.

Finally, I would like to acknowledge the financial support from Swedish Research Council, VR (Grant ID:621-2014-6400) and China Scholarship Council, CSC (No. 201606100043) for making this project possible and to welcome me in this fascinating and beautiful country of Sweden.

爸，姐，希望我的独立与成长已不让你们牵挂。

妈，希望你曾经的期许，有在我身上不断实现。

感谢你们给予我最深的爱，支持与理解，是它们照亮夜空，陪伴我一路前行。

References

- [1] A. Chernewski. (2010). *Pinhole history*. Available: <https://www.alternative-photography.com/pinhole-history/>
- [2] R. P. Feynman. (1960) There's Plenty of Room at the Bottom. *Caltech Magazine*. 23-36. Available: <https://resolver.caltech.edu/CaltechES:23.5.1960Bottom>
- [3] D. Deamer, M. Akeson, and D. Branton, "Three decades of nanopore sequencing," *Nature Biotechnology*, vol. 34, no. 5, 2016, pp. 518-524.
- [4] E. A. Manrao *et al.*, "Reading DNA at single-nucleotide resolution with a mutant MspA nanopore and phi29 DNA polymerase," *Nature Biotechnology*, vol. 30, no. 4, 2012, pp. 349-U174.
- [5] N. Varongchayakul, J. X. Song, A. Meller, and M. W. Grinstaff, "Single-molecule protein sensing in a nanopore: a tutorial," *Chemical Society Reviews*, vol. 47, no. 23, 2018.
- [6] S. L. Cai, J. Y. Y. Sze, A. P. Ivanov, and J. B. Edel, "Small molecule electro-optical binding assay using nanopores," *Nature Communications*, vol. 10, 2019.
- [7] N. S. Galenkamp, M. Soskine, J. Hermans, C. Wloka, and G. Maglia, "Direct electrical quantification of glucose and asparagine from bodily fluids using nanopores," *Nature Communications*, vol. 9, 2018.
- [8] J. Y. Y. Sze, A. P. Ivanov, A. E. G. Cass, and J. B. Edel, "Single molecule multiplexed nanopore protein screening in human serum using aptamer modified DNA carriers," *Nature Communications*, vol. 8, 2017.
- [9] M. Chinappi and F. Cecconi, "Protein sequencing via nanopore based devices: a nanofluidics perspective," *Journal of Physics-Condensed Matter*, vol. 30, no. 20, 2018.
- [10] L. Restrepo-Perez, C. Joo, and C. Dekker, "Paving the way to single-molecule protein sequencing," *Nature Nanotechnology*, vol. 13, no. 9, 2018, pp. 786-796.
- [11] J. J. Kasianowicz, E. Brandin, D. Branton, and D. W. Deamer, "Characterization of individual polynucleotide molecules using a membrane channel," *Proceedings of the National Academy of Sciences of the United States of America*, vol. 93, no. 24, 1996, pp. 13770-13773.
- [12] M. Faller, M. Niederweis, and G. E. Schulz, "The structure of a mycobacterial outer-membrane channel," *Science*, vol. 303, no. 5661, 2004, pp. 1189-1192.
- [13] E. A. Manrao, I. M. Derrington, M. Pavlenok, M. Niederweis, and J. H. Gundlach, "Nucleotide Discrimination with DNA Immobilized in the MspA Nanopore," *Plos One*, vol. 6, no. 10, 2011.
- [14] J. M. Carter and S. Hussain, "Robust long-read native DNA sequencing using the ONT CsgG Nanopore system," *Wellcome Open Res*, vol. 2, 2017, p. 23.
- [15] S. Zeng, C. Wen, P. Solomon, S.-L. Zhang, and Z. Zhang, "Rectification of protein translocation in truncated pyramidal nanopores," *Nature Nanotechnology*, vol. 14, no. 11, 2019, pp. 1056-1062.

- [16] B. M. Venkatesan, A. B. Shah, J. M. Zuo, and R. Bashir, "DNA Sensing using Nano-crystalline Surface Enhanced Al(2)O(3) Nanopore Sensors," *Advanced Functional Materials*, vol. 20, no. 8, 2010, pp. 1266-1275.
- [17] R. Wang, T. Gilboa, J. Song, D. Huttner, M. W. Grinstaff, and A. Meller, "Single-Molecule Discrimination of Labeled DNAs and Polypeptides Using Photoluminescent-Free TiO₂ Nanopores," *ACS Nano*, vol. 12, no. 11, 2018, pp. 11648-11656.
- [18] J. Larkin, R. Henley, D. C. Bell, T. Cohen-Karni, J. K. Rosenstein, and M. Wanunu, "Slow DNA Transport through Nanopores in Hafnium Oxide Membranes," *ACS Nano*, vol. 7, no. 11, 2013, pp. 10121-10128.
- [19] S. J. Heerema and C. Dekker, "Graphene nanodevices for DNA sequencing," *Nature Nanotechnology*, vol. 11, no. 2, 2016, pp. 127-136.
- [20] J. Feng *et al.*, "Single-layer MoS₂ nanopores as nanopower generators," *Nature*, vol. 536, no. 7615, 2016, pp. 197-200.
- [21] M. Mojtavavi, A. VahidMohammadi, W. Liang, M. Beidaghi, and M. Wanunu, "Single-Molecule Sensing Using Nanopores in Two-Dimensional Transition Metal Carbide (MXene) Membranes," *ACS Nano*, vol. 13, no. 3, 2019, pp. 3042-3053.
- [22] J. Li, D. Stein, C. McMullan, D. Branton, M. J. Aziz, and J. A. Golovchenko, "Ion-beam sculpting at nanometre length scales," *Nature*, vol. 412, no. 6843, 2001, pp. 166-169.
- [23] A. J. Storm, J. H. Chen, X. S. Ling, H. W. Zandbergen, and C. Dekker, "Fabrication of solid-state nanopores with single-nanometre precision," *Nature Materials*, vol. 2, no. 8, 2003, pp. 537-540.
- [24] J. Gierak *et al.*, "Sub-5nm FIB direct patterning of nanodevices," *Microelectronic Engineering*, vol. 84, no. 5, 2007, pp. 779-783.
- [25] E. Kennedy, Z. Dong, C. Tennant, and G. Timp, "Reading the primary structure of a protein with 0.07 nm³ resolution using a subnanometre-diameter pore," *Nature Nanotechnology*, vol. 11, no. 11, 2016, pp. 968-976.
- [26] H. Kwok, K. Briggs, and V. Tabard-Cossa, "Nanopore Fabrication by Controlled Dielectric Breakdown," *PLOS ONE*, vol. 9, no. 3, 2014, p. e92880.
- [27] I. Yanagi, R. Akahori, T. Hatano, and K.-i. Takeda, "Fabricating nanopores with diameters of sub-1 nm to 3 nm using multilevel pulse-voltage injection," *Scientific Reports*, vol. 4, no. 1, 2014, p. 5000.
- [28] C. E. Arcadia, C. C. Reyes, and J. K. Rosenstein, "In Situ Nanopore Fabrication and Single-Molecule Sensing with Microscale Liquid Contacts," *ACS Nano*, vol. 11, no. 5, 2017, pp. 4907-4915.
- [29] M. Waugh *et al.*, "Solid-state nanopore fabrication by automated controlled breakdown," *Nature Protocols*, vol. 15, no. 1, 2020, pp. 122-143.
- [30] S. R. Park, H. Peng, and X. S. Ling, "Fabrication of Nanopores in Silicon Chips Using Feedback Chemical Etching," *Small*, vol. 3, no. 1, 2007, pp. 116-119.
- [31] T. Schmidt, M. Zhang, I. Sychugov, N. Roxhed, and J. Linnros, "Nanopore arrays in a silicon membrane for parallel single-molecule detection: fabrication," *Nanotechnology*, vol. 26, no. 31, 2015, p. 314001.
- [32] Q. Chen, Y. Wang, T. Deng, and Z. Liu, "Fabrication of nanopores and nanoslits with feature sizes down to 5 nm by wet etching method," *Nanotechnology*, vol. 29, no. 8, 2018, p. 085301.
- [33] M. Zhang, T. Schmidt, F. Sangghaleh, N. Roxhed, I. Sychugov, and J. Linnros, "Oxidation of nanopores in a silicon membrane: self-limiting formation of sub-10 nm circular openings," *Nanotechnology*, vol. 25, no. 35, 2014, p. 355302.

- [34] M. Ayub *et al.*, "Precise electrochemical fabrication of sub-20 nm solid-state nanopores for single-molecule biosensing," *Journal of Physics: Condensed Matter*, vol. 22, no. 45, 2010, p. 454128.
- [35] A. Rutkowska, K. Freedman, J. Skalkowska, M. J. Kim, J. B. Edel, and T. Albrecht, "Electrodeposition and Bipolar Effects in Metallized Nanopores and Their Use in the Detection of Insulin," *Analytical Chemistry*, vol. 87, no. 4, 2015, pp. 2337-2344.
- [36] O. M. Eggenberger, C. Ying, and M. Mayer, "Surface coatings for solid-state nanopores," *Nanoscale*, vol. 11, no. 42, 2019, pp. 19636-19657.
- [37] X. Li *et al.*, "Non-sticky translocation of bio-molecules through Tween 20-coated solid-state nanopores in a wide pH range," vol. 109, no. 14, 2016, p. 143105.
- [38] Y. Xie *et al.*, "Surface Modification of Single Track-Etched Nanopores with Surfactant CTAB," *Langmuir*, vol. 25, no. 16, 2009, pp. 8870-8874.
- [39] M. Ali *et al.*, "Layer-by-Layer Assembly of Polyelectrolytes into Ionic Current Rectifying Solid-State Nanopores: Insights from Theory and Experiment," *Journal of the American Chemical Society*, vol. 132, no. 24, 2010, pp. 8338-8348.
- [40] T. Ma *et al.*, "Impact of Polyelectrolyte Multilayers on the Ionic Current Rectification of Conical Nanopores," *Langmuir*, vol. 34, no. 11, 2018, pp. 3405-3412.
- [41] N. Giamblanco, D. Coglitore, J.-M. Janot, P. E. Coulon, B. Charlot, and S. Balme, "Detection of protein aggregate morphology through single antifouling nanopore," *Sensors and Actuators B: Chemical*, vol. 260, 2018, pp. 736-745.
- [42] Z. Siwy, L. Trofin, P. Kohli, L. A. Baker, C. Trautmann, and C. R. Martin, "Protein Biosensors Based on Biofunctionalized Conical Gold Nanotubes," *Journal of the American Chemical Society*, vol. 127, no. 14, 2005, pp. 5000-5001.
- [43] G. Emilsson *et al.*, "Polymer brushes in solid-state nanopores form an impenetrable entropic barrier for proteins," *Nanoscale*, vol. 10, no. 10, 2018, pp. 4663-4669.
- [44] R. Wei, V. Gatterdam, R. Wieneke, R. Tampé, and U. Rant, "Stochastic sensing of proteins with receptor-modified solid-state nanopores," *Nature Nanotechnology*, vol. 7, no. 4, 2012, pp. 257-263.
- [45] E. C. Yusko *et al.*, "Real-time shape approximation and fingerprinting of single proteins using a nanopore," *Nature Nanotechnology*, vol. 12, no. 4, 2017, pp. 360-367.
- [46] E. C. Yusko *et al.*, "Controlling protein translocation through nanopores with bio-inspired fluid walls," *Nature Nanotechnology*, vol. 6, no. 4, 2011, pp. 253-260.
- [47] C.-M. Wang, D.-L. Kong, Q. Chen, and J.-M. Xue, "Surface engineering of synthetic nanopores by atomic layer deposition and their applications," *Frontiers of Materials Science*, vol. 7, no. 4, 2013, pp. 335-349.
- [48] P. Chen, T. Mitsui, D. B. Farmer, J. Golovchenko, R. G. Gordon, and D. Branton, "Atomic Layer Deposition to Fine-Tune the Surface Properties and Diameters of Fabricated Nanopores," *Nano Letters*, vol. 4, no. 7, 2004, pp. 1333-1337.
- [49] S. M. George, "Atomic Layer Deposition: An Overview," *Chemical Reviews*, vol. 110, no. 1, 2010, pp. 111-131.
- [50] J. Houghtaling *et al.*, "Estimation of Shape, Volume, and Dipole Moment of Individual Proteins Freely Transiting a Synthetic Nanopore," *ACS Nano*, vol. 13, no. 5, 2019, pp. 5231-5242.

- [51] A. R. Hall, A. Scott, D. Rotem, K. K. Mehta, H. Bayley, and C. Dekker, "Hybrid pore formation by directed insertion of α -haemolysin into solid-state nanopores," *Nature Nanotechnology*, vol. 5, no. 12, 2010, pp. 874-877.
- [52] C. R. Engst, M. Ablay, G. Divitini, C. Ducati, T. Liedl, and U. F. Keyser, "DNA Origami Nanopores," *Nano Letters*, vol. 12, no. 1, 2012, pp. 512-517.
- [53] B. Cressiot, S. J. Greive, M. Mojtavavi, A. A. Antson, and M. Wanunu, "Thermostable virus portal proteins as reprogrammable adapters for solid-state nanopore sensors," *Nature Communications*, vol. 9, no. 1, 2018, p. 4652.
- [54] A. Zhang and C. M. Lieber, "Nano-Bioelectronics," *Chemical Reviews*, vol. 116, no. 1, 2016, pp. 215-257.
- [55] P. Xie, Q. Xiong, Y. Fang, Q. Qing, and C. M. Lieber, "Local electrical potential detection of DNA by nanowire-nanopore sensors," *Nature Nanotechnology*, vol. 7, no. 2, 2012, pp. 119-125.
- [56] M. Puster *et al.*, "Cross-Talk Between Ionic and Nanoribbon Current Signals in Graphene Nanoribbon-Nanopore Sensors for Single-Molecule Detection," vol. 11, no. 47, 2015, pp. 6309-6316.
- [57] S. J. Heerema, L. Vicarelli, S. Pud, R. N. Schouten, H. W. Zandbergen, and C. Dekker, "Probing DNA Translocations with Inplane Current Signals in a Graphene Nanoribbon with a Nanopore," *ACS Nano*, vol. 12, no. 3, 2018, pp. 2623-2633.
- [58] F. Traversi *et al.*, "Detecting the translocation of DNA through a nanopore using graphene nanoribbons," *Nature Nanotechnology*, vol. 8, no. 12, 2013, pp. 939-945.
- [59] L. Xue *et al.*, "Gated Single-Molecule Transport in Double-Barreled Nanopores," *ACS Applied Materials & Interfaces*, vol. 10, no. 44, 2018, pp. 38621-38629.
- [60] G. Binnig and H. Rohrer, "Scanning tunneling microscopy," *Surface Science*, vol. 126, no. 1, 1983, pp. 236-244.
- [61] M. Zwolak and M. Di Ventra, "Electronic Signature of DNA Nucleotides via Transverse Transport," *Nano Letters*, vol. 5, no. 3, 2005, pp. 421-424.
- [62] S. J. Heerema and C. Dekker, "Graphene nanodevices for DNA sequencing," *Nature Nanotechnology*, vol. 11, no. 2, 2016, pp. 127-136.
- [63] A. B. Farimani, K. Min, and N. R. Aluru, "DNA Base Detection Using a Single-Layer MoS₂," *ACS Nano*, vol. 8, no. 8, 2014, pp. 7914-7922.
- [64] S. Liang *et al.*, "Noise in nanopore sensors: Sources, models, reduction, and benchmarking," *Nanotechnology and Precision Engineering*, vol. 3, no. 1, 2020, pp. 9-17.
- [65] A. Fragasso, S. Schmid, and C. Dekker, "Comparing Current Noise in Biological and Solid-State Nanopores," *ACS Nano*, vol. 14, no. 2, 2020, pp. 1338-1349.
- [66] C. Wen *et al.*, "Generalized Noise Study of Solid-State Nanopores at Low Frequencies," *ACS Sensors*, vol. 2, no. 2, 2017, pp. 300-307.
- [67] C. Wen, S. Zeng, Z. Zhang, and S.-L. Zhang, "Group Behavior of Nanoparticles Translocating Multiple Nanopores," *Analytical Chemistry*, vol. 90, no. 22, 2018, pp. 13483-13490.
- [68] T. Gilboa and A. Meller, "Optical sensing and analyte manipulation in solid-state nanopores," *Analyst*, vol. 140, no. 14, 2015, pp. 4733-4747.
- [69] B. McNally, A. Singer, Z. Yu, Y. Sun, Z. Weng, and A. Meller, "Optical recognition of converted DNA nucleotides for single-molecule DNA sequencing using nanopore arrays," *Nano Letters*, vol. 10, no. 6, 2010, pp. 2237-2244.

- [70] D. Nykypanchuk, H. H. Strey, and D. A. Hoagland, "Brownian motion of DNA confined within a two-dimensional array," *Science*, vol. 297, no. 5583, 2002, pp. 987-990.
- [71] G. Ando, C. Hyun, J. Li, and T. Mitsui, "Directly Observing the Motion of DNA Molecules near Solid-State Nanopores," *ACS Nano*, vol. 6, no. 11, 2012, pp. 10090-10097.
- [72] T. Auger *et al.*, "Zero-mode waveguide detection of flow-driven DNA translocation through nanopores," *Physical Review Letters*, vol. 113, no. 2, 2014, p. 028302.
- [73] H. Yamazaki, K. Esashika, and T. Saiki, "A 150 nm ultraviolet excitation volume on a porous silicon membrane for direct optical observation of DNA coil relaxation during capture into nanopores," *Nano Futures*, vol. 1, no. 1, 2017, p. 011001.
- [74] A. B. Dahlin, "Sensing applications based on plasmonic nanopores: The hole story," *Analyst*, vol. 140, no. 14, 2015, pp. 4748-4759.
- [75] J. D. Spitzberg, A. Zrehen, X. F. van Kooten, and A. Meller, "Plasmonic-Nanopore Biosensors for Superior Single-Molecule Detection," *Advanced Materials*, vol. 31, no. 23, 2019, p. 1900422.
- [76] D. Garoli, H. Yamazaki, N. Maccaferri, and M. Wanunu, "Plasmonic Nanopores for Single-Molecule Detection and Manipulation: Toward Sequencing Applications," *Nano Letters*, vol. 19, no. 11, 2019, pp. 7553-7562.
- [77] O. N. Assad, T. Gilboa, J. Spitzberg, M. Juhasz, E. Weinhold, and A. Meller, "Light-Enhancing Plasmonic-Nanopore Biosensor for Superior Single-Molecule Detection," *Advanced Materials*, vol. 29, no. 9, 2017, p. 1605442.
- [78] Y. Yao, C. Wen, N. H. Pham, and S.-L. Zhang, "On Induced Surface Charge in Solid-State Nanopores," *Langmuir*, vol. 36, no. 30, 2020, pp. 8874-8882.
- [79] D. P. Hoogerheide, S. Garaj, and J. A. Golovchenko, "Probing Surface Charge Fluctuations with Solid-State Nanopores," *Physical Review Letters*, vol. 102, no. 25, 2009, p. 256804.
- [80] J.-P. Cloarec *et al.*, "pH driven addressing of silicon nanowires onto Si₃N₄/SiO₂ micro-patterned surfaces," *Nanotechnology*, vol. 27, no. 29, 2016, p. 295602.
- [81] A. W. Adamson and A. P. Gast, *Physical Chemistry of Surfaces*. New York: Wiley, 1997.
- [82] S. W. Kowalczyk, A. Y. Grosberg, Y. Rabin, and C. Dekker, "Modeling the conductance and DNA blockade of solid-state nanopores," *Nanotechnology*, vol. 22, no. 31, 2011, p. 315101.
- [83] C. Wen, Z. Zhang, and S.-L. Zhang, "Physical Model for Rapid and Accurate Determination of Nanopore Size via Conductance Measurement," *ACS Sensors*, vol. 2, no. 10, 2017, pp. 1523-1530.
- [84] C. Wen, "Solid-State Nanopores for Sensing : From Theory to Applications," Doctoral thesis, comprehensive summary, Digital Comprehensive Summaries of Uppsala Dissertations from the Faculty of Science and Technology, Acta Universitatis Upsaliensis, Uppsala, 1825, 2019.
- [85] B. Luan and A. Aksimentiev, "Electro-osmotic screening of the DNA charge in a nanopore," *Physical Review. E, Statistical, Nonlinear, and Soft Matter Physics*, vol. 78, no. 2 Pt 1, 2008, pp. 021912-021912.
- [86] M. Wanunu, W. Morrison, Y. Rabin, A. Y. Grosberg, and A. Meller, "Electrostatic focusing of unlabelled DNA into nanoscale pores using a salt gradient," *Nature Nanotechnology*, vol. 5, no. 2, 2010, pp. 160-165.
- [87] N. C. Stellwagen, C. Gelfi, and P. G. Righetti, "The free solution mobility of DNA," *Biopolymers*, vol. 42, no. 6, 1997, pp. 687-703.

- [88] A. E. Nkodo *et al.*, "Diffusion coefficient of DNA molecules during free solution electrophoresis," *ELECTROPHORESIS*, vol. 22, no. 12, 2001, pp. 2424-2432.
- [89] E. Stellwagen and N. C. Stellwagen, "Determining the electrophoretic mobility and translational diffusion coefficients of DNA molecules in free solution," *ELECTROPHORESIS*, vol. 23, no. 16, 2002, pp. 2794-2803.
- [90] M. Gershow and J. A. Golovchenko, "Recapturing and trapping single molecules with a solid-state nanopore," *Nature Nanotechnology*, vol. 2, no. 12, 2007, pp. 775-779.
- [91] N. A. W. Bell, M. Muthukumar, and U. F. Keyser, "Translocation frequency of double-stranded DNA through a solid-state nanopore," *Physical Review. E*, vol. 93, no. 2, 2016, pp. 022401-022401.
- [92] Y.-C. Chou, P. Masih Das, D. S. Monos, and M. Drndić, "Lifetime and Stability of Silicon Nitride Nanopores and Nanopore Arrays for Ionic Measurements," *ACS Nano*, vol. 14, no. 6, 2020, pp. 6715-6728.
- [93] E. Laarz, B. V. Zhmud, and L. Bergström, "Dissolution and Deagglomeration of Silicon Nitride in Aqueous Medium," *Journal of the American Ceramic Society*, vol. 83, no. 10, 2000, pp. 2394-2400.
- [94] F. T. Mackenzie, R. M. Garrels, O. P. Bricker, and F. Bickley, "Silica in Sea Water: Control by Silica Minerals," *Science*, vol. 155, no. 3768, 1967, p. 1404.
- [95] J. G. Croissant, Y. Faticiev, and N. M. Khashab, "Degradability and Clearance of Silicon, Organosilica, Silsesquioxane, Silica Mixed Oxide, and Mesoporous Silica Nanoparticles," *Advanced Materials*, vol. 29, no. 9, 2017, p. 1604634.
- [96] R. Rollings, E. Graef, N. Walsh, S. Nandivada, M. Benamara, and J. Li, "The effects of geometry and stability of solid-state nanopores on detecting single DNA molecules," *Nanotechnology*, vol. 26, no. 4, 2015, p. 044001.
- [97] M. van den Hout, A. R. Hall, M. Y. Wu, H. W. Zandbergen, C. Dekker, and N. H. Dekker, "Controlling nanopore size, shape and stability," *Nanotechnology*, vol. 21, no. 11, 2010, p. 115304.
- [98] M. Vogt and R. Hauptmann, "Plasma-deposited passivation layers for moisture and water protection," *Surface and Coatings Technology*, vol. 74-75, 1995, pp. 676-681.
- [99] H. Yamazaki, R. Hu, Q. Zhao, and M. Wanunu, "Photothermally Assisted Thinning of Silicon Nitride Membranes for Ultrathin Asymmetric Nanopores," *ACS Nano*, vol. 12, no. 12, 2018, pp. 12472-12481.
- [100] T. Gilboa, E. Zvuloni, A. Zrehen, A. H. Squires, and A. Meller, "Automated, Ultra-Fast Laser-Drilling of Nanometer Scale Pores and Nanopore Arrays in Aqueous Solutions," *Advanced Functional Materials*, vol. 30, no. 18, 2020, p. 1900642.
- [101] T. Gilboa, A. Zrehen, A. Girsault, and A. Meller, "Optically-Monitored Nanopore Fabrication Using a Focused Laser Beam," *Scientific Reports*, vol. 8, no. 1, 2018, p. 9765.
- [102] H. Yamazaki *et al.*, "Label-Free Single-Molecule Thermoscopy Using a Laser-Heated Nanopore," *Nano Letters*, vol. 17, no. 11, 2017, pp. 7067-7074.
- [103] P. Mehrotra, "Biosensors and their applications - A review," *Journal of Oral Biology and Craniofacial Research*, vol. 6, no. 2, 2016, pp. 153-159.
- [104] J. R. Mejía-Salazar and O. N. Oliveira, "Plasmonic Biosensing," *Chemical Reviews*, vol. 118, no. 20, 2018, pp. 10617-10625.
- [105] M. Ozboyaci, D. B. Kokh, S. Corni, and R. C. Wade, "Modeling and simulation of protein-surface interactions: achievements and challenges," *Quarterly Reviews of Biophysics*, vol. 49, 2016, p. e4.

- [106] W. Norde and J. Lyklema, "Why proteins prefer interfaces," *Journal of Bio-material Science Polymer Edition*, vol. 2, no. 3, 1991, pp. 183-202.
- [107] D. S. Salloum and J. B. Schlenoff, "Protein adsorption modalities on polyelectrolyte multilayers," *Biomacromolecules*, vol. 5, no. 3, 2004, pp. 1089-1096.
- [108] R. A. Hartvig, M. van de Weert, J. Østergaard, L. Jorgensen, and H. Jensen, "Protein Adsorption at Charged Surfaces: The Role of Electrostatic Interactions and Interfacial Charge Regulation," *Langmuir*, vol. 27, no. 6, 2011, pp. 2634-2643.
- [109] S. N. Jamadagni, R. Godawat, and S. Garde, "Hydrophobicity of Proteins and Interfaces: Insights from Density Fluctuations," *Annual Review of Chemical and Biomolecular Engineering*, vol. 2, no. 1, 2011, pp. 147-171.
- [110] J. N. Israelachvili and R. M. Pashley, "Molecular layering of water at surfaces and origin of repulsive hydration forces," *Nature*, vol. 306, no. 5940, 1983, pp. 249-250.
- [111] I. Szleifer, "Polymers and proteins: interactions at interfaces," *Current Opinion in Solid State and Materials Science*, vol. 2, no. 3, 1997, pp. 337-344.
- [112] Z. Nie and E. Kumacheva, "Patterning surfaces with functional polymers," *Nature Materials*, vol. 7, no. 4, 2008, pp. 277-290.
- [113] W. F. van Dorp and C. W. Hagen, "A critical literature review of focused electron beam induced deposition," *Journal of Applied Physics*, vol. 104, no. 8, 2008, p. 081301.
- [114] J. Korlach *et al.*, "Selective aluminum passivation for targeted immobilization of single DNA polymerase molecules in zero-mode waveguide nanostructures," *Proceedings of the National Academy of Sciences of the United States of America*, vol. 105, no. 4, 2008, pp. 1176-1181.
- [115] R. Schlapak, J. Danzberger, T. Haselgrübler, P. Hinterdorfer, F. Schäffler, and S. Howorka, "Painting with Biomolecules at the Nanoscale: Biofunctionalization with Tunable Surface Densities," *Nano Letters*, vol. 12, no. 4, 2012, pp. 1983-1989.
- [116] E. Hoque, J. A. DeRose, G. Kulik, P. Hoffmann, H. J. Mathieu, and B. Bhushan, "Alkylphosphonate Modified Aluminum Oxide Surfaces," *The Journal of Physical Chemistry B*, vol. 110, no. 22, 2006, pp. 10855-10861.
- [117] "Handbook of X-ray and ultraviolet photoelectron spectroscopy. Herausgegeben von D. Briggs; Heyden & Son LTD, 1977, 400 Seiten, DM 192,—," *Physik in unserer Zeit*, vol. 10, no. 1, 1979, pp. 30-30.
- [118] O. Söderberg *et al.*, "Direct observation of individual endogenous protein complexes in situ by proximity ligation," *Nature Methods*, vol. 3, no. 12, 2006, pp. 995-1000.
- [119] H. Wang, R. Yang, L. Yang, and W. Tan, "Nucleic Acid Conjugated Nanomaterials for Enhanced Molecular Recognition," *ACS Nano*, vol. 3, no. 9, 2009, pp. 2451-2460.
- [120] K. Saha, S. S. Agasti, C. Kim, X. Li, and V. M. Rotello, "Gold Nanoparticles in Chemical and Biological Sensing," *Chemical Reviews*, vol. 112, no. 5, 2012, pp. 2739-2779.
- [121] D. A. Giljohann, D. S. Seferos, W. L. Daniel, M. D. Massich, P. C. Patel, and C. A. Mirkin, "Gold nanoparticles for biology and medicine," *Angewandte Chemie International Edition*, vol. 49, no. 19, 2010, pp. 3280-3294.
- [122] S. Nam *et al.*, "Graphene nanopore with a self-integrated optical antenna," *Nano Letters*, vol. 14, no. 10, 2014, pp. 5584-5589.
- [123] R. D. Bulushev, L. J. Steinbock, S. Khlybov, J. F. Steinbock, U. F. Keyser, and A. Radenovic, "Measurement of the Position-Dependent Electrophoretic Force

- on DNA in a Glass Nanocapillary," *Nano Letters*, vol. 14, no. 11, 2014, pp. 6606-6613.
- [124] K. Chuah *et al.*, "Nanopore blockade sensors for ultrasensitive detection of proteins in complex biological samples," *Nature Communications*, vol. 10, no. 1, 2019, p. 2109.
 - [125] C. A. Keller, K. Glasmästar, V. P. Zhdanov, and B. Kasemo, "Formation of Supported Membranes from Vesicles," *Physical Review Letters*, vol. 84, no. 23, 2000, pp. 5443-5446.
 - [126] V. P. Zhdanov and B. Kasemo, "Comments on Rupture of Adsorbed Vesicles," *Langmuir*, vol. 17, no. 12, 2001, pp. 3518-3521.
 - [127] F. Y. Jiang, Y. Bouret, and J. T. Kindt, "Molecular Dynamics Simulations of the Lipid Bilayer Edge," *Biophysical Journal*, vol. 87, no. 1, 2004, pp. 182-192.
 - [128] P. M. Kasson and V. S. Pande, "Molecular Dynamics Simulation of Lipid Re-orientation at Bilayer Edges," *Biophysical Journal*, vol. 86, no. 6, 2004, pp. 3744-3749.
 - [129] R. Richter, A. Mukhopadhyay, and A. Brisson, "Pathways of Lipid Vesicle Deposition on Solid Surfaces: A Combined QCM-D and AFM Study," *Biophysical Journal*, vol. 85, no. 5, 2003, pp. 3035-3047.
 - [130] D. Axelrod, D. E. Koppel, J. Schlessinger, E. Elson, and W. W. Webb, "Mobility measurement by analysis of fluorescence photobleaching recovery kinetics," *Biophysical Journal*, vol. 16, no. 9, 1976, pp. 1055-1069.
 - [131] D. M. Soumpasis, "Theoretical analysis of fluorescence photobleaching recovery experiments," *Biophysical Journal*, vol. 41, no. 1, 1983, pp. 95-97.
 - [132] O. M. Eggenberger *et al.*, "Fluid surface coatings for solid-state nanopores: comparison of phospholipid bilayers and archaea-inspired lipid monolayers," *Nanotechnology*, vol. 30, no. 32, 2019, p. 325504.
 - [133] O. N. Assad, N. Di Fiori, A. H. Squires, and A. Meller, "Two Color DNA Barcode Detection in Photoluminescence Suppressed Silicon Nitride Nanopores," *Nano Letters*, vol. 15, no. 1, 2015, pp. 745-752.
 - [134] Z. Roelen, J. A. Bustamante, A. Carlsen, A. Baker-Murray, and V. Tabard-Cossa, "Instrumentation for low noise nanopore-based ionic current recording under laser illumination," *Review of Scientific Instruments*, vol. 89, no. 1, 2018, p. 015007.
 - [135] V. Kurz, E. M. Nelson, J. Shim, and G. Timp, "Direct Visualization of Single-Molecule Translocations through Synthetic Nanopores Comparable in Size to a Molecule," *ACS Nano*, vol. 7, no. 5, 2013, pp. 4057-4069.
 - [136] C. Plesa *et al.*, "Direct observation of DNA knots using a solid-state nanopore," *Nature Nanotechnology*, vol. 11, no. 12, 2016, pp. 1093-1097.
 - [137] R. Kumar Sharma, I. Agrawal, L. Dai, P. S. Doyle, and S. Garaj, "Complex DNA knots detected with a nanopore sensor," *Nature Communications*, vol. 10, no. 1, 2019, p. 4473.
 - [138] L. J. Steinbock, O. Otto, C. Chimere, J. Gornall, and U. F. Keyser, "Detecting DNA Folding with Nanocapillaries," *Nano Letters*, vol. 10, no. 7, 2010, pp. 2493-2497.
 - [139] M. Kosmulski, "Isoelectric points and points of zero charge of metal (hydr)oxides: 50years after Parks' review," *Advances in Colloid and Interface Science*, vol. 238, 2016, pp. 1-61.
 - [140] R. M. M. Smeets, U. F. Keyser, D. Krapf, M.-Y. Wu, N. H. Dekker, and C. Dekker, "Salt Dependence of Ion Transport and DNA Translocation through Solid-State Nanopores," *Nano Letters*, vol. 6, no. 1, 2006, pp. 89-95.

- [141] N. Di Fiori, A. Squires, D. Bar, T. Gilboa, T. D. Moustakas, and A. Meller, "Optoelectronic control of surface charge and translocation dynamics in solid-state nanopores," *Nature Nanotechnology*, vol. 8, no. 12, 2013, pp. 946-951.
- [142] M. Muthukumar, "Polymer escape through a nanopore," vol. 118, no. 11, 2003, pp. 5174-5184.
- [143] M. Muthukumar, "Polymer translocation through a hole," *The Journal of Chemical Physics*, vol. 111, no. 22, 1999, pp. 10371-10374.
- [144] D. Fologea, B. Ledden, D. S. McNabb, and J. Li, "Electrical characterization of protein molecules by a solid-state nanopore," *Applied Physics Letters*, vol. 91, no. 5, 2007, pp. 539011-539013.
- [145] A. Oukhaled *et al.*, "Dynamics of completely unfolded and native proteins through solid-state nanopores as a function of electric driving force," *ACS Nano*, vol. 5, no. 5, 2011, pp. 3628-3638.
- [146] S. W. Kowalczyk *et al.*, "Single-molecule transport across an individual biomimetic nuclear pore complex," *Nature Nanotechnology*, vol. 6, no. 7, 2011, pp. 433-438.
- [147] C. Plesa, S. W. Kowalczyk, R. Zinsmeister, A. Y. Grosberg, Y. Rabin, and C. Dekker, "Fast Translocation of Proteins through Solid State Nanopores," *Nano Letters*, vol. 13, no. 2, 2013, pp. 658-663.
- [148] X. Shi *et al.*, "Dynamics of a Molecular Plug Docked onto a Solid-State Nanopore," *The Journal of Physical Chemistry Letters*, vol. 9, no. 16, 2018, pp. 4686-4694.
- [149] A. Ivankin, R. Y. Henley, J. Larkin, S. Carson, M. L. Toscano, and M. Wanunu, "Label-Free Optical Detection of Biomolecular Translocation through Nanopore Arrays," *ACS Nano*, vol. 8, no. 10, 2014, pp. 10774-10781.

Acta Universitatis Upsaliensis

*Digital Comprehensive Summaries of Uppsala Dissertations
from the Faculty of Science and Technology 2010*

Editor: The Dean of the Faculty of Science and Technology

A doctoral dissertation from the Faculty of Science and Technology, Uppsala University, is usually a summary of a number of papers. A few copies of the complete dissertation are kept at major Swedish research libraries, while the summary alone is distributed internationally through the series Digital Comprehensive Summaries of Uppsala Dissertations from the Faculty of Science and Technology. (Prior to January, 2005, the series was published under the title "Comprehensive Summaries of Uppsala Dissertations from the Faculty of Science and Technology".)

Distribution: publications.uu.se
urn:nbn:se:uu:diva-433812



ACTA
UNIVERSITATIS
UPSALIENSIS
UPPSALA
2021